國 立 交 通 大 學

機 械 工 程 學 系

博 士 論 文

脈衝式電源之平板型介電質常壓電漿束特性分析及
利用其後放電區域的應用研究

Characterization of a Planar Atmospheric Dielectric Barrier Discharge

Driven by a Pulsed-Power Source and Its Applications Using

Post-Discharge Jet Region

研 究 生： 江明鴻

指導教授： 吳宗信 博士

中 華 民 國 九 十 九 年 六 月

脈衝式電源之平板型介電質常壓電漿束特性分析及利用其後放電

區域的應用研究

Characterization of a Planar Atmospheric Dielectric Barrier Discharge

Driven by a Pulsed-Power Source and Its Applications Using

Post-Discharge Jet Region

研 究 生： 江明鴻　　　　　　　　Student:　Ming-Hung Chiang

指導教授： 吳宗信 博士　　　　　　Advisor:　Dr. Jong-Shinn Wu

A Thesis

Submitted to Department of Mechanical Engineering College of Engineering
National Chiao Tung Iniversity
In partial Fulfillment of the Requirements
for the Degree of Doctor of Philosophy in Mechanical Engineering
June 2010

Hsinchu, Taiwan

中 華 民 國 九 十 九 年 六 月

脈衝式電源之平板型介電質常壓電漿束特性分析及利用其後放電區域的應用研究

學生：江明鴻　　　　　　　　　　　　指導教授：吳宗信 博士

國立交通大學機械工程學系博士班

中文摘要

本論文探討自組的脈衝式電源驅動的平板型介電質常壓電漿束 (氮氣為主)，及電漿束的後放電區域特性分析及其應用之研究。特性分析主要包括拍照直接觀察、電性量測 (電壓及電流波型，電漿吸收功率)、光譜量測 (OES 及 FTIR)、氣體溫度量測 (熱電偶線及 OES)與臭氧濃度量測。量測顯示純氮 DBD 電漿產生大量亞穩態氮氣 [$N_2(A^3\sum_u^+)$]，逐漸加入氧氣後產生大量臭氧。同時，根據後放電區域量得的光譜特性，吾人成功地瞭解相關電漿化學反應機制。了解這些反應機制對表面處理相關的應用是相當重要的。此研究使用氮氣為主的平板型介電質常壓電漿束的應用研究包括 PP 薄片親水性改質、ITO 玻璃表面清潔、*E. coli*/ *B. subtilis* 殺菌與 *B. subtilis* 孢子滅菌。結果顯示這些特性對於應用有很大效率影響，簡單的敘述如下。

在靜止 PP 薄片表面親水特性處理方面，以氮氣為主 (氧氣/氮氣比小於 1%) 平板型 DBD 常壓電漿束處理後 (處理距離小於 10 mm，處理時間 5 秒)，接觸角從原先 103 度降至 30 度。處理後 PP 薄片靜置 24 小時後接觸角恢復至 40 度。同樣電漿條件對靜止的 ITO 玻璃表面處理，結果顯示 (氧氣/氮氣比) 有兩個區域接觸角從 84 度降至 20-30 度。第一區域為氧氣/氮氣比小於 0.05%，處理距離 6-16 mm。第二區域為氧氣/氮氣比超過

0.06%，處理距離 2-10 mm。量測結果顯示: (1) 於後放電出口 10 mm 內，亞穩態氮氣 [$N_2(A^3\sum_u^+)$]與臭氧光分解反應均扮演主要角色對於表面處理，而相關電漿反應過程需再進一步研究釐清。(2) 遠離大於後放電出口 10 mm，對於 ITO 玻璃清潔及 PP 薄板表面親水改質，亞穩態氮氣[$N_2(A^3\sum_u^+)$]扮演了主要角色。XPS 量測結果發現，經過平板型 DBD 常壓電漿束處理後的試片隨 O/C 比增加而更加具有親水性。

在 *E. coli* 與 *B. subtilis* 殺菌的應用，結果顯示與前人在放電區域的研究相較後放電區滅菌效率仍然相當優異，毫無遜色。主要關鍵在於電漿放氣體中需要加入氧氣以產生足夠量的臭氧增加滅菌效率。此外使用空氣平板型介電質常壓電漿束的滅菌效率比氧氣電漿好，可能與空氣電漿中含有氮氧化物與臭氧同時對滅菌作出貢獻。在 *E. coli* 與 *B. subtilis* (10^7 CFU/mL)存活率實驗方面，經過氧氣及空氣電漿處理小於 18 次 (等效停留時間 1.8 秒)，距離介於 4-20 mm，均可以使菌種達到完全失活(inactivation)。在 *B. subtilis* 孢子($10^5 – 10^7$ spore/mL)滅菌實驗方面，經過加入 2%四氟化碳的空氣電漿對孢子滅菌處理效果相當優異(單純空氣電漿處理幾乎完全無效)。經過 2%四氟化碳的空氣電漿處理小於 10 次 (等效停留時間 1 秒)，距離 14 mm，均可以達到完全滅菌。間接證明應有不少高化學反應性自由基 (如氟原子)，存在放電及後放電區域。

總結來說，本博士論文在實驗上針對氮氣為主的平板型介電質常壓電漿束自組架設完成及有效的特性分析，成功地利用其後放電區域進行應用的研究。與前人大部分直接利用放電區域進行分析與應用的研究相較，本論文相對是較獨特的。同時在論文最後章節亦條列出建議未來應進行研究的研究部分。

Characterization of a Planar Atmospheric Dielectric Barrier Discharge

Driven by a Pulsed-Power Source and Its Applications

Using Post-Discharge Jet Region

Student: Ming-Hung Chiang   Advisor: Dr. Jong-Shinn Wu

Department of Mechanical Engineering

National Chiao Tung University

Abstract

Development, characterization of a planar atmospheric-pressure nitrogen-based dielectric barrier discharge driven by a quasi-pulsed (distorted sinusoidal) power source and its applications using the post-discharge jet region are presented in this PhD thesis. The characterizations of the DBD system included the measurements of the direct image visualization, the electrical properties (current-voltage curve and power absorption), the optical properties (optical emission spectra and FTIR), the gas temperatures (thermocouple and optical emission spectra), and the ozone concentration. The measurements showed that abundant mestastable nitrogen [$N_2(A^3\sum_u^+)$] was generated in the pure nitrogen DBD, while abundant ozone was created as long as the oxygen was added. Specially, observation of optical emissions in the post-discharge jet region was successfully explained by several kinetic mechanisms, which is important in understanding the fundamental mechanism in surface modification. This DBD system was then applied to several important applications, which included the modification of hydrophilic property of PP film, the surface cleaning of ITO glass, the inactivation of *E. coli*, *B. subtilis* and the sterilization of *B. subtilis* spore. Results of applications showed that the developed DBD system was highly effective in these

applications under proper operating conditions, which they are briefly described in the following in turn.

For the stationary PP films, the contact angle (CA) decreases dramatically from 103° (untreated) to less than 30° (treated) with a wide range of O_2/N_2 ratios (< 1%) and treating distances (< 10 mm). In addition, the CA can still be maintained at ~40° after 24 h of the aging test. For the stationary ITO glass, show that there exists two distinct regimes with lower CAs in the range of 20-30° (84° for untreated). The first one was the regime with an oxygen addition of less than 0.05% and a treating distance in the range of 6-16 mm. The second one was the regime with an oxygen addition larger than 0.06% and a treating distance in the range of 2-10 mm. The measurements showed that: 1) in the near jet downstream location (z<10 mm), both the metastable N_2 [$N_2(A^3\sum_u^+)$] and ozone photo-induced dissociation played dominant roles in surface modification, although their relative importance was unclear and requires further investigation; and 2) in the far jet downstream location (z>10mm), when the ratio of O_2/N_2 was small, only the long-lived metastable N_2 [$N_2(A^3\sum_u^+)$] played a major role in ITO cleaning and PP film surface modification. XPS measurements showed that improved hydrophilic property was obtained after DBD jet treatment with increasing O/C ratio.

For the inactivation of *E. coli* and *B. subtilis*, the results showed that the post-discharge jet region is very efficient in inactivating these two bacteria as previous studies using the discharge region, should the working gas contains appreciable oxygen addition, which in turn generates abundant ozone. In addition, the inactivation is more effective by using compressed-air APPJ as compared to that by oxygen APPJ, possibly through the assistance of nitrous oxide existing in the former. Results of survival rate show that both *E. coli* and *B. subtilis* bacteria (up to 10^7 CFU/mL) can be effectively inactivated using less than 18 passes (1.8 seconds of residence time in total) of exposure to the post-discharge jet region of compressed air and oxygen discharges at different treating distances in the range of 4-20 mm. For the sterilization of *B. subtilis* spore, the results showed that addition of only 2% CF_4 into

the air DBD is found to be very effective, which was otherwise very ineffective using the pure air DBD. It was found that the CF_4/air (2%) APPJ treatment resulted in the efficient inactivation of the *B. subtilis* spores after 10 passes (residence time: 1.0 s) exposures for treatment distances (14 mm). Indirect evidence showed that highly reactive atoms, such as F atoms, were generated in the discharge and in the post-discharge jet region.

In conclusion, in the current thesis, a simple yet very effective planar nitrogen-based DBD system under atmospheric-pressure condition is presented and characterized experimentally. It was successfully applied using its post-discharge jet region, which was rarely seen in the literature, for surface modification and inactivation/sterilization. Recommendations for the future study are also outlined at the end of the thesis.

誌 謝

本文得以順利完成，首先要感謝指導教授 吳宗信博士四年來的悉心指導與訓練，並引導至脈衝式電源之平板型介電質常壓電漿束研究的領域，謹在此致上最誠摯的謝意。同時承蒙成功大學工科系 楊瑞珍博士、交通大學機械系 陳慶耀博士、中原大學化工系魏大欽博士、台灣大學化工系 徐振哲博士及大葉大學生科系 吳建一博士五位口試委員與國衛院醫工組 林峰輝博士提供寶貴的經驗與建議，亦深表謝意。

研究進行中，感謝洪捷粲學長，博士後研究郭啟良博士，同學孟樺、沅明，學弟育宗、逸民、皓遠、其璋、柏村、瑞祥及大葉大學生科系學弟奕宏、柏榮、峻傑，在實驗上的建議與幫忙，在此致上十分的謝意。

最後僅將本文獻給我的母親，小妹佳玲，小女彥璇及無怨無悔的老婆璧華，謝謝他們在四年求學期間給我的鼓勵與支持。

<div align="right">2010 年 6 月 28 日於新竹交通大學氣熱與電漿物理研究室</div>

Table of Contents

List of Tables

List of Figures

Nomenclature

D	Venting chamber diameter (mm)
L	Venting chamber length (mm)
E	Mean energy deposited into gas in a full cycle
P	Plasma-absorbed power
Z	Vertical direction
f	Quasi-pulsed frequency
T	Cycle time
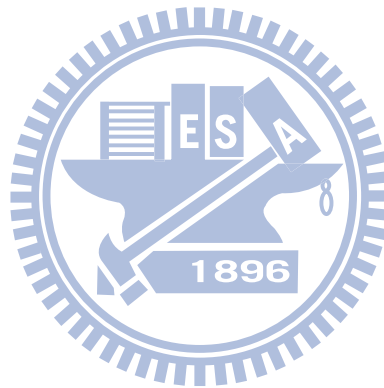
Chapter 1

Introduction

1.1 Background and Motivation

1.1.1 Advantages of Atmospheric-Pressure Discharges

Recently, atmospheric-pressure (AP) plasmas have attracted great attention [Schütze et al., 1998; Chaudhary K et al., 2003; Laroussi M et al., 2007], mainly because of their distinct advantages as compared to low-pressure plasmas. These advantages include: 1) their relatively low cost since there is no need to use expensive vacuum equipment, 2) the reduced practical operational time; and 3) the possibility for large-scale continuous in-line processing. To make the most of the AP plasmas, a thorough understanding of all aspects of AP plasmas is of critical importance, in terms of both their fundamental physics and their practical applications.

1.1.2 Classification of Atmospheric-Pressure Discharges

Atmospheric-pressure plasmas overcome the inherent disadvantages of low-pressure plasmas [Schutze et al., 1998; Becker et al., 2004; Moravej et al., 2006]. Thus, there exists great interest in atmospheric-pressure plasmas, as can be seen increasing publications from several international conferences on this subject during the past five years. There are several ways of classifying atmospheric-pressure plasmas. In this section, we have adopted the one that was adopted by Schutze et al. [1998]. Types of atmospheric-pressure plasmas include: transferred arc and plasma torch, corona discharge, dielectric barrier discharge (DBD), and atmospheric-pressure plasma jet, as shown schematically in Fig. 1-1. They are briefly introduced in the following in turn.

1.1.2.1 Plasma Torch

Plasma torch (see Figure 1-1a) is one type of thermal equilibrium plasmas, in which the temperatures of the electrons, ions and neutrals are approximately the same (10,000-20,000 K); the other three kinds are all non-thermal ("cold") non-equilibrium plasmas, in which the electron temperature (10^4-10^5 K) is much higher than that of the ions or neutrals (~300K). The former is limited in applications such as welding and gasification of materials due to its high temperature, while the latter are more widely used due to their low temperature. In addition, one of the major problems of plasma torch is the relatively short life of the electrode, caused by the discharge arc attached on it.

1.1.2.2 Plasma Jet

Atmospheric-pressure plasma jets (see Figure 1-1b) often consist of two coaxial electrodes through which a mixture of rare gases flow (He or Ar). By applying 13.56 MHz (or higher frequency) RF power to the central electrode at a voltage in the range of several hundred volts, the gas discharge can be ignited and maintained over a fairly large range of conditions. Normally, the atmospheric-pressure plasma jet is operated in the "abnormal glow" regime, in which the voltage increases with increases in current, while the low-pressure plasma is often operated in the "normal glow" regime, in which the voltage remains constant with increases in current [Schutze *et al*., 1998]. Atmospheric-pressure plasma jets have been demonstrated to be very useful in surface cleaning, thin-film deposition and biomedical applications, among others.

1.1.2.3 Corona Discharge

In corona discharges (see Figure 1-1c), plasmas are generated around the tip a

needle within a distance of ~0.5 mm, where the electric field is very large and highly

non-uniform. The corona discharge is considered a Townsend discharge or a negative

glow discharge depending on the field and potential distribution. Micro-discharges and

streamers are generated in the plasma. The operating voltage is in the range of 10-50 kV.

Major applications of the corona discharge are in the field of photocopying.

1.1.2.4 DBD

A DBD (see Figure 1-1d), which is often called a "silent discharge," consists of two

electrodes with at least one coated with dielectrics. The discharge is maintained through

a series of micro-discharges or "streamers", which last for 10-100 ns and are randomly

distributed in space and time. The operating voltage is in the range of 5-25 kV. As for N_2,

high breakdown voltage (35kV/cm) can be used in atmospheric-pressure DBD

applications within a few mm discharge gap range. Rare gases like helium and argon

have generally been used [Walsh *et al.,* 2006; Jung *et al.,* 2007] in RF

atmospheric-pressure plasma jets, dramatically increasing operating costs. Thus, the

efficient use of cheaper gases, such as nitrogen or air, has become an important issue in

practical applications. In N_2 DBD plasma, there exists abundant metastable N_2

[$N_2(A^3\sum_u^+)$]. Note that the metastable N_2 [$N_2(A^3\sum_u^+)$] energy state is 6.2 eV above

the ground state and its lifetime is ~13 sec [Fridman *et al.,* 2004]. It is very reactive

towards saturated hydrocarbons and can efficiently transfer about 6.2 eV to these

molecules to generate dissociative triplet states that break C-H (4.2 eV) and C-C bonds

(3.8 eV) [Herron 1999; Klages *et al.,* 2008].

1.1.3 Comparison of Plasma Sources

Tables 1-1 and 1-2 show summaries of the typical range of applied voltages and

plasma densities, respectively, for different plasma sources [Schutze *et al.*, 1998]. More detailed comparisons of these plasma sources, which have been omitted here for the sake of brevity, can be found in [Schutze *et al.*, 1998]. The arc and plasma torch exhibit the highest plasma density (10^{16}-10^{19} cm^{-3}) in the discharge region but, as they are types of thermal plasma, both medical and polymer material surface modification applications are limited. The DBD plasma density (10^{12}-10^{15} cm^{-3}) in the discharge region is another good choice as a non-thermal plasma source. The DBD parallel-plate-type discharge, although representing the simplest geometrical configuration, has the potential for applications that require large-area uniformity. In addition, Table 1-3 shows a summary of the typical densities of oxygen species for different types of discharges. The densities of oxygen-related species generated from DBD (e.g., 10^{18} cm^{-3} for long lifetime ozone species) are the highest for these plasmas, making them suitable for bio-medical sterilization/inactivation applications. The main types of plasma reactions are listed in Table 1-4 [Eliasson 1991].
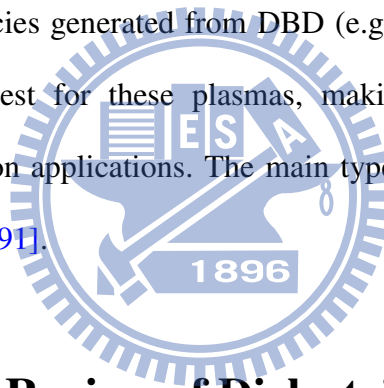
1.2 Literature Review of Dielectric Barrier Discharges

As our particular interest was in developing the DBD in atmospheric-pressure condition, the following literature surveys reflect this focus.

1.2.1 Types of DBD

A typical DBD in an atmospheric-pressure planar-electrode arrangement is as shown in Figure 1-2 [Wagner, *et al.,* 2003; Lee *et al.,* 2005]. Because of a capacitive coupling of the insulating material to the gas gap, a barrier-discharge can be driven by either an alternating feeding voltage or by a pulsed DC voltage. The high voltage is connected to the top electrode, while the bottom electrode is grounded. There are other types besides

planar electrodes, such as the cylindrical-barrier-discharges [Xu *et al.,* 2006] used for sterilization applications and pin to parallel electrodes with lower breakdown voltage characteristic for increased etching rate [Lee *et al.,* 2005]. In addition, the parallel-plate-type discharge, although having the simplest geometrical configuration, has the potential for applications requiring large-area uniformity.

1.2.2 Discharge and Post-Discharge Regions

One of the major disadvantages of AP plasma is the small distance between the two electrodes (order of mm) [Takaki *et al.,* 2005; Lee *et al.,* 2005; Laroussi *et al.,* 2004], which makes their application difficult and inflexible, although it has been shown that thin foil can still be used directly in the discharge region [Meiners *et al.,* 1998]. Thus, the use of the post-discharge jet region of atmospheric-pressure plasma may possibly remove this difficulty, although the corresponding plasma would likely be much weaker than that in the discharge, or even entirely disappear. However, the use of the post-discharge region can render the plasma source as a stand-alone module, which could be very useful in practical applications [Herrmann *et al.,* 1999; Xiong *et al.,* 2008].

1.2.3 Surface Hydrophilic Modification

PP films have found numerous applications in industry and our daily lives. Most applications requires hydrophilic surface for strong adhesion with some other surfaces. Thus, how to effectively improve the hydrophilic property of the PP film at a reduced cost becomes an important issue. In the past, most of the studies using nitrogen APPs for PP film surface modification have directly placed the test object in the discharge region [Kwon *et al.,* 2005; Wang *et al.,* 2008; Akishev *et al.,* 2008], while relatively few

have made the most of the post-discharge region. These studies have shown that the application of the nitrogen DBD discharge is relatively efficient in modifying PP film from a highly hydrophobic (90.8°) into a relatively hydrophilic state (56.5°) after a short period of exposure (e.g., 3 s) in the discharge [Morent et al., 2008]. In addition, XPS analysis has shown that when polar functional groups, such as C-O, C=O and COO, have been introduced onto the PP film surface after the AP nitrogen plasma treatment, the percentage of oxygen-containing groups has increased dramatically from 2.998% to 9.039% [Kwon et al., 2005]. Akishev [Akishev et al., 2005] argued that the polar groups were mainly formed from the abstraction of hydrogen in the secondary carbon atom, and that the formation and disappearance rate of the polar groups became equilibrated. They also found that the decomposition of the C1s peak for PET C=O/N–C=O bonds appeared and the C–O/C–N bonds proportionally increased with N_2 treatment. However, there seems to be no systematic study available for the existence of the functional groups on PP film using a post-discharge region of nitrogen APPs.

ITO coated glass is an important component in a TFT-LCD panel. Before depositing TFT thin film, effective and fast surface cleaning is necessary. In the past decade, excimer xenon-based lamps with 172 nm emission have been shown to effectively remove most of the organic compound on the ITO glass. However, the cost of operation is relatively high since the life time of an excimer lamp is comparably short (~1,000 hours) and expensive. Thus, how to effectively clean the surface of the ITO glass at a reduced cost becomes an important issue. Recently, Iwasaki et al. [2007-2008] have shown that the post-discharge region of a remote-pulse nitrogen DBD with ~0-0.2% of oxygen added, could be used for the surface cleaning of mobile ITO glass surfaces, and also that it could dramatically increase the corresponding hydrophilic property. A kinetic mechanism was proposed to elucidate the cleaning process of the nitrogen AP jet through the measured concentrations of the reactive species, including the reactive

nitrogen species (NO) and the reactive oxygen species (O, O_3), by using optical diagnostics; in their study, neither a detailed description of the pulsed power supply (e.g. voltage waveform and discharge current) nor the quality of the discharge gases were provided. In addition, the measured OES data seemed not properly interpreted through any plausible kinetic mechanisms. Thus far, no other study has systematically verified the results or investigated the effect of the treatment distance (between the exit of the DBD and the surface to be cleaned or treated), both of which are important in practical applications.

1.2.4 Bacteria Sterilization/Inactivation

Conventional sterilization technologies, such as autoclaves, ovens, chemicals such as ethylene oxide (EtO), and radiation (gamma rays) [Holyoak *et al.,* 1996; Lucas *et al.,* 2003] heavily rely on the irreversible metabolic inactivation or breakdown of vital structural components of microorganisms. Although some of these methods which apply direct heating may be effective in inactivating microorganisms, they are often highly inefficient in terms of time and cost (high energy consumption). Sterilization/inactivation using non-thermal plasmas represents one of the most promising technologies. Most applications of plasma technology for sterilization/inactivation require the direct contact of the discharge with the bacterial cells [Moisan *et al.,* 2001] because abundant chemically active ions, electrons and radicals exist in the discharge. The use of low-pressure plasma may be helpful, whereby the electrode distance can be quite large. A larger space between the electrodes in low-pressure plasmas means easier handling of the treated bacteria, as compared to those using atmospheric-pressure plasmas [Deng *et al.,* 2006; Laroussi *et al.,* 2002], in which the electrode distance is very small (order of mm). However, handling the test

pieces requires the break of the vacuum, which is costly and time-consuming.

Deng *et. al* has show a 10-min exposure to the atmospheric-helium plasma plume led to a 4-log reduction of the *Bacillus subtilis* spores, whereas the use of the less than 0.2-log reduction [Deng *et al.*, 2006]. Lee *et. al* has show D-values were 14 min for B. subtilis spore. The sterilizing effect of the Atmospheric-pressure cold helium/oxygen plasma is not due to UV light, which is known to be the major sterilization factor of APCP, but instead results from the action of reactive oxygen radicals [Lee *et. al*, 2006]. Lerouge's group investigated *B. subtilis* spore sterilization by O_2/CF_4 plasma under low-pressure condition, which exhibited much higher efficacy than all other gases or gas mixtures tested (O_2, O_2/Ar, O_2/H_2 and CO_2), with more than a 5 log decrease in 7.5 min, as compared with a 2 log decrease with pure oxygen at an operation pressure of 80 mTorr [Lerouge *et al.*, 2000]. Note *B. subtilis* spore represents one of the toughest organisms, which can tolerate extreme environmental conditions for more than 10 years, and has been often used as a target bacterium to test whether the sterilization method is effective or not. However, the creation of low-pressure plasmas requires the use of vacuum equipment, which is very expensive and rather impractical in bio-medical applications.

Recently, sterilization/inactivation using non-thermal atmospheric-pressure plasmas (APP) has attracted tremendous attention [Sharma *et al.,* 2006; Sun *et al.,* 2007]. The major advantages of applying atmospheric-pressure plasmas may include, among others [Hippler *et al.,* 2008]: 1) generating abundant bactericidal active agents (chemically active radicals, high kinetic energy ions, electrons, and UV photons); 2) producing a fairly low-temperature gas stream which is in direct contact with the bacteria or container; 3) a shorter operating time in the order of seconds or minutes; 4) easy removal of inactivated bacteria and viruses on the treated surface through jet gas streams; and 5) producing essentially no hazardous substances.

1.3 Specific Objectives and Organization of the Thesis

Based on the preceding discussion of the related studies of DBD atmospheric-pressure plasma, it was clear that further experimental study was needed to provide a better fundamental understanding of the properties of DBD atmospheric-pressure plasma and will thus lead to more effective applications.

Therefore, the specific objectives and organization of this thesis were summarized as follows:

1. To develop a parallel-plate DBD operating under the atmospheric-pressure condition that is driven by a high-voltage bipolar quasi-pulsed power supply. (Chapter 2)

2. To study nitrogen-based and air-based DBD planar plasmas, which include measuring the electrical properties of the discharges, the spectrum intensity distributions and temperature distributions in the post-discharge region, to name a few. (Chapter 3)

3. To interpret the measurements in Item No. 2 to understand the plasma physics in the discharge and post-discharge jet regions. (Chapter 3)

4. To study the surface modification of PP film by applying the post-discharge jet region of a nitrogen-based planar DBD. The effects of oxygen addition into the nitrogen DBD and treating distance between the DBD and PP film on the hydrophilic properties were investigated, including the surface hydrophilic properties, roughness and chemical composition (elements and functional groups). Optical emission intensity from the excited species and ozone concentration in the post-discharge region were measured and then used to explain the measured contact angles for the stationary and non-stationary PP

films. (Chapter 4)

5.   To study nitrogen, DBDs with and without the addition of trace oxygen were then applied to clean stationary and non-stationary ITO glass using the post-discharge jet region at different treating distances. Measurements of the concentrations of several reactive species at various spatial locations under different levels of oxygen addition to nitrogen were then used to elucidate the cleaning process. (Chapter 5)

6.   To apply a parallel-plate DBD atmospheric-pressure plasma jet (APPJ) to inactivate two typical bacteria, *E. coli* and *B. subtili,* in the post-discharge jet region. Various inexpensive working gases, including pure N_2, pure O_2 and compressed air, were tested and the discharges were characterized accordingly. (Chapter 6)

7.   To apply a parallel-plate DBD atmospheric-pressure plasma jet (APPJ) to inactivate *B. subtilis* spore in the post-discharge jet region. Various working gases, including compressed air and air mixed with Carbon Fluorine (CF4), were tested and the discharges were characterized accordingly. (Chapter 7)
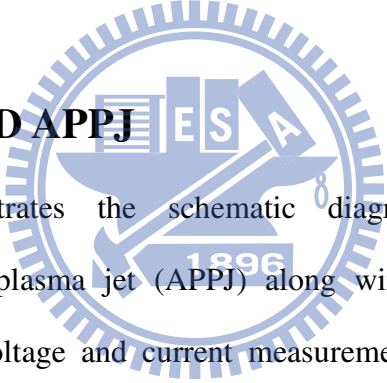
Chapter 2

Experimental Methods

2.1 Test Facility

The test facility for a planar DBD APPJ measurement in this study included: a planar DBD APPJ, cooling system, distorted sinusoidal voltage (quasi-pulsed) power supply, gas supply system, venting chamber and non-stationary stage. Table 2-1 summarizes various components of the DBD system. Each of these arrangements is described in the following in turn.

2.1.1 Planar DBD APPJ

Figure 2-1 illustrates the schematic diagram of a parallel-plate DBD atmospheric-pressure plasma jet (APPJ) along with a gas supply system and the instrumentation for voltage and current measurements. This APPJ consisted of two parallel copper electrodes (50 × 50 × 8 mm each) with embedded cooling water. Each electrode was covered with a ceramic plate 70 × 70 × 2 mm for the inactivation/sterilization application, and a quartz plate 70 × 70 × 1 mm for the surface hydrophilic modification application. The 5 mm dielectric plates extruded from the end of the electrodes (in the flow direction), and prevented the electrode assembly from arcing. The distance between the two dielectric plates (ceramic/quartz) was 1 mm throughout the study. The assembly of electrodes and dielectrics was then covered by a Teflon insulation layer to provide safety and prevent arcing problems during operation.

2.1.2 Cooling System

The water flow of the cooling electrode was delivered by a cooling system. The inlet cooling temperature control was $20 \pm 2°C$ for the electrode and the water pressure control was 1.6 ± 0.1 kg/cm^2. The high voltage and ground electrode used separate cooling pipes which are controlled separately. The diameter of the cooling pipe was 1/4".

2.1.3 Distorted Sinusoidal Voltage Power Supply

This DBD assembly was powered by a distorted sinusoidal voltage (quasi-pulsed) power supply (Model Genius-2, EN Technologies Inc.). This power supply facilitated the adjustment of the frequency (20~60 KHz), power density (low/middle/large), peak current (max. 4A), peak voltage (max. 15 kV), and power (max. 2 kW). The distorted sinusoidal voltage power facilitated generation of high voltage with high dv/dt to enhance the discharge intensity and thus radical generation. Another feature of the output electrical waveform is the distorted sinusoidal voltage waveform which can minimize the occurrence of arc (or streamer) to ensure stable power output according to asymmetric load and sudden load change caused by the plasma.

2.1.4 Gas Supply System

Various working gases flowed between the parallel plates, including N_2 (99.99%), O_2 (99.99%), O_2/N_2 (0.004-1.6%), O_2 (99.99%), compressed air (produced from an oil-less compressor) and CF_4/air (2% of CF_4). The flow rates were controlled by manually adjustable flowmeters. The gas was introduced through two holes at the top of the parallel plate assembly and then passed through a sieved aluminum plate containing 480 holes (0.5 mm in diameter each) for pressure redistribution, followed by a convergent section with a length of 10 mm to coincide with the channel gap size (1 mm)

at the end of the section.

2.1.5 Venting Chamber

In setting up the planar DBD APPJ in a venting chamber for operation safety, the cylindrical chamber size was **D**600 × **L**700 (mm), as shown in Figure 2-2. The planar DBD APPJ was mounted on the top side of the chamber. The exhaust pipe (diameter 210 mm) was mounted on the bottom side of the chamber. The venting flow was produced by a variable blower which was driven by a 1 HP-3phase induction motor (Tatung EBFC) with frequency converter (TECO 7300CV, 1~60 Hz). The blower (frequency 8 Hz) remained on during the experiments as the flow is introduced into the chamber.

2.1.6 Non-Stationary Stage

For the surface treatment, the distance between the bottom edge of the planar DBD and the sample varied in the range of z=2~20 mm; "z" denotes the coordinate in the downstream direction measured from the bottom edge of the DBD assembly throughout the thesis. The sample was either stationary or transported by a pre-programmed non-stationary stage (Unice E-O Service Inc., U-S1-D0-H080378, maximum traveling distance 20 cm, USB driver). The stage plate size was 10×10 cm. The non-stationary variable speed of the sample passing the DBD jet was in the range of 1-9 cm/s. We could preset the passes of the sample treatment using the pre-programmed non-stationary stage.

2.2 Instrumentation

The instruments for a planar DBD APPJ measurement in this study included thermocouples for post-discharge gas temperature measurements, the measurement of

electric properties, the OES for optical spectral measurements, the FTIR for gas and surface sample analysis, contact angles for surface energy measurements, AFM for surface profile measurements, SEM for bacteria morphological observation, visualization of planar DBD APPJ and the sample preparation of bacteria. Table 2-2 summarizes various instruments which were used for the measurements. Each of these arrangements is described in the following in turn.

2.2.1 Thermocouples for Post-Discharge Gas Temperature Measurement

The gas temperatures in the post-discharge jet region were measured using a K-type (-50-500 ℃) thermocouple, which was fixed on a non-stationary stage. The thermocouple was connected to a digital indicator (Brainchild BTC-900) for temperature display.
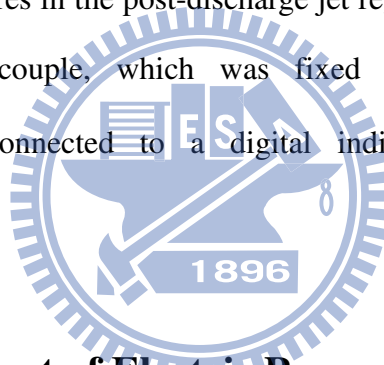
2.2.2 Measurement of Electric Properties

2.2.2.1 Current and Voltage Waveforms

Input voltage and output current waveforms across the electrodes of the parallel-plate discharges were measured by a high-voltage probe (Tektronix P6015A) and a current monitor (IPC CM-100-MG, Ion Physics Corporation Inc.), respectively, through a digital oscilloscope (Tektronix TDS1012B). The current monitor was of the Rogowski coil type. The output sensitivity was 1 volts/Amp, and the diameter of the hole was 0.5 inch to suit the insulating power cable. The Rogowski coil used for fast current changing measurement was proved to be better than the Hall-effect device in terms of sampling speed and accuracy.

2.2.2.2 Power Absorption Estimation based on Lissajous Figure

Plasma power absorption was measured by the technique of the "Lissajous figure" (Q-V characteristics) [Wagner *et al.,* 2003] using a capacitor with a capacitance of C_m=6.8 nF and a voltage probe (Tektronix P2220).

Figure 2-3 shows the typical Lissajous figure obtained for a DBD. The shape of the Q-V curve is a distorted version of the standard parallelogram [Wagner *et al.,* 2003] observed in a DBD driven by a sinusoidal AC power source. The electrical energy consumed per voltage cycle, *E,* and the plasma absorbed power, *P,* were estimated by the following relations [Wagner *et al.,* 2003]:

$$E = \oint V(t)dQ \equiv \text{area of (Q-V) diagram} \tag{1}$$

$$P = \frac{1}{T}E = fE \tag{2}$$

where *f* is the frequency of the distorted sinusoidal voltage.

2.2.3 OES for Spectral Measurements

The spectral optical emission intensities of the APPJ were measured using a monochromator (PI Acton SP 2500) with a Photomultiplier tube (Hamamatsu R928), which was mounted on a mobile 3-D table (see Figure 2-4). The spectral range was 180~900 nm with 1200-g/mm grating (Holographic, 300-nm Blaze and 500-nm Blaze). When the center wavelength of the emission line is 400 nm the linear dispersion is 1.489 nm/mm. Both sides of the fiber (Ocean Optic. BTW-FPC-600-0.22-1.5-UV, 600 μ m) were separately connected to the SMA adapter of the monochromator and the collimating lenses (Ocean Optics 74-UV).

2.2.3.1 Species Identification

Measured optical spectra were used to determine the types of species in the

discharge and post-discharge jet region. In addition, the absolute intensity was proportional to the number density in the region of interest. One aspect of OES measuring is identifying which particle species emits radiation. From the line position, the wavelength is a characteristic of an element/compound; it is sufficient to use a wavelength calibrated (survey) monochromator in combination with wavelength tables for atoms, ions and molecules [Fantz 2006]. A spectroscopy software package, named Plasus SpecLine, was used to evaluate the spectral data, i.e. finding specific lines in the spectra (ex. Figure 2-5) and excited species level change (ex. Table 2-3), and identifying unknown peaks or comparing data from the OES measurements.

2.2.3.2 Gas Temperature Measurements

Metastable states of molecules play an important role in different discharges due to their ability to accumulate a great amount of energy, which can be effective in various chemical and physics processes. For example, from measured line intensities, the concentrations of NO as functions of the average discharge power and estimations of the electron density in the discharge could be derived. Variations in the measured rotational temperature of NO-γ (245-249 nm) can be attributed to changes in the gas heating and, consequently, the gas dynamics in DBD. Since the collision frequency is very high in a DBD under atmospheric-pressure condition, we can assume thermal equilibrium between translational and rotational temperatures. Therefore, in the spectrum of NO-γ transition, the rotational distribution of excited emission ($N_2(A^3\sum_u^+) + NO(X^2\prod) \rightarrow NO(A^2\sum^+) + N_2(X^1\sum_g^+)$) corresponds to the ambient gas temperature [Bibinov *et al.,* 2000]. We used LIFBASE [Luque *et al.,* 1999] to simulate gas temperature in the discharge region (ex. Figure 2-6) throughout the study.

2.2.3.3 2nd Order Radiation in OES spectra

Diffraction gratings produce a multiple order of diffracted light where constructive interference permits the light of one wavelength to appear at more than one angle of diffraction. For example, 236 nm light passing through a monochromator normally appears as 236nm "first order" light. Some of the 236nm light will also appear at 472nm as "second order" light and so on. We removed second order emission lines from measured OES spectra by long-pass filter verification. See Appendix A for details.

2.2.4 Measurement of Ozone Concentrations

2.2.4.1 Ozone Monitor

The concentrations of ozone were measured using an ozone monitor (API Model 450) which was mounted on a mobile 3-D table in the post-discharge jet region. The detection of ozone molecules is based on the absorption of 254 nm UV light due to an internal electronic resonance of the ozone molecule. The API Model 450 used a mercury lamp so that a large majority of the light emitted was at the 254nm wavelength. The operation range was 1 to 1000 ppm. The O_2/N_2 (<1.6%) DBD plasma produced a concentration of ozone well under 1000 ppm based on our measurements. However, as the oxygen exceeds some amount, the concentration of ozone is over the range of the ozone monitor and cannot be measured properly.

2.2.4.2 FTIR

Infrared spectroscopy exploits the fact that the chemical bounds of molecules have specific frequencies at which they rotate or vibrate corresponding to discrete energy levels (vibrational modes). In order for a vibrational mode in a molecule to be IR active, it must be associated with changes in the permanent dipole. Ozone belongs to the dipole molecule (106.8°). In pure O_2 and compressed air DBD plasma, the ozone concentration

is over 1000 ppm, which renders the above-mentioned ozone monitor inappropriate. The ozone infrared spectrum absorbance of the APPJ was measured using a FT-IR spectrometer (Bruker Tensor 27). For example, Figure 2-7 shows the infrared absorption spectra (800-3600 cm^{-1}) of the planar air DBD APPJ. A strong absorption peak of 1055 cm^{-1} for the ozone was clearly observed in the compressed air discharges because of abundant oxygen species in the discharges. We defined the 1055 cm^{-1} line intensity of IR spectrum as the relative ozone concentration in the post-discharge jet region.

2.2.5 Contact Angles for Surface Energy Measurement

The hydrophilic property (contact angle) of the PP film and the ITO glass surface were measured using a contact angle machine (KRŰSS GH100) with a 2 μL drop of de-ionized water placed on the glass surface using a micropipette. The values of the static contact angle were obtained using Laplace-Young curve fitting to measure the 10 average values in the plasma treatment region.

2.2.6 AFM for Surface Profile Measurement

The AFM images for measuring the roughness of the sample surface were obtained using a Veeco Dimension 5000 Scanning Probe Microscope (D5000).When the probe scan is near the sample surface, the probe with sample interaction force reflects testing-arm deformation through laser-beam detection and feeds the information to a PC. The Z-axis information showed the roughness of the sample, and the X-axis and Y-axis showed the AFM scanning area. Three sets of data can be output: 2D/3D morphology, step profile, and roughness analysis.

2.2.7 SEM for Bacteria Morphological Observation

The bacteria of the control (untreated) and the plasma-treated samples were rinsed with distilled water and fixed with 2.5% glutaraldehyde solution overnight. The fixed bacteria were dehydrated in a series of graded acetone concentrations and then dried in a CO_2 atmosphere (HCP-2, Hitachi, Japan) under critical conditions, and then coated with a thin layer of gold. The effects of the plasma treatment on the structure of the bacteria were examined using a scanning electron microscopy (Hitachi S-470 type II, electron voltage: 5kV, amplification factor: 30k).

2.2.8 XPS for Surface Chemical Composition

The surface chemical composition of the PP film and ITO glass before and after application of the AP plasma jet was measured using an X-ray photoelectron spectrometer (PHI Quantera SXM, Scanning Monochromated Aluminum anode, chamber pressure below 5×10^{-10} torr for ITO glass; ESCA PHI 1600, Mg anode at 250W and 15KV, 1253.6 eV, the electron take-off angle respect to the PP film surface was 45°, chamber pressure below 2×10^{-8} torr for PP film).

2.2.9 Visualization of Planar DBD APPJ

The different discharge images of the planar DBD APPJ were taken using a digital camera (Nikon D1H) and lens (Nikon Micro-Nikkor 105mm f/2.8). The image sensor was 12-bit RGB CCD with 2.74 million pixels. The typical images of the post-discharge region for DBD plasma were taken after 0.2 sec (side view: width 1mm) and 2 sec (front view width: 50 cm) of exposure. The typical images of the discharge region for DBD plasma were taken after 0.2 sec of imaging.

2.2.10 Sample Preparation of Bacteria

2.2.10.1 *E. coli* **and** *B. subtilis*

E. coli (BCRC 13014) and *B. subtilis* (BCRC 14716) cultures were grown in 100 mL of nutrient broth which was maintained for 12 h and 18 h at 37∘C, respectively. This allowed the bacteria to reach the exponential-log phase. Bacteria (10 mL) were harvested and transferred from the broth under sterile conditions to the phosphate buffer solution (90 mL and pH 7.0). The solution was then diluted further to the required concentration level (3.2×10^7 CFU/mL), which was very high as compared to previous studies [Sun *et al.,* 2007]. Then 0.1 mL of the diluted solution was added to sterile petri dishes (diameter 80 mm) containing 20 mL of nutrient agar, and spread on the central area of the petri dishes (4 cm × 4 cm) to ensure that all bacteria were treated by a plasma jet 5 cm in width. During the bacteria preparation, we made sure that the petri dishes were level in order to prevent any of the bacteria flowing out of the central area of the petri dish. The petri dishes with nutrient agar were exposed to the parallel-plate DBD APPJ following the planned test conditions, as will be shown later. After the plasma jet treatment, the petri dishes were incubated at 37°C for 24 h, prior to determining the resulting number of colony-forming units (CFU/mL) by NIH ImageJ [Sheffield *et al.,* 2007]. This software can easily calculate the area of grown bacteria based on a pixel count, which resulted in the survival rate of the bacteria in the petri dish.

2.2.10.2 *B. subtilis* **Spore**

B. subtilis (BCRC 14716) precultures were grown in 100 mL of nutrient broth which was maintained for 18 h at 37℃; then 0.1 mL culture suspension was added to sterile petri dishes containing 20 mL of nutrient agar (beef extract, 3 g/liter; peptone, 5 g/liter; agar, 15 g/liter; with the pH adjusted to 6.8±0.2). After being incubated at 37℃ for 2 weeks, the sporulated bacteria were collected by suspension in approximately 5 mL of

water per plate. The spores were washed five times by centrifugation and suspension in sterile water, and finally stored at 4℃ in water at concentrations of about 1.24×10^9 spores/mL, diluted according to the demand thickness of the experiment. Then, 0.1 mL of the diluted solution was added to sterile petri dishes (diameter 80 mm) containing 20 mL of nutrient agar and spread on the central area of the petri-dishes (4 cm × 4 cm) to ensure that all bacteria were treated by a plasma jet 5 cm in width. During the bacteria preparation we made sure that the petri dishes were level; otherwise, some bacteria would flow out of the central area of the petri dish. The petri dishes with nutrient agar were exposed to the parallel-plate DBD APPJ following the planned test conditions, as will be shown later. After the plasma jet treatment, the petri dishes were incubated at 37°C for 24 h, prior to determining the resulting number of spore (spore/mL) by NIH ImageJ, which was described earlier.

2.3 Test Conditions

The test conditions for the planar DBD APPJ measurements in this study included surface modification applications and bacteria sterilization/inactivation applications. Each of these test conditions has been summarized in Tables 2-4 – 2-7.

2.3.1 Surface Modification Applications

2.3.1.1 PP Film Modification

Various working gases flowed between the parallel plates, including N_2 (99.99% purity) and its mixture with trace oxygen (99.99% purity) with different volume fractions in the range of 0.004-1.6%. The flow rates were controlled by manually adjustable flowmeters. The total flow rate was fixed at 50 slm throughout the study. The output power from the power supply was fixed at 500 W (plasma-absorbed power: 175

W). For the PP film treatment, the distance between the planar-DBD APPJ bottom edge and the PP film was varied, while the PP film (0.31 mm in thickness, density of 0.91~0.92 g/cm^3, Nan-Ya Inc.) was either stationary or transported by a pre-programmed non-stationary stage. The moving speed of the PP film was in the range of 0.5-8 cm/s throughout the study. The testing conditions of the PP film modification have been summarized in Table 2-4.

2.3.1.2 ITO Glass Surface Cleaning

Discharge gases, which included pure nitrogen (99.99%) and mixtures of gases with 0.004~1% of oxygen in nitrogen flowed from the top to the bottom between the parallel plates for the ITO glass surface treatment under the conditions of 60 kHz (power supply), 50 slm (flow rate) and 175 W (plasma absorbed power). In addition, the gas temperatures (measured by a K-type thermocouple) in the jet region (z=2~20 mm) were generally low in the range of 50-80°C under the typical operating condition, which was safe for ITO glass cleaning and other applications. The data on the contact angle for the stationary case presented here were obtained after 5 s of plasma jet stream impinging onto a stationary ITO glass. The non-stationary speed of the ITO glass passing the DBD jet was in the range of 1-9 cm/s. The testing condition of ITO glass surface cleaning has been summarized in Table 2-5.

2.3.2 Bacteria Sterilization/Inactivation Applications

2.3.2.1 *E. coli* and *B. subtilis*

Various working gases flowed between the parallel plates, including N$_2$ (99.99%), O$_2$ (99.99%) and compressed air (produced from an oil-less compressor). The flow rates were controlled by manually adjustable flowmeters. For clarity of presentation, all of

the results presented in this paper were performed under the conditions of 30 kHz (power supply) and 10 slm (flow rate). The petri dishes which contained the bacteria were transported by a pre-programmed moving stage. For the treatment of the bacteria, the distance between the bottom edge of the planar DBD and the bacteria varied in the range of z=4-20 mm. The moving speed of the petri dishes was kept at 1 cm/s and the number of passes of the DBD jet pass varied in the range of 1-18. Note that "a pass" is defined as the motion of the APPJ traveling back and forth over the petri dish. Resulting residence time over the petri dish was 0.1 s for a pass under the designated speed, assuming the jet width is 1 mm at the impinging point. In addition, the gas temperatures in the post-discharge jet region were measured using a K-type thermocouple, which was fixed on a moving stage. The testing conditions of the *E. coli* and *B. subtilis* inactivation have been summarized in Table 2-6.

2.3.2.2 *B. subtilis* Spore

Various working gases flowed between the parallel plates, including compressed air (produced from an oil-less compressor) and CF_4/compressed air (2%). The flow rates were controlled by manually adjustable flowmeters. For clarity of presentation, all of the results presented in this paper were performed under the conditions of 30 kHz (power supply) and 5 slm (flow rate). The petri dishes which contained the bacteria were transported by a pre-programmed moving stage. For the treatment of *B. subtilis* spore, the distance between the bottom edge of the planar DBD and the bacteria was fixed at 14 mm. The moving speed of the petri dishes was kept at 1 cm/s and the number of passes of the DBD jet pass varied in the range of 1-18. Resulting residence time over the petri dish was 0.1 s for a pass under the designated speed. In addition, the gas temperatures in the post-discharge jet region were measured using a K-type thermocouple which was fixed on a moving stage. The testing conditions of *B. subtilis*

23

spore inactivation have been summarized in Table 2-7.
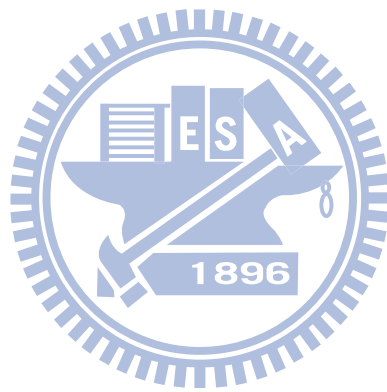
Chapter 3

Characterization of the DBD APPJ

In this chapter, the measurements of the characteristics of the planar DBD system are presented in detail. They include: 1) Visualization of the post-discharge jet region; 2) electrical properties; 3) Optical properties and 4) Ozone concentration, which are described in the following in turn.

3.1 Visualization of the Post-Discharge Region

Figure 3-1 shows the typical images of the post-discharge region for N_2 and N_2+0.06% O_2 discharges under the conditions of 50 slm, 60 kHz and 500 W, which were taken after 0.2-2 s of exposure. For a pure nitrogen discharge, the plume extended over a longer distance (~ 2.5 cm) and had a yellow-orange color. When the plume became even shorter (~ 1 cm) it had a blue color with 0.06% of trace oxygen addition. These color changes could be clearly explained from the OES measurement, as shown in Figure 3-8b, which shows the optical emission spectra in the visible range obtained in the post-discharge region. It was readily apparent that as 0.06% oxygen was added: the blue lines were greatly enhanced, which led to the observed blue plume. Also, it was interesting to observe that as 1.6% oxygen was added, most of the optical emissions in the visible range diminished, which resulted in an invisible plume.

Figure 3-2 shows the bottom view of the discharge region for N_2, O_2, and compressed air plasmas, respectively, under the conditions of 10 slm, 30 kHz and 300 W taken after 0.2 s of exposure. The image of the nitrogen discharge was a very bright and uniform blue color, which was mainly caused by the fluorescence of short-lived

excited nitrogen ($N_2\left(B^3\prod_g\right)$ and $N_2\left(C^3\prod_u\right)$) [Akishev *et al.,* 2008]. The oxygen plasma was a typical electronegative discharge, but its image was much darker than other gas discharges that contained nitrogen. In addition, the micro-discharges were clearly seen in the images of the compressed air and oxygen discharges, which were essentially filamentary-like. This also resulted in rapidly oscillating discharge currents as shown in Figures 3-7a and 3-7b.

Figure 3-3 shows the side view of the post-discharge regions for N_2, O_2 and compressed air discharges, respectively, under the conditions of 10 slm, 30 kHz and 300 W. For the pure nitrogen case, the colorful plume was ~ 1.5 cm in length, with a yellow to orange color, which was mainly caused by the fluorescence of the N_2 first positive lines metastable nitrogen $N_2(B^3\prod_g) \rightarrow N_2(A^3\sum_u^+)$ (500-700 nm). For the discharges generated by pure oxygen and compressed air, the plumes were hardly visible because most of the metastable nitrogen was quenched by the oxygen. In addition, the color was clearly confirmed from the OES measurements, as shown in Figure 3-10, which is described in detail in later section.

3.2 Electrical Properties

3.2.1 Current and Voltage Waveforms

Figure 3-4 shows the typical measured input voltage (60 kHz) and discharge current waveforms under the conditions of 50 slm (flow rate of N_2) and 500 W (the output power from the power supply). The pulsed width was approximately 3 μs. The results showed that the discharge current increased rapidly as the voltage exceeded some value (~4 kV) and decreased rapidly as the voltage further increased to some level. The rapid decrease of the current was mainly due to the charge accumulation on the dielectric

surface, which is a well-known mechanism of DBD to prevent the discharge from arcing. It was also interesting to observe that the current changed direction from positive to negative as the applied voltage reached the maximal value (~8.5 kV). After the pulse, the filament current oscillated between positive and negative values at a lower voltage, mainly because of the displacement current (large rate of change of applied voltage). The measured peak current for N_2 was approximately 0.45 A for 25 cm^2 of the discharge area, which was equivalent to ~0.018 A/cm^2 in terms of current density. Note this corresponds to a typical value of current density of the so-called Townsend-like discharge [Choi *et al.*, 2006].

Figures 3-5(a)-(c) show the typical measured distorted sinusoidal voltage (30 kHz) input voltage to the electrodes and the discharge current waveforms produced in the DBD using pure N_2, pure O_2, and compressed air of 10 slm, in which the output power from the power supply was kept constant (300 W). It was clear that the discharge of N_2 (see Figure 3-5a) was nearly homogeneous based on the current waveform, while those of pure O_2 (see Figure 3-5b) and compressed air (see Figure 3-5c) were filamentary-like. These can also be further verified from Figure 3-2, which illustrates a series of discharge images of these gases. The measured peak current was approximately 400 mA for 25 cm^2 of the discharge area, which was equivalent to ~16 mA/cm^2, which is slightly less than 18 mA/cm^2 when the driving frequency is 60 kHz, as presented earlier. One-dimensional fluid modeling for nitrogen DBD driven by a sinusoidal voltage waveform [Choi *et al.,* 2006] and by the same quasi-pulsed (distorted sinusoidal) waveform [K.-W. Cheng *et al.*, 2010] have both shown that it is a typical Townsend-like discharge for gap distance of 1 mm, in which the electron number density is much less than that of the ion number density (N_2^+ and N_4^+) and very abundant long-lived metastable nitrogen are generated. Details of the fluid modeling of nitrogen [K.-W. Cheng *et al.*, 2010] are beyond the scope of the current study and are skipped here for

brevity. Discharges using pure O_2 and compressed air were more filamentary-like than pure N_2 discharges, as confirmed from the rapid oscillating currents in Figures 3-5b and 3-5c, and also the images of the micro-discharge in Figure 3-3.

3.2.2 Power Absorption Estimation Based on Lissajous Figures

Figure 3-6 shows the typical Lissajous figure obtained for the same test conditions as shown in Figure 3-4. The shape of the Q-V curve was a distorted parallelogram [Wagner *et al.,* 2003] as observed in a DBD driven by a sinusoidal AC power source. The results showed that as the voltage reached the peak value (~8.5 kV), the maximal effective charge (~350 nC) across the electrodes was obtained, which extinguished the discharge (zero current) caused by the shielding effect, as observed in Figure 3-4. As the voltage continued to decrease, the effective charge began to decrease, as had been expected. The estimated plasma absorbed power in this case was 175 W with an efficiency of about 35%.

Figure 3-7 shows the typical Lissajous figure obtained for the same test conditions as in Figure 3-5. Accordingly, for the corresponding N_2, O_2 and compressed air discharges, the estimated absorbed plasma power was 88.6W (28%), 86.4W (28.8%) and 83.5W (27.8%), respectively, where the percentage in each parenthesis represents the ratio of absorbed power to input power. Note that the input power was directly read from the power supply.

3.3 Optical Properties

3.3.1 Species Identification

3.3.1.1 Nitrogen-Based DBD APPJ

Figures 3-8(a)-(b) show the measured optical emission spectra in the range of 180-900 nm in the post-discharge region. In the discharge region, the addition of 0.06% O_2 reduced the production of $N_2\left(C^3\prod_u\right)$ [$N_2 + e \rightarrow N_2\left(C^3\prod_u\right) + e$] because of the reduced electron number density due to the high electron affinity of oxygen. Hence, in the post-discharge region, the emission line intensity for the N_2 second positive [$N_2\left(C^3\prod_u\right) \rightarrow N_2\left(B^3\prod_g\right) + h\upsilon\ (337.1\ nm)$] decreased accordingly (see Figure 3-8a). However, the addition of 0.06% O_2 increased the amount of ground-state NO and, thus, $NO\left(A^2\sum^+\right)$ and $NO\left(B^2\prod\right)$ [through $NO + N_2\left(A^3\sum_u^+\right) \rightarrow NO\left(A^2\sum^+\right)$ and $NO + N_2\left(A^3\sum_u^+\right) \rightarrow NO\left(B^2\prod\right)$]. Hence, in the post-discharge region, the NO-γ, the NO-β and the N_2 first positive (Lewis-Rayleigh afterglow) emission line intensities increased through [$NO\left(A^2\sum^+\right) \rightarrow NO + h\upsilon\ (180-260nm)$], [$NO\left(B^2\prod\right) \rightarrow NO + h\upsilon\ (260-380\ nm)$] and [$N + N + N_2 \rightarrow N_2\left(B^3\prod_g\right)$ and $N_2\left(B^3\prod_g\right) \rightarrow N_2\left(A^3\sum_u^+\right) + h\upsilon\ (580\ nm)$], respectively. In the above, the increase of the N_2 first positive line intensity (580 nm) was mainly caused by the increase of N atoms through the reaction channels in the discharge region, such as $e + N_2 \rightarrow N_2(a'^1\sum_u^-) + e$ and $N_2(a'^1\sum_u^-) + NO \rightarrow N + O + N_2$ with 0.06% addition of O_2. As more O_2 was added, all line emission intensities decreased because of the reduced plasma (thus, electron) intensity in the discharge region [Golubovskii *et al.,* 2002; Brandenburg *et al.,* 2005; Golubovskii *et al.,* 2004; Guerra *et al.,* 2001; Dilecce *et al.,* 2007].

In addition, the emission intensity of 236.6 nm was the highest among these emission lines, which was similar to earlier observations [Iwasaki *et al.,* 2007]. For a clear picture of how the UV emission intensity (e.g. 236.6 nm) varied with its position in the post-discharge region and the concentration of oxygen addition into the nitrogen

discharge, we have summarized the measurements in Figure 3-9. Figure 3-9 shows that UV emission generally increased with increasing amounts of trace oxygen addition and reached a maximal value with only 0.06% oxygen addition. Note that the NO-γ emission was appreciable even with the "pure" nitrogen case since there are always impurities (oxygen) in commercial nitrogen bottles. Further addition of O_2 (> 0.06%) greatly reduced the UV emission, which was probably caused by the very high electron affinity of oxygen that can appreciably reduce the amount of excited nitrogen [$N_2(A^3\sum_u^+)$]. In addition, the UV emission generally decreased rapidly with increased downstream distance from the channel exit, probably because of dramatically decreasing amounts of excited nitrogen as it was quenched by entrained ambient air. Note detailed reaction channels related to nitrogen, oxygen or mixture of both are summarized in Table A-1 for reference. However, these could be clarified using some simulation techniques such as fluid modeling coupling with a flow solver, which is currently in progress in our group.

3.3.1.2 Air-Based DBD APPJ

3.3.1.2.1 Pure Air DBD

Figure 3-10 shows the optical emission spectra in the UV and VIS regions measured in the post-discharge region. UV emission was greatly reduced because of the strong electro-negativity of O_2 gas, as mentioned earlier. Detailed plasma chemistry using more detailed measurements or simulations would be a worthy topic of study in the near future. In addition, in the range of 450-550nm, emission of the nitrogen discharge was much stronger than for either pure oxygen or compressed air, which caused the yellow-orange plume as observed in Figure 3-3.

3.3.1.2.2 Air/Carbon Fluorine Mixture DBD

Figure 3-11 shows the optical emission spectra in the 180-380 nm region measured in the discharge region with air and CF4/air (2%) DBDs. The 180-280 nm UV emission almost disappeared because of the strong electro-negativity of O_2 gas for both cases. In addition, in the range of 300-380nm, the peak lines of emission were similar to the compressed air and CF_4/air (2%) discharges. Obviously, there are no lines related to F atom and CF_x (x=1-3) fragments in the OES data mainly because the excitation energy of F atoms is very high (between 14.37 and 14.75 eV) and it is impossible for the low-energy electrons to excite the F atoms. However, there have been some studies showing that it was possible to find CF_2 fragment in the range of 240-360 nm if the argon and small amount of CF_4 are used as the discharge gases of a DBD [Fanelli F, 2009]. This was probably caused by the abundant metastable argon having higher excitation energy (11.55-11.72 eV), which dissociated the CF4 more easily than by the electrons themselves. However, more studies are required to understand the observed phenomena.

3.3.2 Gas Temperature Measurements

Figure 3-12 shows the measured gas temperature distribution along the centerline (z=3-20 mm) (i.e., 8-25 mm from the end of the electrodes) in the post-discharge jet region for N_2, O_2 and compressed air discharges. Note gas temperatures were measured using the thermocouples, not by the OES technique as mentioned in Chapter 2. It is because the corresponding emission intensities in the post-discharge region were too weak for measuring the rotational gas temperatures. Also with addition of large quantity of oxygen, the related emission lines related to nitrogen diminished because of the high electron affinity of the oxygen. The results showed that the gas temperatures for all the

cases decreased rapidly in the downstream direction. For example, the temperature of the pure nitrogen case dropped from 71°C (z=3mm) to 27°C (z=20mm), which was essentially at room temperature. In addition, gas temperatures for the APPJ containing more nitrogen were higher than those containing more oxygen. This was attributed to the much higher power absorption of neutral nitrogen caused by the ohmic heating effect which positive nitrogen ions collide with neutral background gas molecules as compared to the oxygen case since the ion density is higher in the nitrogen case. In general, the low gas temperatures in the plasma jet region observed in this study were highly suitable for inactivating bacteria without the danger of damaging bio-medical devices, which are often made of polymer-like materials.

3.4 Concentration Measurements of Ozone

3.4.1 Measurements using Ozone Monitor

Figures 3-13 and 3-9 show the concentrations of O_3 and typical NO-γ UV emission (236.6 nm, photon energy: 5.2 eV), respectively, as a function of downstream distance and O_2/N_2 (%) in the plasma jet region. The resolution distance of the measurement of O_3 concentration distribution and NO-γ UV distribution was 2 mm. The distributions of O_3 showed a maximal value at the downstream location of z≈10 mm for various ratios of O_2/N_2. In addition, UV emission was very strong in the near jet region (z up to 10 mm), especially when O_2/N_2≈0.05%. It is well known that ozone can effectively absorb UV emissions in the range of 220-280 nm [Wameck 2008]. Thus, an appreciable amount of oxygen radicals [$O_3 + h\upsilon \rightarrow O(^3P) + O_2$] was generated in the near jet region (z < 10 mm). Note that the NO-γ UV emissions were probably caused by the collision of ground NO species produced in the discharge with the abundant and long-lived

metastable N_2 [$N_2(A^3\sum_u^+)$] in a nitrogen-based discharge [Iwasaki *et al.,* 2008]. Higher

intensity NO-γ UV emissions did not indicate a higher amount of ground NO species

since it was also proportional to the amount of metastable N_2, which was strongly

dependent on the amount of oxygen addition and downstream location in the plasma jet.

Another possible mechanism for improving the hydrophilic property caused by the

existence of metastable N_2 [$N_2(A^3\sum_u^+)$] has been described in Chapter 4.

3.4.2 Infrared Absorption Spectra of the Post-Discharge Region

Figure 3-14 shows the infrared absorption spectra of the post-discharge regions for

N_2, O_2 and compressed air discharges in the 800-3600 cm^{-1} range as measured by an

in-situ FTIR technique. The strong absorption peak of 1055 cm^{-1} for ozone was clearly

observed in compressed air and O_2 discharges because of the abundant oxygen species

in the discharges. Note ozone was generated in the discharges, and carried downstream

since it is relatively long lived. Table 3-1 shows the absorption peak value of 1055 cm^{-1}

for ozone in the post-discharge regions for N_2, compressed air and O_2 discharges in the

range of z=4-20 mm. The results showed that very high levels of ozone were produced

in the post-discharge regions of compressed air and oxygen cases. Observed abundant

ozone played a key role in the inactivation of the bacteria as described in Chapter 6.

3.5 Summary of Chapter 3

Characterizations of the proposed planar DBD APPJ system are summarized as

follows:

(1) Direct visualization and OES spectra aided to our understanding the changes in

plume color.

(2) OES measurements showed that abundant metastble nitrogen was generated in the post-discharge jet region, which was important in later applications. However, addition of oxygen species reduced the amount of metastable nitrogen tremendously because of reduced plasma density due to electro-negativity of the oxygen.

(3) Gas temperature measurements showed that gas temperatures were low enough in the post-discharge jet region for most of the applications studied in the thesis.

(4) Measurements showed that addition of oxygen enhanced the amount of ozone, which were important in bacteria inactivation.

Chapter 4

Hydrophilic Modification of the PP Film Using Nitrogen-Based DBD APPJ

In this chapter, hydrophilic modification of the PP film using the developed planar nitrogen-based DBD APP system has been described in detail. Details of the experimental setup and characteristics of the discharge have been shown in Chapter 2 and Chapter 3, respectively, and are skipped here for brevity. Several diagnostic techniques, including contact angle measurements, aging effect, AFM analysis and XS analysis, were employed to study the effect of plasma jet treatment on the hydrophilic property and their corresponding results are described in the following in turn. Some important findings have been summarized at the end of this Chapter.

4.1 Contact Angle Measurements

4.1.1 Stationary Conditions

Figure 4-1 shows the distribution of the measured contact angles of the PP film as functions of the downstream distance (z=2-20 mm) and the ratio of O_2/N_2 (%) (0.004%-1.6%) immediately after the plasma treatment. Note that the measurement of the contact angle of the untreated sample was 103°. The results were obtained by averaging 3-5 measurements over a region of 10 mm by 10 mm of PP film with ±3°. The results indicated that the favorable operating conditions (contact angles < 30°) included: 1) z=6-9 mm and O_2/N_2 <0.008%; 2) z=2-10 mm and 0.04%<O_2/N_2 <0.3%; and 3) z=0-6 mm and 0.6%<O_2/N_2 <1.0%. The above observations could be explained by the

distributions of ozone and UV emission in the near jet region. It was interesting to learn that the lowest contact angle (23°) occurred at the ratio of O_2/N_2 near 0.06% at z=2 mm in Region 2, which was very close to the exit of the DBD. This could be attributed to the strong UV emission (200-300 nm) near this condition (see Figure 3-9), where the ozone could efficiently absorb and convert into an oxygen radical [Iwasaki *et al.,* 2007], and then easily react with the surface, as will be demonstrated later. In addition, UV emissions in the range of 200-300 nm also played an important role in breaking the chemical bonds of C-H (4.2 eV) and C-C (3.8 eV) since, for example, the photon energy of 236.6 nm was 5.74 eV. In Region 1, the ozone concentration had a maximal value at z=6-9 mm (as shown in Figure 3-14) due to the entrainment of oxygen from the ambient, where the UV emission was still appreciable in order for the ozone to convert efficiently into an oxygen radical. In Region 2, both ozone concentration and UV emission were appreciable, which led to the production of a significant amount of oxygen radicals. In addition, as mentioned earlier, strong UV emission also played an important role when the PP film was non-stationary, as will be discussed next. In Region 3, the ozone concentration was very high (40-80 ppm) (see Figure 3-14), although UV emission became relatively low in the downstream region after z=10 mm (see Figure 3-9).

4.1.2 Non-Stationary Conditions

The measured contact angles for the non-stationary films have been summarized in Tables 4-1 and 3-3 at z=2 mm. Table 4-1 lists the contact angles for various O_2/N_2 ratios (0-1.6%) at a non-stationary speed of v=0.5 cm/s, while Table 4-2 summarizes the data at various non-stationary speeds for PP film (0.5-8 cm/s) for four typical O_2/N_2 ratios in which the contact angles were in the range of 26-39°, as shown in Table 4-1. Only the cases of z=2 mm for the non-stationary films have been presented here, since we found

that the contact angles became very large after this distance (e.g. >70° at z=4 mm with O_2/N_2 ratio of 0.06%) because of a low residence time and very low UV emission at further downstream locations. At the distance of z=2 mm, we found that the minimal contact angle occurred at O_2/N_2 ratios in the range of 0.06-0.2%. However, as the non-stationary speed increased to v=1.0 cm/s, only at the condition of an O_2/N_2 ratio of 0.06% was the contact angle low enough (33°), while all other contact angles were greater than 45°. This was attributed to the very strong UV emission that occurred when the ratio of O_2/N_2 was between 0.02% and 0.2% near the jet exit (as shown in Figure 3-9). This led to a direct breaking of the surface chemical bonds, such as C-H (4.2 eV) and C-C (3.8 eV), without the help of oxygen radicals. Unlike the stationary film, the residence time on the surface for the conversion of ozone into an oxygen radical (very short life-time) by absorbing UV emissions (200-300 nm) became increasingly insufficient with the increasing non-stationary speed of the PP film. Thus, only the direct bond breaking by the UV emissions played an important role in the surface modification of non-stationary PP film. In general, the contact angle increased with the increasing non-stationary speed of the PP film. As the speed reached v=8 cm/s, surface modification of the PP film using a nitrogen-based DBD jet became effectively useless under the current operating conditions.

4.2 Aging Effect

Figure 4-2 presents the typical aging test within 24 h (at room temperature) of the improved hydrophilic property (contact angle) of stationary and non-stationary PP films after plasma treatment. The results showed that for all the cases as presented in Figure 4-2, the contact angles were all less than 30° right after plasma treatment. However, the contact angles for the non-stationary PP films rose very quickly to ~80° (v=0.5 cm/s)

and ~90° (v=1.0 cm/s) after 2 h of exposure to air and became saturated until the end of the test (24 h), while the contact angles for the stationary PP films increased 5-15° after the first 2-4 h and then became saturated at ~40-50° until the end of the test. This showed that the improved hydrophilic property, formed because of the bond breaking by the UV emission (non-stationary PP film), deteriorated quickly; however, the one caused by both the UV emission and oxygen radical (stationary PP film) could be sustained much longer. This will be further explained by the XPS analysis.

4.3 AFM Analysis

Table 4-3 summarizes the typical roughness data of stationary PP film, as measured by AFM, after treatment using the pure nitrogen discharge jet. Note that the RMS roughness data were taken from a 3 μm by 3 μm section. The untreated RMS roughness was 40.4 nm, but it decreased to 17.8 nm at z=6 mm and gradually increased at further downstream locations (28.6 nm at z=20 mm). This trend coincided with that of the measured contact angles, in which a minimal value occurred in the range of z=6-8 mm. This meant that the less the level of roughness, the smaller the contact angle. The DBD treatments thus produced various effects, such as the removal of contaminants, oligomers and amorphous layers existing on the surface, allowing for chemical activation of the material [Borcia *et al.*, 2006]; however, this will require further investigation in order to understand the underlying physics.

4.4 XPS Analysis

Figure 4-3 shows the XPS scan spectra of untreated and treated stationary PP (N_2+0.06% O_2) films. After plasma treatment, the O1s peak increased dramatically, while the C1s peak decreased in a milder fashion. This meant that an appreciable

amount of oxygen radical had been incorporated into the surface compound, while carbon had been removed efficiently.

4.5 Discussion

Table 4-4 summarizes the corresponding quantitative atomic compositions and the fractions of peak area of untreated and treated samples, as calculated from the C1s core level spectra on the surface of the PP film for the various typical test conditions. The results showed that after plasma treatment, tremendous increases in the O/C ratio at z=2 and 6 mm were found. In the stationary cases, at z=2 and 6 mm, we found a large increase in the O/C ratio. A possible explanation could be that at z=2 mm, the ozone absorbed the abundant NO-γ UV emission (200-300 nm) and produced abundant highly chemically active oxygen radicals by photo dissociation $[O_3 + h\upsilon \rightarrow O(^3P) + O_2]$ which further reacted with the PP film. The N_2 1st positive lines $[N_2(B^3\prod_g) \rightarrow N_2(A^3\sum_u^+)]$ (500-700 nm in Figure 3-8a) show that abundant metastable $N_2(A^3\sum_u^+)$ (energy=6.2 eV) was generated, which could be transported to the substrate by the jet stream and easily break the C-C (3.8 eV) chemical bonds, as has been observed previously [Herron 1999; Klages *et al.,* 2008]. At downstream z=6 mm, the UV emission became weaker but the ozone became more abundant because of ambient entrainment, and it could still produce appreciable amounts of oxygen radicals. In addition, the amount of long-lived metastable $N_2(A^3\sum_u^+)$ was still high enough to reach the PP film and break its chemical bonds. The above two mechanisms resulted in a tremendous O/C increase at both z=2 and 6 mm. However, at the further downstream position z=20 mm, no UV emission was possible and the amount of metastable $N_2(A^3\sum_u^+)$ became smaller, making the O/C ratio increase less obvious, as shown in Table 4-4.

For example, the O/C ratio increased from 0.1 to 0.9 for stationary PP film at z=6 mm for the condition of $N_2+0.06\%$ O_2, in which the measured contact angle was 23°. This again confirmed that the polar functional groups containing oxygen were introduced on the PP film surface. By comparing the corresponding measurements of the contact angles in Table 4-4, we concluded that the larger the O/C ratio, the smaller the contact angle. Figure 4-4 presents a graph by separating the peak of the samples in the C1s level through curve fitting. As shown in Figure 4-4, the polar functional groups, such as C-O (286.8 eV), C=O (287.8 eV) and COO (289.7 eV), were introduced on the PP film surface after an AP nitrogen plasma treatment, although the fraction of COO was very small and less than the experimental uncertainties. Nevertheless, these could be only considered qualitative since they were fitted values.

The results showed that the greater the amount of functional groups C-O and C=O, the better the hydrophilic property of the PP film. In addition, the appearance of the C=O group may have explained the longer measured aging time for stationary film cases as found earlier (see Figure 4-2), given the higher binding energy as compared to that of C-O. As trace oxygen was added into the nitrogen ($O_2/N_2=0.06\%$), more ozone was generated (see Figure 3-14) and more UV (200-300 nm) emitted (see Figure 3-9), which produced more abundant oxygen radicals to react with the PP film. This was confirmed by the increase of the O/C ratio (0.8-0.9) as compared to the pure nitrogen case (0.7) in Table 4-4, resulting in a better hydrophilic property at z=2 mm. At z=6 mm, much lower UV emission caused the role of this mechanism to be less important than the metastable nitrogen, as can be seen from almost the same contact angle (23° vs. 26°).

Based on this observation, methods to efficiently incorporate C=O and even COO functional groups, which have higher binding energies, are sure to become an important issue for longer aging time and should be subject to further investigation.
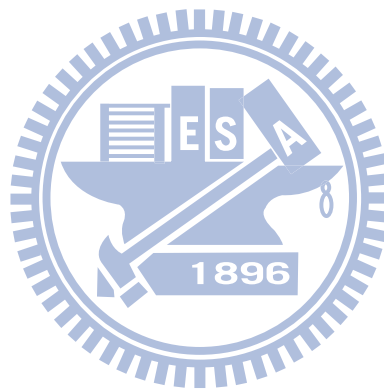
4.6 Summary of Chapter 4

Major findings of the study of hydrophilic modification of the PP film using the developed planar DBD APPJ system are summarized as follows:

(1) The DBD jet was applied to treat the PP film under stationary and non-stationary conditions with various O_2/N_2 ratios ranging from 0 to 1.6% at different treating distances in the range of 2-20 mm.

(2) Results show that, for stationary PP films, the surface hydrophilic property improves dramatically from 103° (untreated) to a value less than 30° (treated) for contact angles with a wide range of O_2/N_2 ratios (< 1%) and treating distances (< 10 mm). For the non-stationary PP films, highly hydrophilic surfaces can only be obtained when the PP film is placed near the jet exit (treating distance of 2-4 mm) with an O_2/N_2 ratio of 0.06-0.2%.

(3) These observations are explained through measured optical emission spectra and ozone concentration data, in which the metastable nitrogen plays a key role in breaking the surface chemical bounds and UV emission (200-300 nm) participates in the process of converting the ozone into oxygen radical. Aging tests show that for stationary PP films the contact angle can still be maintained at ~40° after 24 h, while for the non-stationary test cases it can only be maintained at ~80-90° when the non-stationary speed is near 1 cm/s.

(4) By AFM analysis, we also observed that the less the surface roughness the smaller the contact angle is. Finally, XPS analysis shows that O/C ratio increases dramatically which results from the incorporation of several polar functional groups containing oxygen into the surface of PP films during plasma treatment. The greater the amount of functional groups C-O and C=O, the better the

hydrophilic property of the PP film.

(5) In addition, the number of polar functional groups, such as C=O, having higher binding energy can directly influence the aging time of the hydrophilic property of PP film after the plasma treatment.

Chapter 5

Surface Cleaning of the ITO Glass Using Nitrogen-Based DBD APPJ

In this chapter, surface cleaning of ITO glass using the developed planar nitrogen-based DBD APP system has been described in detail. Details of the experimental setup have been shown in Chapter 2 and are skipped here for brevity. Several diagnostic techniques, including contact angle measurements, aging effect, XPS analysis and AFM analysis were employed to study the effect of plasma jet treatment on the hydrophilic property and their corresponding results are described in the following in turn. Some important findings have been summarized at the end of this Chapter.

5.1 Contact Angle Measurements

5.1.1 Stationary Conditions

Figure 5-1 shows the measured contact angle (CA) of the stationary ITO glass surface after the plasma jet treatment as a function of both the downstream distance and the ratio of O_2 to N_2 (%). The contact angle before plasma treatment was 84°. The results showed that there existed two distinct regimes with lower CAs in the range of 20-30°. The first one was the regime with an oxygen addition of less than 0.05% and a treating distance in the range of 6-16 mm. The second one was the regime with an oxygen addition larger than 0.06% and a treating distance in the range of 2-10 mm. Measured CAs in both regimes were less than 30° in general; for some conditions in the first regime they were well below 25°, demonstrating that this post-discharge jet region could be used to effectively improve the hydrophilic property of ITO glass by adding

trace amounts of oxygen.

5.1.2 Non-Stationary Conditions

Figures 5-2a and 5-2b show the measured contact angles (CA) of the ITO glass surface after pure N_2 and 0.04% O_2/N_2 plasma jet treatment for the non-stationary case (1-9 cm/s) as a function of downstream distance, respectively. The measured contact angle generally increased with increased non-stationary speed at the fixed downstream distance from the jet exit, which meant that the hydrophilic property deteriorated because of the reduced effective treatment time. However, the range of smaller contact angles for the 0.04% O_2/N_2 plasma jet treatment was obviously wider than that of the pure N_2 one; this showed that the addition of a trace amount of oxygen produced a wider operating window. These results are explained below.

5.2 XPS Analysis

Table 5-1 summarizes the measured chemical composition of the ITO glass surface using XPS analysis and the measured CAs after plasma jet treatment. Clearly, the O/C ratio increased dramatically from 1.16 (untreated) to 2.95-2.96 (z=10 mm for pure nitrogen and 0.06% oxygen cases), which was similar to the result in [Yi *et al.,* 2004]. This meant that some carbon atoms were effectively removed by the plasma jet, which could be explained by considering the measured concentrations of O_3, UV emission (e.g., 236.6 nm, NO-γ) and other OES spectra in the jet region, which are described next.

5.3 AFM Analysis

Table 5-2 summarizes the typical roughness data of stationary ITO glass under

various test conditions after surface treatment using the pure N_2 and O_2/N_2 (0.1%) discharge jet with different distances. Note that the RMS roughness data were taken from a $2 \, \mu m$ by $2 \, \mu m$ section. All RMS roughness was in the range of 0.53-0.69 nm, signifying that the application of APPJ did not significantly modify the surface morphology. APPJ only acted to remove the attached organic contaminants, which was important for this type of application.

5.4 Discussion

These data have shown that the amount of metastable nitrogen decreased rapidly with the addition of too much oxygen, since oxygen is an electronegative gas which has a very strong electron affinity. However, the quantitative reason for observing the maximal amount of the 1st positive N_2 at O_2/N_2=0.06% is still unknown and deserves further investigation. Note that the metastable N_2 [$N_2(A^3\sum_u^+)$] energy state is 6.2 eV above the ground state and its lifetime is ~13 s [Fridman *et al.,* 2004]. It is very reactive towards saturated hydrocarbons and can transfer about 6.2 eV efficiently to these molecules to generate dissociative triplet states that break C-H bonds (4.2 eV) and C-C bonds (3.8 eV) [Herron 1999; Klages *et al.,* 2008]. This effect may have been especially important in improving the hydrophilic property of ITO glass at the far downstream locations where the amount of O_2/N_2 was very small (e.g., 0.05-0.06%), and the amount of ozone was also very small (see Figure 5-1).

In the first regime (nearly pure nitrogen plasma jet), as indicated in Figure 5-1, at the exit of the DBD, the NO-γ UV emission was relatively appreciable (see Figure 6) since the metastable $N_2(A^3\sum_u^+)$ in the early portion of the plasma jet was still abundant, although the NO concentration would be low under this condition. Note that
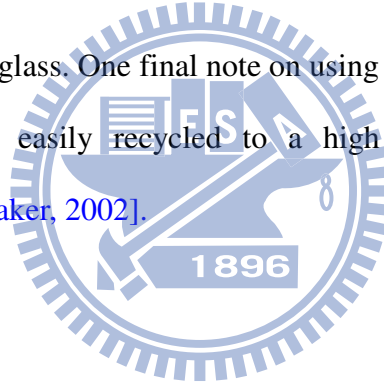
the residence time of the N$_2$ [$N_2(A^3\sum_u^+)$] species for the current test condition was 0.1 ms up to z=16 mm, which was much shorter than its lifetime (~13 sec). Although the amount of NO-γ UV emission decreased rapidly in the downstream direction (because of ambient quenching of the NO and the short-lived excited $N_2(B^3\prod_g)$), the amount of long-lived metastable $N_2(A^3\sum_u^+)$ was still high enough to transfer energy effectively to break the C-H and C-C bonds of the organic compounds on the ITO glass surface.

In the second regime, as indicated in Figure 5-1, at the exit of the DBD, the NO-γ UV emission peaked at ~0.05% of oxygen addition and then dropped rapidly due to the quenching of increased oxygen addition (reduced metastable N$_2$ species), as shown in Figure 3-9. In this peak region near the DBD exit, a high intensity of NO-γ UV emission produced better surface cleaning because of more atomic oxygen O produced following the reaction path ($O_3 + h\upsilon \rightarrow O(^3P) + O_2$), and the abundant metastable N$_2$ [$N_2(A^3\sum_u^+)$] transferred energy to break bonds such as C-C (3.8 eV) and C-H (4.2 eV). As more oxygen was added (e.g., 1%), the amount of atomic oxygen decreased accordingly (see Figure 3-9) because the NO-γ UV emission was much lower than in the first regime. However, in the further downstream location after z=10 mm, the NO-γ UV emission was reduced to a very small amount, as atomic oxygen O could not be produced effectively; the long-lived N$_2$ [$N_2(A^3\sum_u^+)$] then played a key role in surface cleaning, although the CA increased rapidly after this point.

5.5 Summary of Chapter 5

Major findings of the study of surface cleaning of ITO glass using the developed planar DBD APPJ system are summarized as follows:

(1) Results showed that there existed two distinct regimes having lower CAs in the range of 20-30°. Possible mechanisms of surface cleaning have been presented; they took into account the spatial distribution of O_3, NO-γ UV emission and OES spectra.

(2) For ITO cleaning mechanisms, in the near jet downstream location (z<10 mm), both the metastable N_2 [$N_2(A^3\sum_u^+)$] and ozone photo-induced dissociation played dominant roles in cleaning ITO glass, although their relative importance was unclear and requires further investigation.

(3) In the far jet downstream location (z>10mm), when the ratio of O_2/N_2 was small, only the long-lived metastable N_2 [$N_2(A^3\sum_u^+)$] played a major role in cleaning ITO glass. One final note on using nitrogen as the discharge gas is that nitrogen was easily recycled to a high purity (>99%) using a ceramic membrane [Baker, 2002].

Chapter 6

Inactivation of the *E. coli* and the *B. subtilis* Using Air-Based DBD APPJ

In this chapter, inactivation of the *E. coli* and *B. subtilis* using the developed planar air-based DBD APP system has been described in detail. Details of the experimental setup and the characteristics of the discharge have been shown in Chapter 2 and Chapter 3, respectively, are skipped here for brevity. Direct visualization of the Petri dish with bacteria inside and SEM images before and after plasma jet treatment are described in the following in turn. Some important findings have been summarized at the end of this Chapter.
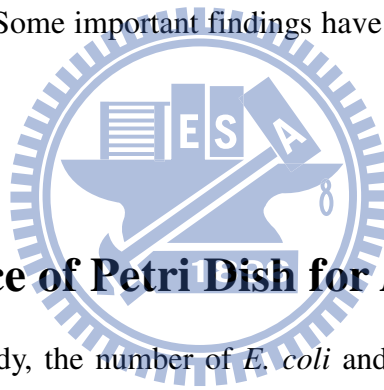
6.1 Appearance of Petri Dish for *E. coli* and *B. subtilis*

In the current study, the number of *E. coli* and *B. subtilis* on each petri dish was controlled as $\sim 10^7$ CFU/mL, respectively, before plasma jet treatment. Figures 6-1 and 6-2 show the appearance of the petri dish for *E. coli* and *B. subtilis*, respectively, after incubation with different designated exposure distances and times (i.e., numbers of passes) by the compressed-air plasma jet. As shown in Figure 3-14, the oxygen APPJ generated a higher concentration of ozone than the air APPJ; however, the other reactive nitrogen species (e.g., NO_2) existing in air plasma may have also assisted in the inactivation of the bacteria [Laroussi *et al.,* 2004]. Further investigation is required to clarify the roles of these reactive nitrogen species. It was found that the compressed-air APPJ treatment resulted in very efficient inactivation of both the *E. coli* and *B. subtilis* bacteria after 10 (residence time: 1.0 s) and 18 passes (residence time: 1.8 s) of

exposure, respectively, for all treatment distances (4-20 mm).

Tables 6-1 and 6-2 summarize the survival rates (%) of *E. coli* and *B. subtilis*, respectively, under various test conditions (exposure distance and number of passes). The results clearly showed that discharges containing oxygen performed excellently in activating both types of bacteria because of the existence of oxygen radicals that were very chemically active in reacting with the bacteria. The generation of the oxygen radicals will be explained later.

For *E. coli*, all discharges totally inactivated the bacteria within 10 passes of exposure for the highest CFUs (=10^7 CFU/mL), except for the nitrogen discharge. Using the nitrogen discharge, even after 18 passes of exposure, the inactivation was essentially in vain for the case of 10^7 CFU/mL. The nitrogen discharge possessed a much higher germicidal UV emission of NO (180-280 nm) than the oxygen or compressed-air discharges, as shown in Figure 3-10 earlier. However, the OES measurements have shown that the germicidal UV emission was essentially negligible in the jet region because of quenching from the entrained air and because it is very short-lived. This made the inactivation of the *E. coli* very inefficient, as summarized in Table 6-1. For *B. subtilis*, the results were similar, but it generally required a longer period (up to 18 passes) of exposure to inactivate the bacteria for the case of 10^7 CFU/mL.

6.2 SEM images of Untreated and Treated *E. coli* and *B. subtilis*

The SEM images of the untreated and treated *E. coli* and *B. subtilis* using a compressed air plasma jet are shown in Figures 6-3 and 6-4, respectively. The *E. coli* underwent a slight morphological change as compared to the control, while the *B. subtilis* bacteria remained nearly intact; however, the bacteria were actually inactivated

based on our experimental observation (Tables 6-1 and 6-2). This was different from the sterilization studies showing clear ruptured bacterium surfaces after plasma treatment, which could have been caused by the different plasma doses in the present study and these other studies. This definitely deserves further investigation (e.g., using bio-TEM) to clarify the underlying cause for the efficient inactivation as found in the current study.

6.3 Discussion

Plasma-generated ozone is at least partially dissociated when immersed into water, liquid-based, or liquid-like biomaterial (bacteria smeared on agar) [Fridman 2008]. Atomic oxygen generated in the process intensively reacts with bioorganic molecules, producing radicals and OH radicals. Thus, ozone can play an important role in assisting intensive OH-based biochemical oxidation. It was thought that *B. subtilis* had a thicker peptidoglycan structure (about 20~80 nm) than *E. coli* (about 7~8 nm) [Sun *et al.,* 2007], which may have been the main reason a longer exposure time was needed to inactivate the *B. subtilis* bacteria. Note that the peptidoglycan exists in periplasmic space between the cytoplasmic membrane and the outer membrane. A broken peptidoglycan would affect the proper function of the solute transportation function for carrying protein in the cytoplasmic membrane, which would result in effective bacterium inactivation. Some mechanisms of the inactivation effect on microorganisms by low-temperature plasma have been postulated previously [Gaunt *et al.,* 2006]. Nevertheless, the current results have shown that it was as effective as the previous studies using discharge region, by using post-discharge jet region [Sun *et al.,* 2007; Lee *et al.,* 2006], which was very encouraging from the perspective of application convenience. In addition, considering the cost of operation, the compressed air discharge may represent the best choice.

6.4 Summary of Chapter 6

Major findings of the study of inactivation of *E. coli* and *B. subtilis* using the developed planar air-based DBD APPJ system are summarized as follows:

(1) The APPJ was used to inactivate *E. coli* (Gram negative) and *B. subtilis* (Gram positive) up to 10^7 CFU/mL using the post-discharge region. Results show that the post-discharge jet region is very efficient in inactivating these two bacteria as previous studies using the discharge region, should the working gas contains appreciable oxygen addition, which in turn generates abundant ozone.

(2) In addition, the inactivation is more effective by compressed-air APPJ compared to that by oxygen APPJ, possibly through the assistance of nitrous oxide existing in the former. Major advantage by using post-discharge jet region is its flexibility in practical applications, in which the DBD becomes a stand-alone module that can be used to treat essentially any sample as compared to the conventional applications by using the discharge region.

Chapter 7

Sterilization of the *B. subtilis* Spore Using Air/Carbon Fluorine DBD APPJ

In this chapter, sterilization of the *B. subtilis* spore using the developed planar air-carbon fluorine DBD APPJ system has been described in detail. Details of the experimental setup and characteristics of the discharge have been shown in Chapter 2 and Chapter 3, respectively, and are skipped here for brevity. XPS analysis of PP film treated by the air-carbon fluorine DBD APPJ, direct visualization of the Petri dish with bacteria inside and SEM images before and after plasma jet treatment are described in the following in turn. Some important findings have been summarized at the end of this Chapter.

7.1 XPS Analysis of PP Film

Since it is difficult to directly probe the existence of the F related atoms or compounds in the discharge and post-discharge jet regions using OES data, we have instead verified the existence of chemically active F radicals indirectly. We have applied the air-carbon fluorine DBD APPJ to treat a PP film and examined the surface composition using XPS analysis. Table 7-1 summarizes the measured chemical composition of the PP film surface using XPS analysis and the measured CAs after plasma jet treatment. Clearly, the O/C ratio increased dramatically from 0.30 (untreated) to 0.40 (z=14 mm for 2% CF_4/air oxygen cases), which was similar to the result in [Kim *et al.,* 2006]. We have to admit that the measured trace amount F atoms in the PP film surface is obviously smaller than the experimental uncertainties of measurement..

However, the results clearly showed that some carbon atoms were effectively removed by the plasma jet, which could be only caused by the F related species since the O/C ratio obtained by the use of pure air discharge is smaller (0.35) than 0.40. Of course, further study is required to unveil the role of F related radicals and compounds in the sterilization of bacteria.

7.2 Appearance of Petri Dish for *B. subtilis* Spore

In the current study, the number of *B. subtilis* spores on each petri dish was controlled at $\sim10^5$, 10^6 and 10^7 spore/mL before plasma jet treatment. Figures 7-1 and 7-2 show the appearance of the *B. subtilis* spore after incubation with different designated bacterial numbers (i.e., spore/mL) and times (i.e., numbers of passes) by the air plasma and CF_4/air (2%) plasma jets, respectively. It was found that the CF_4/air (2%) APPJ treatment resulted in the efficient inactivation of the *B. subtilis* spores after 10 passes (residence time: 1.0 s) exposures for treatment distances (14 mm).

Tables 7-2 and 7-3 summarize the survival rates (%) of the *B. subtilis* spores under various test conditions (number of bacteria and number of passes) air and CF_4/air (2%), respectively. The results clearly showed that the discharges containing Carbon Fluorine (CF_4) performed excellently in activating the *B. subtilis* spores because of the existence of F atoms that are very chemically active in etching with the spores [Lerouge *et al.*, 1999].

7.3 SEM Images of Untreated and Treated *B. subtilis* Spore

The SEM images of untreated and treated *B. subtilis* spore using a CF_4/air (2%) plasma jet are shown in Figure 7-3. The *B. subtilis* spore underwent some

morphological erosion as compared to the control dish. The bacteria were actually sterilized based on our experimental observation (see Tables 7-2 and 7-3). This was similar to polymer material etching studies which showed clear ruptured bacterium surfaces after plasma treatment. This definitely deserves future investigation (e.g., using bio-TEM) to clarify the underlying cause for the efficient sterilization as found in the current study.

7.4 Summary of Chapter 7

Major findings of the study of sterilization of *B. subtilis* spore using the developed planar air-carbon fluorine DBD APPJ system are summarized as follows:

(1) In the PP film treated by CF4/air (2%) DBD plasma, the O/C ratio of the XPS data showed an increase as compared with treated by air DBD. This showed that chemically active F related radicals existed in the discharge.

(2) The sterilization of the *B. subtilis* spore treated by CF_4/air (2%) DBD plasma was very inefficient as compared with that treated by air DBD plasma.

Indeed, the role of CF_4 mixed in the air DBD discharge for sterilization of the *B. subtilis* spore requires further investigation.

Chapter 8

Conclusion and Recommendations for Future Study

In this chapter, major findings of the current thesis are summarized in the following in turn as: 1) Characterization of the planar DBD APPJ; 2) Hydrophilic modification of the PP film; 3) Surface cleaning of the ITO glass; 4) Inactivation of *E. coli* and *B. subtilis* and 5) Sterilization of *B. subtilis* spore. In addition, recommendations for future study are also outlined at the end of this chapter.

8.1 Summaries of the Thesis

8.1.1 Characterization of the Planar DBD APPJ

Characterizations of the proposed planar DBD APPJ system are summarized as follows:

(1) Direct visualization and OES spectra aided to our understanding the changes in plume color.

(2) OES measurements showed that abundant metastble nitrogen was generated in the post-discharge jet region, which was important in later applications. However, addition of oxygen species reduced the amount of metastable nitrogen tremendously because of reduced plasma density due to electro-negativity of the oxygen.

(3) Gas temperature measurements showed that gas temperatures were low enough in the post-discharge jet region for most of the applications studied in the thesis.

(4) Measurements showed that addition of oxygen enhanced the amount of ozone, which were important in bacteria inactivation.

8.1.2 Hydrophilic Modification of the PP Film

Major findings of the study of hydrophilic modification of the PP film using the developed planar DBD APPJ system are summarized as follows:

(1) The DBD jet was applied to treat the PP film under stationary and non-stationary conditions with various O_2/N_2 ratios ranging from 0 to 1.6% at different treating distances in the range of 2-20 mm.

(2) Results show that, for stationary PP films, the surface hydrophilic property improves dramatically from 103° (untreated) to a value less than 30° (treated) for contact angles with a wide range of O_2/N_2 ratios (< 1%) and treating distances (< 10 mm). For the non-stationary PP films, highly hydrophilic surfaces can only be obtained when the PP film is placed near the jet exit (treating distance of 2-4 mm) with an O_2/N_2 ratio of 0.06-0.2%.

(3) These observations are explained through measured optical emission spectra and ozone concentration data, in which the metastable nitrogen plays a key role in breaking the surface chemical bounds and UV emission (200-300 nm) participates in the process of converting the ozone into oxygen radical. Aging tests show that for stationary PP films the contact angle can still be maintained at ~40° after 24 h, while for the non-stationary test cases it can only be maintained at ~80-90° when the non-stationary speed is near 1 cm/s.

(4) By AFM analysis, we also observed that the less the surface roughness the smaller the contact angle is. Finally, XPS analysis shows that O/C ratio increases dramatically which results from the incorporation of several polar

functional groups containing oxygen into the surface of PP films during plasma treatment. The greater the amount of functional groups C-O and C=O, the better the hydrophilic property of the PP film.

(5) In addition, the number of polar functional groups, such as C=O, having higher binding energy can directly influence the aging time of the hydrophilic property of PP film after the plasma treatment.

8.1.3 Surface Cleaning of the ITO Glass

Major findings of the study of surface cleaning of ITO glass using the developed planar DBD APPJ system are summarized as follows:

(1) Results showed that there existed two distinct regimes having lower CAs in the range of 20-30°. Possible mechanisms of surface cleaning have been presented; they took into account the spatial distribution of O_3, NO-γ UV emission and OES spectra.

(2) For ITO cleaning mechanisms, in the near jet downstream location (z<10 mm), both the metastable N_2 [$N_2(A^3\sum_u^+)$] and ozone photo-induced dissociation played dominant roles in cleaning ITO glass, although their relative importance was unclear and requires further investigation.

(3) In the far jet downstream location (z>10mm), when the ratio of O_2/N_2 was small, only the long-lived metastable N_2 [$N_2(A^3\sum_u^+)$] played a major role in cleaning ITO glass. One final note on using nitrogen as the discharge gas is that nitrogen was easily recycled to a high purity (>99%) using a ceramic membrane [Baker, 2002]

8.1.4 Inactivation of *E. coli* and *B. subtilis*

Major findings of the study of inactivation of *E. coli* and *B. subtilis* using the developed planar air-based DBD APPJ system are summarized as follows:

(1) The APPJ was used to inactivate *E. coli* (Gram negative) and *B. subtilis* (Gram positive) up to 10^7 CFU/mL using the post-discharge region. Results show that the post-discharge jet region is very efficient in inactivating these two bacteria as previous studies using the discharge region, should the working gas contains appreciable oxygen addition, which in turn generates abundant ozone.

(2) In addition, the inactivation is more effective by compressed-air APPJ compared to that by oxygen APPJ, possibly through the assistance of nitrous oxide existing in the former. Major advantage by using post-discharge jet region is its flexibility in practical applications, in which the DBD becomes a stand-alone module that can be used to treat essentially any sample as compared to the conventional applications by using the discharge region.

8.1.5 Sterilization of *B. subtilis* Spore

Major findings of the study of sterilization of *B. subtilis* spore using the developed planar air-carbon fluorine DBD APPJ system are summarized as follows:

(1) In the PP film treated by CF4/air (2%) DBD plasma, the O/C ratio of the XPS data showed an increase as compared with treated by air DBD plasma. This showed that chemically active F related radicals existed in the discharge.

(2) The sterilization of the *B. subtilis* spore treated by CF_4/air (2%) DBD plasma was very efficient as compared with that treated by air DBD plasma.

(3) Indeed, the role of CF_4 mixed in the air DBD discharge for sterilization of the *B. subtilis* spore requires further investigation.

8.2 Recommendations for Future Work

(1) The fluid modeling coupled with a neutral flow solver using detailed plasma chemistry should be conducted to help elucidate the observed physical phenomena, which are otherwise very difficult to understand only based on measurements.

(2) Further tailor of the properties of nitrogen- and air-based discharges using a realistic pulse-based power source with the help of fluid modeling should be conducted to enhance the applicability of the proposed discharges.

(3) For CF_4/Air DBD APPJ OES measurement, try to enlarge the relative CFx/F line peak intensity of OES spectrum compare with background (without plasma) CF_4/Air. To presume plasma chemistry of the possible existence of CFx/F line peak in discharge region of CF_4/Air DBD APPJ.

(4) For CF_4/Air DBD APPJ post-discharge region, try to use FTIR measuring reactive F species (as CFx fragment and CF_2O) IR spectrum. To presume plasma chemistry of the possible existence of relative F species in post-discharge region of CF_4/Air DBD APPJ.

(5) Using ATR-FTIR analysis the bacteria (*E. coli* and *B. subtilis*)/*B. subtilis* spore of surface chemical composition after DBD plasma untreated/treated to explain the cell wall variation of C1s/O1s chemical bonding energy.

(6) For *B. subtilis* spore sterilization mechanism presuming of CF_4/Air DBD APPJ, to study relative references about low pressure CF_4/O_2 plasma remove photo-resistance mechanism. And try to search the optimum concentration of CF_4/Air for *B. subtilis* spore sterilization.

(7) To use air DBD APPJ treated the similar cell membrane material (liposome bilayers) and compare the SEM of liposome bilayers and *E. coli*. It can help to

understand plasma chemistry of E. coli outer cell wall.

(8) For PP film treated by nitrogen-based DBD APPJ, the XPS data of chemical composition C and O atom concentration are different with C1s peak curve fitting C-O, C-C, C=O, COO concentration. To discuss with equipment technician about the calculating rules and verify again.

(9) For PP film non-stationary treated by nitrogen-based DBD APPJ case, try to normalize the equation of non-stationary speeds and treatment distances in fixed O_2/N_2 ratio. It can help to presume PP film contact angle variation in application.

(10) More studies are required to clarify qualitatively and quantitatively what kinds of reactive species for the sterilization of *B. subtilis* spore using the CF_4/air DBD APPJ.

(11) We can possibly apply an enlarged enclosure to cover the post-discharge jet region to form a region of abundant metastable region for some specific applications.

(12) As demonstrated in the present thesis, we have shown that the nitrogen- and air-based DBD APPJ system is very effective with a reduced cost in improving hydrophilic properties and sterilization/inactivation of a polymer surface. It is thus highly promising to apply this APPJ system to improve the cell attachment or bio-compatibility of some bio-materials, for example, PLA $((C_6H_8O_4)_n)$ as the skeleton of artificial vascular graft and PDMS $((C_2H_6OSi)_n)$ as the microfluidic channels, in a totally dry approach, unlike the conventional chitosan coating $((C_6H_{11}NO_4)_n)$, which is notoriously time-consuming and very tedious.

References

[1] Akishev, Y., Grushin, M., Dyatko, N., Kochetov, I., Napartovich, A., Trushkin, N., Duc, T. M. and Descours S., 2008, "Studies on Cold Plasma-Polymer Surface Interaction by Example of PP- and PET-Films," *J. Phys. D: Appl. Phys.*, Vol. 41, Issue 23, 235203.Baker, R. W., 2002, "Future Directions of Membrane Gas Separation Technology," *Ind. Eng. Chem. Res.*, Vol. 41, pp. 1393-1411.

[2] Bibinov, N. K., Fateev, A. A. and Wiesemann, K., 2001, "On the Influence of Metastable Reactions on Rotational Temperature in Dielectric Barrier Discharges in He-N_2 mixture," *J. Phys. D: Appl. Phys.*, Vol. 34, Issue 12, pp. 1819-1826.

[3] Borcia, G., Chiper, A. and Rusu, I., 2006, "Using a He+N_2 Dielectric Barrier Discharge for the Modification of Polymer Surface Properties," *Plasma Sources Sci. Technol.*, Vol. 15, Issue 4, pp. 849-857.

[4] Brandenburg, R., Maiorov, V. A., Golubovskii, Y. B., Wagner, H. E., Behnke, J. and Behnke, J. F., 2005, "Diffuse Barrier Discharges in Nitrogen with Small Admixtures of Oxygen: Discharge Mechanism and Transition to the Filamentary Regime," *J. Phys. D: Appl. Phys.*, Vol. 38, Issue 13, pp. 2187-2197.

[5] Chaudhary, K., Inomata, K., Yoshimoto, M. and Koinuma, H., 2003, "Open-Air Silicon Etching by H_2-He-CH_4 Flowing Cold Plasma," *Mater. Lett.*, Vol. 57, Issue 22-23, pp. 3406-3411.

[6] Cheng, K. W., Hung, C. T., Chiang, M. H., Hwang, F. N. and Wu, J. S., 2010, "One-Dimensional Simulation of Nitrogen Dielectric Barrier Discharge Driven by a Quasi-Pulsed Power Source and Its Comparison with Experiments," *Comput. Phys. Comm.*, has been accepted.

[7] Choi, Y. H., Kim, J. H. and Hwang, Y. S., 2006, "One-Dimensional Discharge Simulation of Nitrogen DBD Atmospheric Pressure Plasma," *Thin Solid Films*, Vol. 506, pp. 389-395.

[8] Deng, X. T., Shi, J. J. and Kong, M. G., 2006, "Physical Mechanisms of Inactivation of *Bacillus subtilis* Spores Using Cold Atmospheric Plasmas," *IEEE Trans. Plasma. Sci.*, Vol. 34, Issue 4, pp. 1310-1316.

[9] Dilecce, G., Ambrico, P. F. and Benedictis, S. D., 2007, "$N_2(A(3)Sigma(+)(u))$ Density Measurement in a Dielectric Barrier Discharge in N_2 and N_2 with Small O_2 admixtures," *Plasma Sources Sci. Technol.*, Vol. 16, Issue 3, pp. 511-522.

[10] Fanelli, F., 2009, "Optical Emission Spectroscopy of Ar-Fluorocarbon-Oxygen Fed Atmospheric Pressure Dielectric Barrier Discharge," *Plasma Process. Polym.*, Vol. 6, pp. 547-554.

[11] Fantz, U., 2006, "Basic of Plasma Spectroscopy," *Plasma Sources Sci. Technol.*, Vol. 15, Issue 4, pp. S137-S147.

[12] Fridman, A. and Kennedy, L. A., 2004, Plasma Physics and Engineering, *Taylor and Francis*, New York.

[13] Fridman, A., 2008, Plasma Chemistry, 1st ed., *Cambridge*, New York, pp. 848-859.

[14] Golubovskii, Y. B., Maiorov, V. A., Behnke, J. and Behnke, J. F., 2002, "Influence of Interaction Between Charged Particles and Dielectric Surface Over a Homogeneous Barrier Discharge in Nitrogen" *J. Phys. D: Appl. Phys.*, Vol. 35, Issue, pp. 751-761.

[15] Golubovskii, Y. B., Maiorov, V. A. Behnke, J. F., Tepper, J. and Lindmayer, M., 2004, "Study of the Homogeneous Glow-Like Discharge in Nitrogen at Atmospheric Pressure," *J. Phys. D: Appl. Phys.*, Vol. 37, Issue 9, pp. 1346-1356.

[16] Gaunt, L. F., Beggs, C. B. and Georghiou, G. E., 2006, "Bacterial Action of the Reactive Species Produced by Gas-Discharge Nonthermal Plasma at Atmospheric Pressure: A Review," *IEEE Trans. Plasma Sci.*, Vol. 34, Issue 4, pp. 1257-1269.

[17] Guerra, V., Sá, P. A. and Loureiro, J., 2001, "Role Played by the $N_2(A(3)Sigma(+)(u))$ Metastable in Stationary N_2 and N_2-O_2 Discharge," *J. Phys. D: Appl. Phys.*, Vol. 34, Issue 12, pp. 1745-1755.

[18] Herrmann, H. W., Henins, I., Park, J. and Selwyn, G. S., 1999, "Decontamination of Chemical and Biological Warfare, (CBW) Agents Using an Atmospheric Pressure Plasma Jet (APPJ)," Phys. Plasmas, Vol. 6, Issue 5, pp. 2284-2289.

[19] Herron, J. T., 1999, "Evaluated Chemical Kinetics Data for Reactions of $N(D^2)$, $N(P^2)$, and $N_2(A(3)Sigma(+)(u))$ in the Gas Phase," *J. Phys. Chem. Ref. Data*, Vol. 28, Issue 5, pp. 1453-1483.

[20] Hippler, R., Kersten, H., Schmidt, M. and Schoenbach, K. H., 2008, Low temperature plasmas: fundamentals, 2nd ed., *Wiley*, New York, pp. 821-835.

[21] Holyoak, G. R., Wang, S. Q., Liu, Y. H. and Bunch, T. D., 1996, "Toxic Effects of Ethylene Oxide Residues on Bovine Embryos in Vitro," *Toxicol.*, Vol. 108, Issue 1-2, pp. 33-38.

[22] Iwasaki, M., Takeda, K., Ito, M., Yara, T., Uehara, T. and Hori, M., 2007, "Effect of Low Level O_2 Addition to N_2 on Surface Cleaning by Nonequilibrium Atmospheric-Pressure Pulsed Remote Plasma," *Jpn. J. of Appl. Phys.*, Vol. 46, Issue 20-24, pp. L540-L542.

[23] Iwasaki, M., Matsudaira, Y., Takeda, K., Ito, M., Miyamoto, E., Yara, T., Uehara, T. and Hori, M., 2008, "Roles of Oxidizing Species in a Nonequilibrium Atmospheric-Pressure Pulsed Remote O_2/N_2 Plasma Glass Cleaning Process," *J. Appl. Phys.,* Vol. 103, Issue 2, 023303.

[24] Jung, M. H. and Choi, H. S., 2007, "Surface Treatment and Characterization of ITO Thin Films Using Atmospheric Pressure Plasma for Organic Light Emitting Diodes," *J. of Colloid Interface Sci.*, Vol. 310, Issue 2, pp. 550-558.

[25] Kim, Y., Lee, Y., Han, S. and Kim, K. J., 2006, "Improvement of Hydrophobic Properties of Polymer Surfaces by Plasma Source Ion Implantation," *Surf. Coat. Technol.*, Vol. 200, Issue 16-17, pp. 4763-4769.

[26] Klages, C. P. and Grishin, A., 2008, "Plasma Amination of Low-Density Polyethylene by DBD Afterglows at Atmospheric Pressure," *Plasma Proc. Polym.*, Vol. 5, Issue 4, pp. 368-376.

[27] Kwon, O. J., Tang, S., Myung, S. W., Lu, N. and Choi, H. S., 2005, "Surface Characteristics of Polypropylene Film Treated by an Atmospheric Pressure Plasma," *Surf. Coat. Technol.*, Vol. 192, Issue 1, pp. 1-10.

[28] Laroussi, M. and Leipold, F., 2004, "Evaluation of the Roles of Reactive Species, Heat, and UV Radiation in the Inactivation of Bacterial Cells by Air Plasmas at Atmospheric Pressure," *Int. J. Mass Spectrom.*, Vol. 233, Issue 1-3, pp. 81-86.

[29] Laroussi, M., Richardson, J. P. and Dobbs, F. C., 2002, "Effects of Nonequilibrium Atmospheric Pressure Plasmas on the Heterotrophic Pathways of Bacteria and on Their Cell Morphology," *Appl. Phys. Lett.*, Vol. 81, Issue 4, pp. 772-774.

[30] Lee, K., Paek, K. H., Ju, W. T. and Lee. Y., 2006, "Sterilization of Bacteria, Yeast, and Bacterial Endospores by Atmospheric-Pressure Cold Plasma Using Helium and Oxygen," *J. Microbiol.*, Vol. 44, Issue 3, pp. 269-275.

[31] Lee, Y. H. and Yeom, G. Y., 2005, "Properties and Applications of a Modified Dielectric Barrier Discharge Generated at Atmospheric Pressure," *Jpn. J. of Appl. Phys.*, Vol. 44, Issue 2, pp. 1076-1080.

[32] Lerouge, S., Wertheimer, M. R., Marchand, R., Tabrizian, M. and Yahia, L., 2000, "Effect of Gas Composition on Spore Mortality and Etching During Low-Pressure Plasma Sterilization," *J. Biomed. Mater. Res.*, Vol. 51, Issue 1, pp. 128-135.

[33] Lucas, A. D., Merritt, K., Hitchins, V. M., Woods, T. O., NcMamee, S. G., Lyle, D. B. and Brown, S. A., 2003, "Residual Ethylene Oxide in Medical Devices and Devices Material," *J. Biomed. Mater. Res. Part B: Appl. Biomater.*, Vol. 66B, Issue 2, pp. 548-552.

[34] Luque, J. and Crosley, D. R., 1999, "LIFBASE: Database and Special Simulation (version 1.5)," *SRI International Report* MP 99-009.

[35] Meiners, S., Salge, J. G. H., Prinz, E. and Förster, F., 1998, "Surface Modification of Polymer Materials by Transient Gas Discharges at Atmospheric Pressure," *Surf. Coat. Technol.*, Vol. 98, Issue 1-3, pp. 1121-1127.

[36] Moisan, M., Barbeau, J., Moreau, S., Pelletier, J., Tabrizian, M. and Yahia, L. H., 2001, *Int. J. Pharmac.*, Vol. 226, Issue 1-2, pp. 1-21.

[37] Morent, R., De, G. N., Gengembre, L., Leys, C., Payen, E., Van, V. S. and Schacht, E., 2008, "Surface Treatment of a Polypropylene Film with a Nitrogen DBD at Medium Pressure," *Eur. Phys. J. Appl. Phys.*, Vol. 43, Issue 3, pp. 289-294.

[38] Schütze, A., Jeong, J. Y., Babayan, S. E., Park, J., Selwyn, G. S. and Hicks, R. F., 1998, "The Atmospheric-Pressure Plasma Jet: A Review and Comparison to Other Plasma Sources," *IEEE Trans. Plasma. Sci.*, Vol. 26, Issue 6, pp. 1685-1694.

[39] Sharma, A., Pruden, A., Stan, O. and Collins, G. J., 2006, "Bacterial Inactivation Using an RF-Powered Atmospheric Pressure Plasma," *IEEE Trans. Plasma Sci.*, Vol. 34, Issue 4, pp. 1290-1296.

[40] Sheffield, J. B., 2007, "ImageJ, a Useful Tool for Biological Image Processing and Analysis," *Microsc. Microanal.*, Vol. 13, pp. 200-20.

[41] Sun, Y. Z., Qiu, Y. C., Nie, A. L. and Wang, X. D., 2007, "Experimental Research on Inactivation of Bacteria by Using Dielectric Barrier Discharge," *IEEE Trans. Plasma. Sci.*, Vol. 35, Issue 5, pp. 1496-1500.

[42] Takaki, K., Hosokawa, M., Sasaki, T., Mukaigawa, S. and Fujiwara, T., 2005, "Production of Atmospheric-Pressure Glow Discharge in Nitrogen Using Needle-Array Electrode," *Appl. Phys. Lett.*, Vol. 86, Issue 15, 151501.

[43] Wagner, H. E., Brandenburg, R., Kozlov, K. V., Sonnenfeld, A., Michel, P. and Behnke, J. F., 2003, "The Barrier Discharge: Basic Properties and Applications to Surface Treatment," *Vacuum*, Vol. 71, Issue 3, pp. 417-436.

[44] Walsh, J. L., Shi, J. J. and Kong, M. G., 2006, "Contrasting Characteristics of Pulsed and Sinusoidal Cold Atmospheric Plasma Jets," *Appl. Phys. Lett.*, Vol. 88, Issue 17, 171501.

[45] Wameck, P., 1998, Chemistry of the Natural Atmosphere, *Academic*, London.

[46] Wang, K., Li, J., Ren, C. S., Wang, D. Z. and Wang, Y. N., 2008, "Surface Modification of Polyethylene (PE) Films Using Dielectric Barrier Discharge Plasma at Atmospheric Pressure," *Plasma Sci. and Technol.*, Vol. 10, Issue 4, pp. 433-437.

[47] Xiong, Q., Lu, X. P., Jiang, Z. H., Tang, Z. Y., Hu, J., Xing, Z. L. and Pan, Y., 2008, "An Atmospheric Pressure Nonequilibrium Plasma Jet Device," *IEEE Trans. Plasma Sci.*, Vol. 36, Issue 4, pp. 986-987.

[48] Yi, C. H., Jeong, C. H., Lee, Y. H., Ko, Y. W. and Yeom, G. Y., 2004, "Oxide Surface Cleaning by an Atmospheric Pressure Plasma," *Surf. Coat. Technol.*, Vol. 177, pp. 711-715.

Appendix A.

Removal of the 2nd Order Radiation in OES Spectra

We have used two long-pass filters (280 and 400 nm) to measure the OES spectra (Fig. A-1 and A-2) to remove the 2nd order radiation caused by the grating system of the OES. We used the 280 nm long-pass filter for removing the NO-γ peak emission lines (215, 226.9, 237, 247 nm) to verify if our originally measured spectra in the range of 430-500 nm in the post-discharge region ($N_2 + 0.06\%$ O_2) contained the 2nd order NO-γ emission lines. We have observed that the corresponding 2nd order of NO-γ peak emission lines (430, 453.8, 474, 494 nm) disappeared. Similarly, the use of 400 nm long-pass filter have made the 674.2 nm emission (2nd order of 337.1 nm) disappeared in the post-discharge region (pure N_2). For reference, Fig. A-3 (below) shows the detailed classification of the originally unfiltered observed OES lines. The above verified that the originally measured OES spectra without optical filters require some proper modifications by removing these 2nd order emission lines, as now shown in the new Figs. A-4(a) and A-4(b). As shown in the new Fig. A-4(b), the N_2 1st positive emission line (580 nm) was clearly observed, especially as 0.06% of O_2 was added into the N_2.
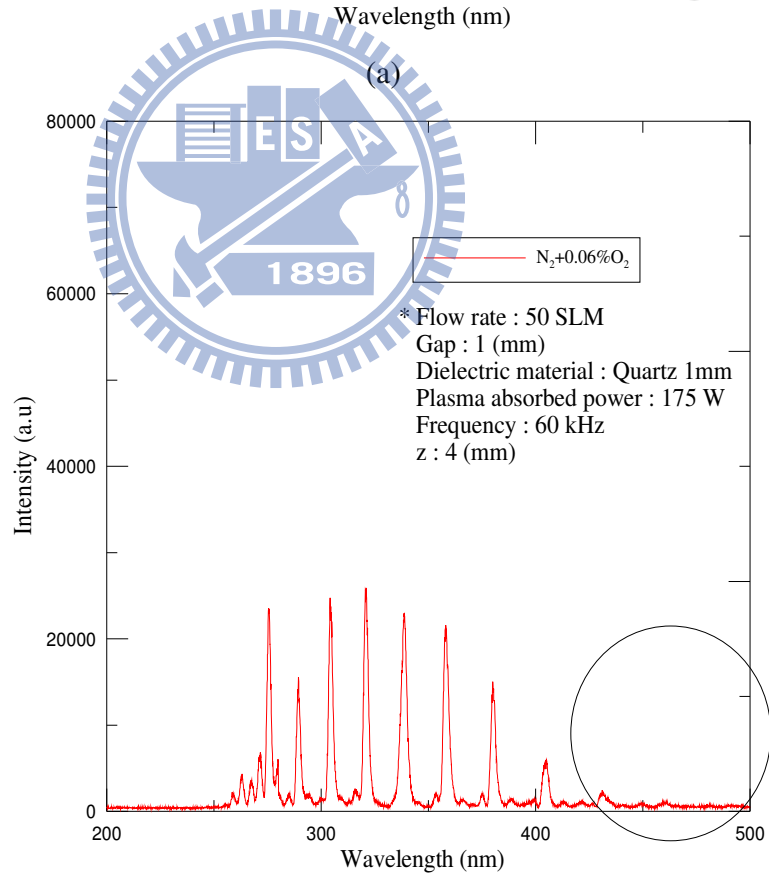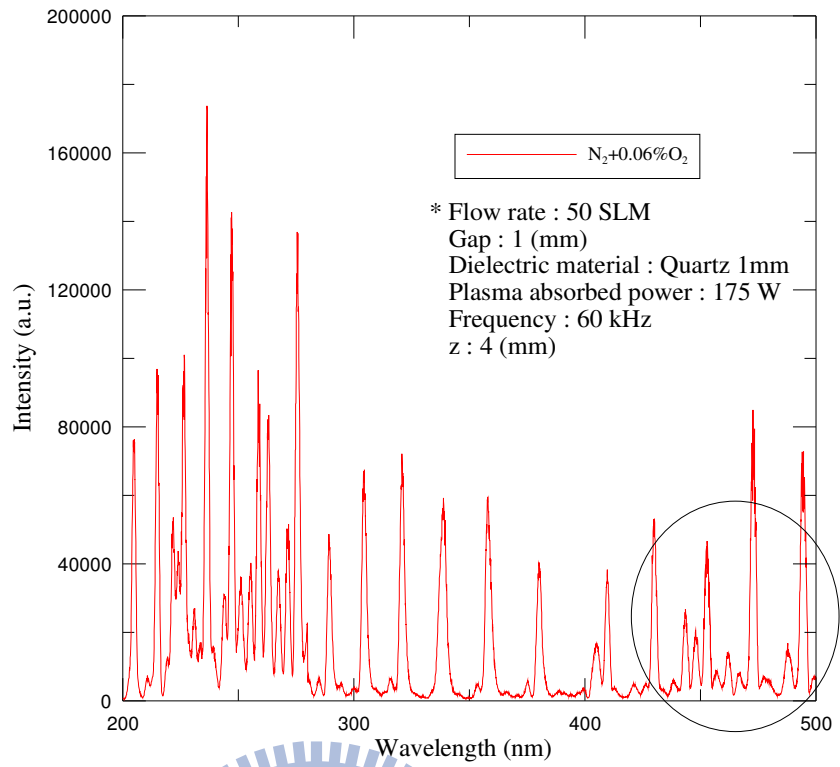
Fig. A-1 The OES spectra (a) without filter; (b) w/280 nm longpass filter

(a)

(b)
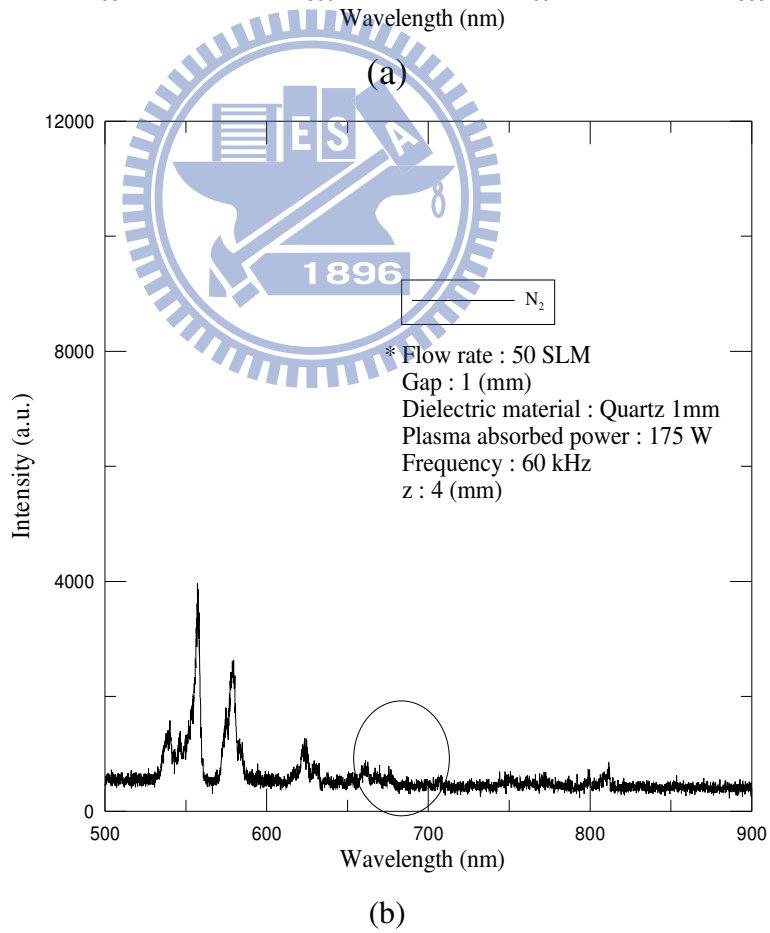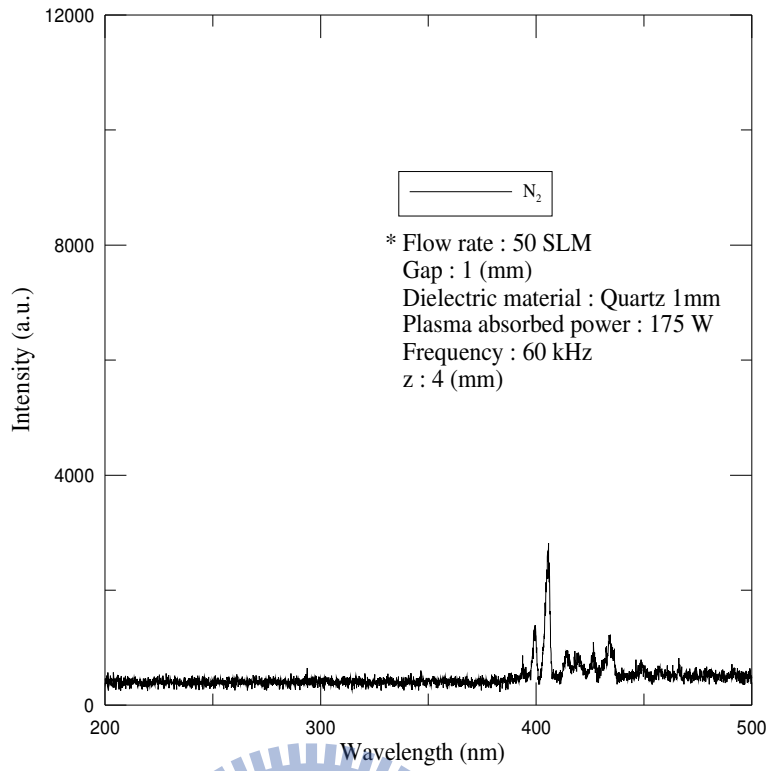
Fig. A-2 The OES spectra (a) 200-500 nm w/480 nm filter; (b) 500-900 nm w/400 nm

filter.
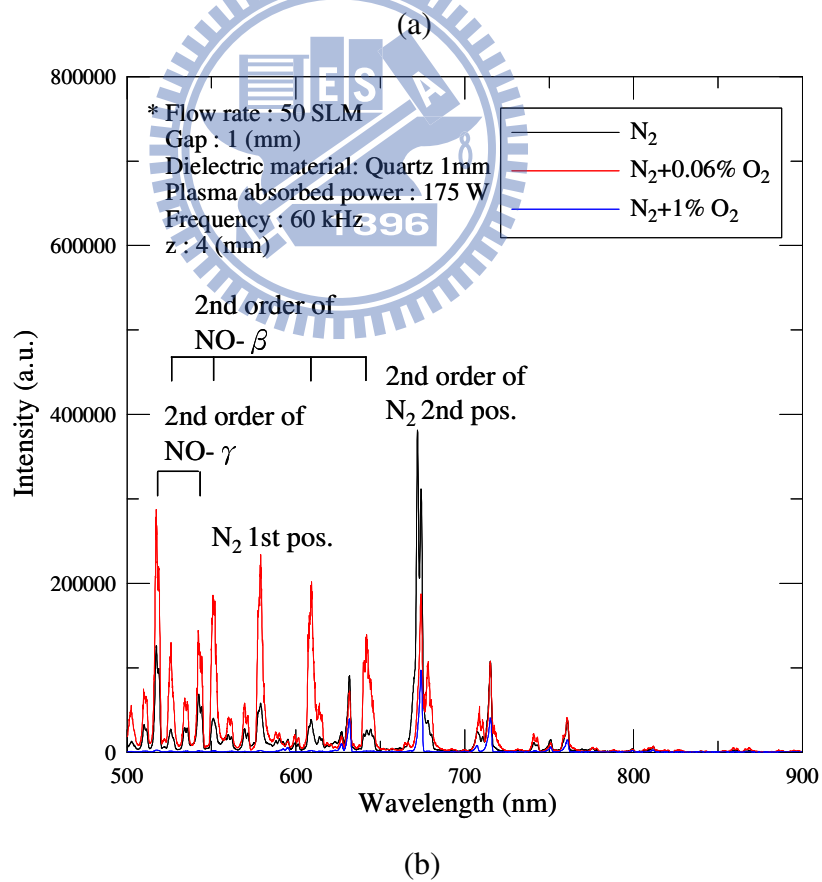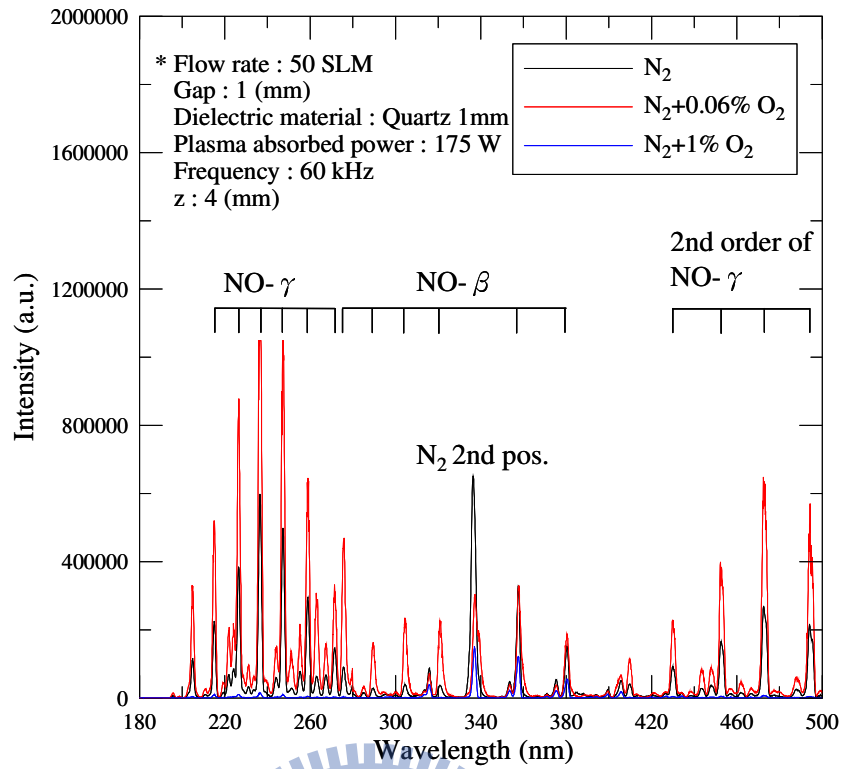
Fig. A-3 OES in the (a) 180-500 nm; (b) 500-900 nm for the post-discharge plasma (60

kHz, 50 SLM, absorbed power=175W).
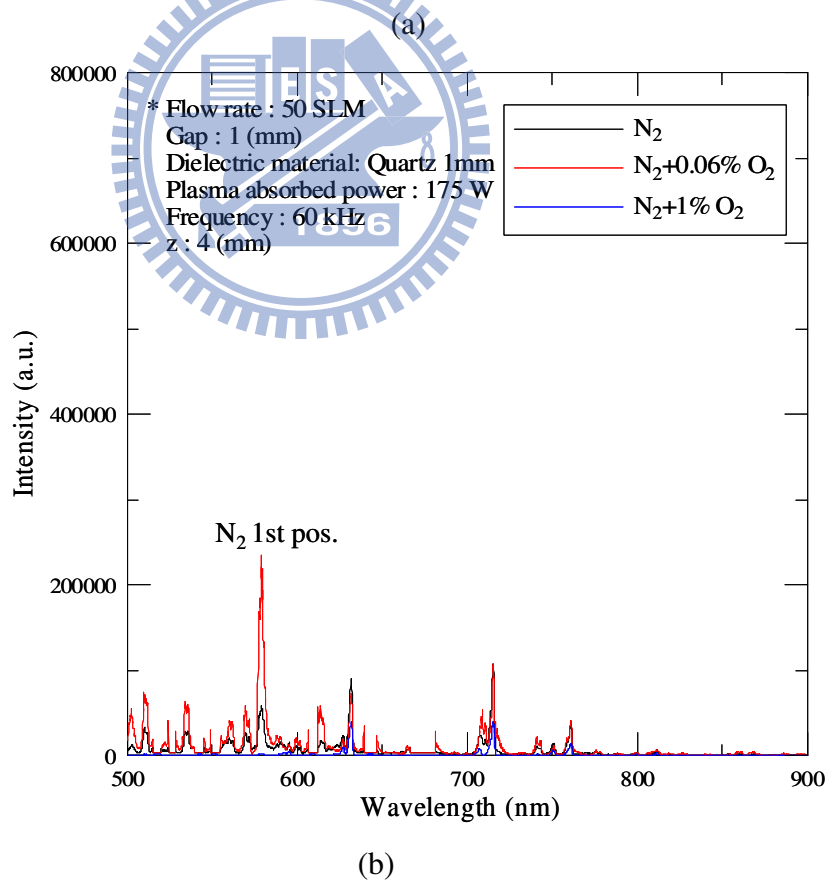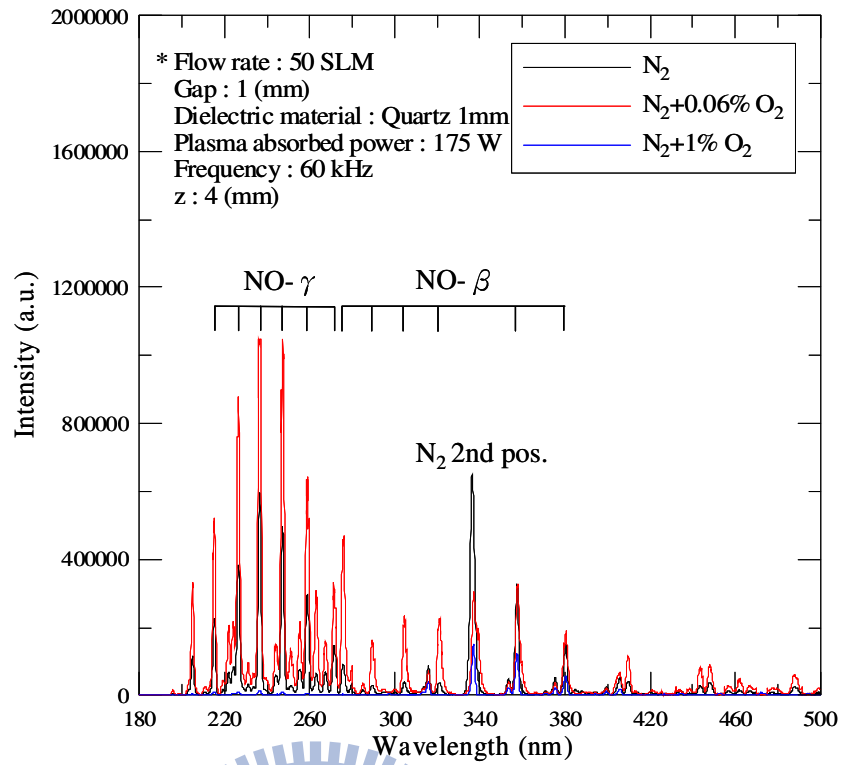
Fig. A-4 Optical emission spectra for the post-discharge plasma: (a) 180-500 nm; (b)

500-900 nm (60 kHz, 50 SLM, absorbed power=175W).

Table A-1 Major reaction channels in a nitrogen/oxygen discharge.

Gas	Major reaction channels (discharge region)	Major reaction channels (post-discharge region)	Comments
N_2 (+ impurity-level O_2)	$NO+e\rightarrow NO(A^2\Sigma^+)+e$ $NO+e\rightarrow NO(B^2\Pi)+e$ $N_2+e\rightarrow N_2(A^2\Sigma_u^+)+e$ $N_2+e\rightarrow N_2(C^3\Pi_u)+e$ $N_2+e\rightarrow N_2(B^3\Sigma_u^-)+e$ $N_2+e\rightarrow N_2(a'^1\Sigma_u^-)+e$	$NO(A^2\Sigma^+)\rightarrow NO+h\nu\,(200\sim260\,nm)\,NO-\gamma$ $NO(B^2\Pi)\rightarrow NO+h\nu\,(260\sim380\,nm)\,NO-\beta$ $N_2(C^3\Pi_u)\rightarrow N_2(B^3\Pi_g)+h\nu\,(337.1\,nm)\,N_2\,2nd\,positive$ $N_2(a'^1\Sigma_u^-)+NO\rightarrow N+O+N_2$ $N+N+N_2\rightarrow N_2(B^3\Pi_g)$ $N_2(B^3\Pi_g)\rightarrow N_2(A^2\Sigma_u^+)+h\nu\,(580\,nm)\,N_2\,1st\,positive$	N_2 (99.99%) OES: 1. NO-γ 2. NO-β 3. N₂ 2nd positive 4. N₂ 1st positive
N_2 +0.08% O_2	$NO+e\rightarrow NO(A^2\Sigma^+)+e$ $NO+e\rightarrow NO(B^2\Pi)+e$ $N_2+e\rightarrow N_2(A^2\Sigma_u^+)+e$ $N_2+e\rightarrow N_2(C^3\Pi_u)+e$ $N_2+e\rightarrow N_2(B^3\Sigma_u^-)+e$ $N_2+e\rightarrow N_2(a'^1\Sigma_u^-)+e$	$NO+N_2(A^2\Sigma_u^+)\rightarrow NO(A^2\Sigma^+)$ $NO(A^2\Sigma^+)\rightarrow NO+h\nu\,(200\sim260\,nm)\,NO-\gamma$ $NO+N_2(A^2\Sigma_u^+)\rightarrow NO(B^2\Pi)$ $NO(B^2\Pi)\rightarrow NO+h\nu\,(260\sim380\,nm)\,NO-\beta$ $N_2(C^3\Pi_u)\rightarrow N_2(B^3\Pi_g)+h\nu\,(337.1\,nm)\,N_2\,2nd\,positive$ $N_2(a'^1\Sigma_u^-)+NO\rightarrow N+O+N_2$ $N+N+N_2\rightarrow N_2(B^3\Pi_g)$ $N_2(B^3\Pi_g)\rightarrow N_2(A^2\Sigma_u^+)+h\nu\,(580\,nm)\,N_2\,1st\,positive$	Trace O_2 addition OES: 1. NO neutral species increase 2. NO-γ increase 3. NO-β increase 4. N₂ 2nd positive decrease 5. N₂ 1st positive increase
N_2 +1% O_2	Aboundant oxygen quench $NO+e\rightarrow NO(A^2\Sigma^+)+e$ $NO+e\rightarrow NO(B^2\Pi)+e$ $N_2+e\rightarrow N_2(A^3\Sigma_u^+)+e$ $N_2+e\rightarrow N_2(C^3\Pi_u)+e$ $N_2+e\rightarrow N_2(B^3\Pi_g)+e$ $N_2+e\rightarrow N_2(a'^1\Sigma_u^-)+e$	$NO(A^2\Sigma^+)\rightarrow NO+h\nu\,(200\sim260\,nm)\,NO-\gamma$ $NO(B^2\Pi)\rightarrow NO+h\nu\,(260\sim380\,nm)\,NO-\beta$ $N_2(C^3\Pi_u)\rightarrow N_2(B^3\Pi_g)+h\nu\,(337.1\,nm)\,N_2\,2nd\,positive$ $N_2(a'^1\Sigma_u^-)+NO\rightarrow N+O+N_2$ $N+N+N_2\rightarrow N_2(B^3\Pi_g)$ $N_2(B^3\Pi_g)\rightarrow N_2(A^2\Sigma_u^+)+h\nu\,(580\,nm)\,N_2\,1st\,positive$	Abundant O_2 addition OES: 1. NO-γ decrease 2. NO-β decrease 3. N₂ 2nd positive decrease 4. N₂ 1st positive decrease

Appendix B.

Tolerance Analysis

1. Flow rate

   Flow meter min. scale 2 SLM (0~100 SLM, as N_2: 50 SLM)

   Flow meter min. scale 0.2 SLM (0~10 SLM, as N_2, O_2, compressed air: 10 SLM)

   Flow meter min. scale 0.02 SLM (0~1 SLM, as CF_4: 0.1 SLM)

   N_2 (50 SLM) Flow rate tolerance$=\pm\dfrac{2/2}{50}\times100=\pm2\%$

   N_2, O_2, compressed air (10 SLM) Flow rate tolerance$=\pm\dfrac{0.2/2}{10}\times100=\pm1\%$

   CF_4 (0.1 SLM) Flow rate tolerance$=\pm\dfrac{0.02/2}{0.2}\times100=\pm5\%$

2. Z distance

   3D-table min. scale 0.05 mm

   Z=2mm tolerance$=\pm\dfrac{0.05/2}{2}\times100=\pm1.25\%$

3. Output power from power supply

   Quasi-pulsed power min. scale 10W

   Nitrogen-based DBD APPJ 500 W tolerance$=\pm\dfrac{10/2}{500}\times100=\pm1\%$

   Air-based DBD APPJ 300 W tolerance$=\pm\dfrac{10/2}{300}\times100=\pm1.67\%$

4. Frequency

   Quasi-pulsed power min. scale 0.01 kHz

   Nitrogen-based DBD APPJ 60 kHz tolerance$=\pm\dfrac{0.01/2}{60}\times100=\pm0.01\%$

$$\text{Air-based DBD APPJ 30 kHz tolerance} = \pm\frac{0.01/2}{30}\times100 = \pm0.02\%$$

5. Contact angle

   CAs are obtained by averaging over three to five measurements over a region of a
   ITO glass/PP film with ±3°.

   $$\text{PP film CA }(23^\circ)\text{ tolerance} = \pm\frac{3}{23}\times100 = \pm13.04\%$$

6. AFM Roughness (nm)

   Surface roughness are obtained by averaging over three to five measurements over
   a region of a ITO glass/PP film with ±0.05 nm.

   $$\text{ITO glass untreated roughness 0.68 nm tolerance} = \pm\frac{0.05}{0.68}\times100 = \pm7.35\%$$
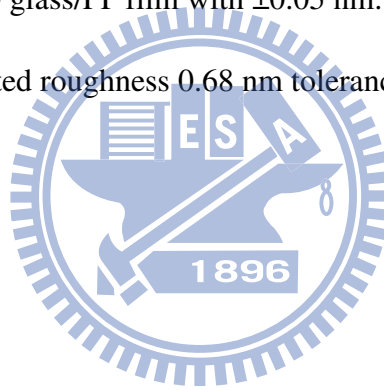
Table 1-1 Breakdown voltages of the plasma discharge [Schutze et al., 1998]

Source	V_b (kV)
Low-pressure discharge	$0.2 - 0.8$
Arc and plasma torch	$10 - 50$
Corona	$10 - 50$
Dielectric barrier discharge	$5 - 25$
Plasma jet	$0.05 - 0.2$

Table 1-2 Densities of charge species in the plasma discharge [Schutze et al., 1998]

Source	Plasma density (cm^{-3})
Low-pressure discharge	$10^8 - 10^{13}$
Arc and plasma torch	$10^{16} - 10^{19}$
Corona	$10^9 - 10^{13}$
Dielectric barrier discharge	$10^{12} - 10^{15}$
Plasma jet	$10^{11} - 10^{12}$

Table 1-3 Densities of oxygen species in the discharges [Schutze et al., 1998]

Source	Density (cm^{-3})		
	O^+, O_2^+, O^-	O	O_3
Low-pressure discharge	10^{10}	10^{14}	$<10^{10}$
Arc and plasma torch	10^{15}	10^{18}	$<10^{10}$
Corona	10^{10}	10^{12}	10^{18}
Dielectric barrier	10^{10}	10^{12}	10^{18}
Plasma jet	10^{12}	10^{16}	10^{16}

Table 1-4 Main plasma reaction [Eliasson, B., 1991]

Electron/Molecular Reactions

Excitation:	$e + A_2$	$\rightarrow$	$A_2^* + e$
Dissociation	$e + A_2$	$\rightarrow$	$2A + e$
Attachment	$e + A_2$	$\rightarrow$	A_2^-
Dissociative attachment	$e + A_2$	$\rightarrow$	$A^- + A$
Ionization	$e + A_2$	$\rightarrow$	$A_2^+ + 2e$
Dissociative ionization	$e + A_2$	$\rightarrow$	$A^+ + A + e$
Recombination	$e + A_2^+$	$\rightarrow$	A_2
Detachment	$e + A_2^-$	$\rightarrow$	$A_2 + 2e$

Atomic/Molecular Reactions

Pennning Dissociation	$M^* + A_2$	$\rightarrow$	$2A + M$
Pennning Ionization	$M^* + A_2$	$\rightarrow$	$A_2^+ + M + e$
Charge Transfer	$A^\pm + B$	$\rightarrow$	$B^\pm + A$
Ion Recombination	$A^- + B^+$	$\rightarrow$	AB
Neutral Recombination	$A + B + M$	$\rightarrow$	$AB + M$

Decomposition

Electronic	$e + AB$	$\rightarrow$	$A + B + e$
Atomic	$A^* + B_2$	$\rightarrow$	$AB + B$

Synthesis

Electronic	$e + A$	$\rightarrow$	$A^* + e$
	$A^* + B$	$\rightarrow$	AB
Atomic	$A + B$	$\rightarrow$	AB

Table 2-1 Summary of the DBD-APPJ system.

Item	Description	Model	Specification
1	Planar DBD APPJ	APPL Designed	(1) Two parallel copper electrodes $50 \times 50 \times 8$ mm (2) Two quartz plate $70 \times 70 \times 1$ mm (surface modification) (3) Two ceramic plate $70 \times 70 \times 2$ mm (inactivation) (4) Gap 1mm (5) Electrodes with embedded cooling water
2	Cooling System	APPL Designed	(1) The inlet cooling temperature control was $20 \pm 2℃$ (2) The water pressure control was 1.6 ± 0.1 kg/cm^2 (3) The diameter of the cooling pipe was 1/4"
3	Power Supply	Genius 2 (EN Tech. Inc.)	(1) Frequency (20~60 KHz) (2) Peak current (max. 4A) (3) Peak voltage (max. 15 kV) (4) Power (max. 2 kW)
4	Gas Supply System	APPL Designed	(1) N_2 (99.99%), O_2 (99.99%), CF_4 (99.99%) (2) Compressed air (oil-less compressor)
5	(1) Venting Chamber (2) Induction motor (3) Frequency converter	(1) APPL Designed (2) Tatung EBFC (3) TECO 7300CV	(1) Cylindrical chamber size was **D**600 $\times$ **L**700 (mm), the exhaust pipe (diameter 210 mm) (2) frequency converter (0~60Hz)
6	Non-Stationary Stage	U-S1-D0-H080378 (Unice E-O Service Inc.)	(1) Maximum traveling distance 20 cm (2) USB driver (3) Sample plate size was 10×10 cm (4) Passing speed in the range of 1-9 cm/s

Table 2-2 Summary of the instrumentation.

Item	Description	Model	Specification
1	(1) Thermocouple (2) Digital indicator	(1) K-type (2) BTC-900 (Brainchild)	Temperature range: -50-500 ℃
2	(1) High-voltage probe (2) Current monitor (3) Digital oscilloscope	(1) P6015A (Tektronix) (2) IPC CM-100-MG (Ion Physics Co. Inc.) (3) TDS1012B (Tektronix)	Measured input voltage and output current waveforms
3	(1) Voltage probe (2) Capacitance	(1) P2220 (Tektronix) (2) 6.8 nF	Measured by the technique of the "Lissajous figure" (Q-V characteristics)
4	(1) Monochromator (2) Photomultiplier tube (3) Fiber (4) Collimating lenses	(1) SP 2500 (PI Acton) (2) R928 (Hamamatsu) (3) BTW-FPC-600-0.22-1.5-UV (Ocean Optics) (4) 74-UV (Ocean Optics)	(1) Grating: 180~900 nm with 1200-g/mm (Holographic, 300-nm Blaze and 500-nm Blaze) (2) Fiber: diameter 600 μ m
5	OES software	(1) Plasus SpecLine (Ocean Optics) (2) LIFBASE (Luque *et al.,* 1999)	(1) Species identification (2) Gas temperature measurement
6	(1) Ozone monitor (2) FTIR	(1) 450 (API) (2) Tensor 27 (Bruker)	(1) Maximum 1000 ppm (2) Infrared absorption spectra (800-3600 cm^{-1})
7	Contact angle machine	GH100 (KRÜSS)	(1) Measuring the hydrophilic properties (2) Used a 2 µL drop of de-ionized water placed on the surface using a micropipette (3) The values of the static contact angle were obtained using Laplace-Young curve fitting to measure the 10 average values

8	AFM	D5000 (Veeco)	(1) Surface Profile measurement (2) Max. horizontal scan area: 80×80 μm^2 (3) Max. vertical scan area: 6 μm
9	SEM	S-470 type II (Hitachi)	(1) Bacteria morphological observation (2) Electron voltage: 5kV (3) Amplification factor: 30k
10	XPS	(1) Quantera SXM (PHI) (2) 1600 ECSA (PHI)	(1) Scanning Monochromated Aluminum anode, chamber pressure below $5×10^{-10}$ torr for ITO glass (2) Mg anode at 250W and 15KV, 1253.6 eV, the electron take-off angle respect to the PP film surface was 45°, chamber pressure below $2×10^{-8}$ torr for PP film
11	Digital Camera	D1H (Nikon)	(1) The image sensor was 12-bit RGB CCD with 2.74 million pixels. (2) Imaging exposure time: 0.2 sec for 1 mm-side view, 2 sec for 50 mm-front view (post-discharge region) (3) Imaging exposure time: 0.2 sec for bottom view (discharge region)

Table 2-3 Element peak line information of NO (220-280 nm)

Element	Line (nm)	I (rel.)	Energy (eV) lower-upper	ΔE (eV)	Transition lower-upper	Quantum number lower-upper	Comment
NO	226.28	800	$0.00 - 5.45$	5.45	X2Pi – A2Sig+	$0 - 0$	
NO	237.02	1000	$0.00 - 5.45$	5.45	X2Pi – A2Sig+	$1 - 0$	Kaplan's. System
NO	247.11	1000	$0.00 - 5.45$	5.45	X2Pi – A2Sig+	$2 - 0$	
NO	258.75	900	$0.00 - 5.45$	5.45	X2Pi – A2Sig+	$3 - 0$	
NO	271.32	800	$0.00 - 5.45$	5.45	X2Pi – A2Sig+	$4 - 0$	

Table 2-4 Test conditions of planar DBD APPJ in PP film modification application.

Discharge gas	N_2 (99.99%) 、 O_2/N_2 (0.004~1.6%)
Flow rate	50 slm (16.5 m/s)
Dielectric material	Quartz (SiO_2, t=1 mm)
Gap distance	1 mm
Output power from power supply	60 kHz, 500 W, power density (Large)
Plasma absorbed power	175 W
Treatment distance	2 – 20 mm
Treatment sample	PP film (t=0.31 mm)
ITO glass treatment	Stationary: 5 sec Non-stationary speed: 0.5 - 8 cm/s

Table 2-5 Test conditions of planar DBD APPJ in ITO glass surface cleaning application.

Discharge gas	N_2 (99.99%) 、 O_2/N_2 (0.004~1.6%)
Flow rate	50 slm (16.5 m/s)
Dielectric material	Quartz (SiO_2, t=1 mm)
Gap distance	1 mm
Output power from power supply	60 kHz, 500 W, power density (Large)
Plasma absorbed power	175 W
Treatment distance	2 – 20 mm
Treatment sample	ITO glass (In_2O_3)
ITO glass treatment	Stationary: 5 sec Non-stationary speed: 1 - 9 cm/s

Table 2-6 Test conditions of planar DBD APPJ in *E. coli* and *B. subtilis* sterilization.

Discharge gas	N$_2$ (99.99%)、O$_2$ (99.99%) 、Compressed air
Flow rate	10 slm (3.3 m/s)
Dielectric material	Ceramic (Al$_2$O$_3$, t=2 mm)
Gap distance	1 mm
Output power from power supply	30 kHz, 300 W, power density (Large)
Treatment distance	4 – 20 mm
Treatment bacterial cell	*E. coli* and *B. subtilis* (3.2✕10^7 CFU/mL)
Bacterial cell treatment	Non-stationary speed: 1 cm/s
Treatment times	2-18 passes
Treatment residence time	0.2 – 1.8 sec
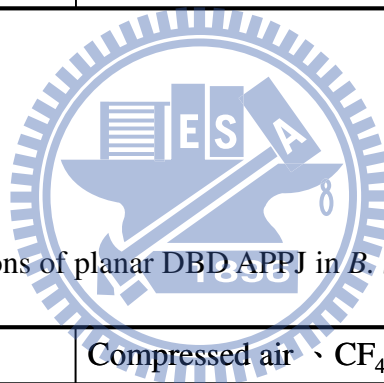
Table 2-7 Test conditions of planar DBD APPJ in *B. subtilis* spore sterilization.

Discharge gas	Compressed air 、CF$_4$/air (2%)
Flow rate	5 slm (1.65 m/s)
Dielectric material	Ceramic (Al$_2$O$_3$, t=2 mm)
Gap distance	1 mm
Output power from power supply	30 kHz, 300 W, power density (Large)
Treatment distance	14 mm
Treatment bacterial cell	*B. subtilis* spore (10^5 、10^6 、10^7 spore/mL)
Bacterial cell treatment	Non-stationary speed: 1 cm/s
Treatment times	2-18 passes
Treatment residence time	0.2 – 1.8 sec

Table 3-1 FTIR measured absorption peak value of 1055 cm^{-1} for ozone in the post-discharge region for N_2, compressed air, and O_2 discharges in z distance 4-20mm.

z distance (mm)	N_2 plasma	Compressed air plasma	O_2 plasma
4	0.00017	0.032	0.138
8	0.00037	0.033	0.135
12	0.0004	0.028	0.14
16	0.00001	0.0188	0.104
20	0.00001	0.0152	0.083
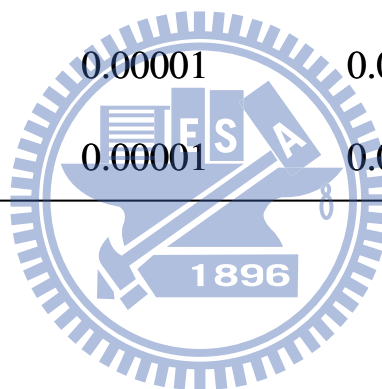
Table 4-1 Measured contact angles of non-stationary PP film at different O_2/N_2 ratios after plasma treatment (z=2 mm, v= 0.5 cm/s)

O_2/N_2 (%)	Contact angle (^{o})
0	75
0.002	74
0.004	73
0.006	72
0.008	70
0.01	77
0.012	77
0.014	76
0.016	74
0.019	73
0.021	73
0.06	26
0.2	27
0.4	33
0.8	39
1.6	77

Table 4-2 Measured contact angles of non-stationary PP film at four typical O_2/N_2 ratios after plasma treatment (Z=2 mm, v= 0.5-8 cm/s)

V (cm/s)	O_2/N_2 (%)			
	0.06	0.20	0.40	0.80
0.5	26	27	33	39
1	33	45	50	72
2	80	82	94	94
4	97	91	101	98
8	100	97	103	103
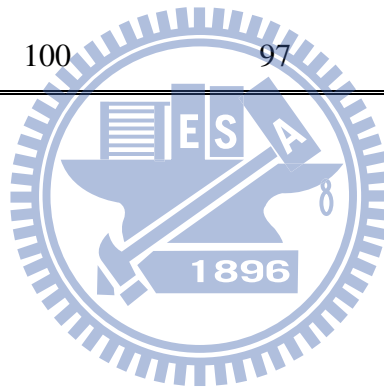
Table 4-3 RMS roughness of PP film at different treating distances measured by AFM

z (mm)	RMS roughness (nm)
Untreated	40.4
2	19.6
6	17.8
20	28.6

Table 4-4 Atomic percent concentration and ratio and percentage peak area of XPS C1s core level spectra of untreated PP and atmospheric- pressure plasma treated PP

O_2/N_2 (%)	z (mm)	Speed (cm/s)	Exposure time (s)	Contact angle (°)	C (%)	N (%)	O (%)	O/C	$\frac{C-C}{C1s}$ (%)	$\frac{C-O}{C1s}$ (%)	$\frac{C=O}{C1s}$ (%)	$\frac{COO}{C1s}$ (%)
0	2	0	5	35	58.1	0.5	41.4	0.7	85.3	7.6	6.9	0.1
0	6	0	5	23	58.0	0.2	41.3	0.7	88.8	4.9	5.8	0.6
0	20	0	5	95	70.8	0	29.3	0.4	96.3	3.8	0	0
0.06	2	0	5	24	53.9	1.5	44.6	0.8	88.3	8.0	3.5	0.2
0.06	6	0	5	26	52.7	0	47.3	0.9	92.7	4.2	3.1	0
0.06	20	0	5	96	67.9	0	32.2	0.5	96.2	3.8	0	0
0	2	1	0.1	87	65.0	0.5	34.6	0.5	89.2	10.8	0	0
0.06	2	1	0.1	33	62.4	0.4	37.3	0.6	95.4	4.6	0	0
untreated				103	88.9	0	11.1	0.1	97.1	2.9	0	0
untreated (ethanol)				103	83.6	0	16.4	0.2	99.9	0.1	0	0

Table 5-1 XPS measured chemical composition of ITO glass after planar-DBD APPJ treatment

O_2/N_2 (%)	z (mm)	Speed (cm/s)	Exposure time (s)	Contact angle (°)	C (%)	N (%)	O (%)	In (%)	Sn (%)	O/C
0	4	0	5	37	30.29	5.04	42.47	20.09	2.11	1.4
0	10	0	5	20	17.47	0.89	51.69	27.05	2.90	2.96
0.06	4	0	5	29	18.83	1.18	49.55	27.18	3.26	2.63
0.06	10	0	5	22	17.38	0.74	51.29	27.65	2.93	2.95
	Untreated ITO			84	33.83	0.63	39.38	23.50	2.66	1.16

Table 5-2 RMS roughness of ITO glass at different treating distances measured by AFM.

O_2/N_2 (%)	z (mm)	Speed (cm/s)	Exposure time (s)	Contact angle (°)	RMS roughness (nm)
0	4	0	5	37	0.66
0	10	0	5	20	0.62
0	20	0	5	32	0.63
0	4	9	0.01	73	0.63
0.06	4	0	5	29	0.53
0.06	10	0	5	22	0.53
0.06	20	0	5	54	0.54
0.06	4	9	0.01	42	0.69
	Untreated ITO			84	0.68

Table 6-1 Summary of survival rates under different treatment distances for *E. coli* bacteria (10^7 CFU/mL) on petri dishes for different gas discharges. Other discharge parameters: gas flow rate=10 slm, stage moving speed=1cm/sec, output power from power supply=300 W, gap=1 mm, and Z=20 mm.

Working gas	Plasma exposure time (number of passes)	Survival rate (%)
N₂	2/6/10/14/18	94/84/85/95/80
Compressed air	2/6/10/14/18	5/1/0/0/0
O₂	2/6/10/14/18	89/20/3/1/0

Table 6-2 Summary of survival rates under different treatment distances for *B. subtilis* bacteria (10^7 CFU/mL) on petri dishes for different gas discharges. Other discharge parameters: gas flow rate=10 slm, stage moving speed=1cm/sec, output power from power supply=300 W, gap=1 mm, and z= 20 mm.

Working gas	Plasma Exposure time (number of passes)	Survival rate (%)
N₂	2/6/10/14/18	99/94/99/98/97
Compressed air	2/6/10/14/18	88/63/18/0/0
O₂	2/6/10/14/18	80/61/18/3/0

Table 7-1 Chemical composition of PP film after planar-DBD APPJ treatment (30 kHz, output power from power supply=300 W)

CF_4/air (%)	z (mm)	Speed (cm/s)	Exposure time (s)	Passes	C (%)	O (%)	F (%)	O/C
0	14	1	3.4	34	73.89	26.11	0	0.35
2	14	1	3.4	34	70.98	28.94	0.08	0.41
Untreated pp film				34	77.01	22.99	0	0.30

Table 7-2 Summary of survival rates under different bacterial number treatments for *B. subtilis* spore bacteria on petri dishes for air discharges. Other discharge parameters: gas flow rate=5 slm, stage moving speed=1cm/sec, output power from power supply=300 W, gap=1 mm, and Z=14 mm.

The number of *B. subtilis* spore (spore/mL)	Plasma exposure time (number of passes)	Survival rate (%)
10^5	2/6/10/14/18	92/96/81/80/80
10^6	2/6/10/14/18	91/97/98/98/98
10^7	2/6/10/14/18	99/97/997/97/97

Table 7-3 Summary of survival rates under different bacterial number treatments for *B. subtilis* spore bacteria on petri dishes for CF$_4$/air (2%) discharges. Other discharge parameters: gas flow rate=5 slm, stage moving speed=1cm/sec, output power from power supply=300 W, gap=1 mm, and Z=14 mm.

The number of *B. subtilis* spore (spore/mL)	Plasma exposure time (number of passes)	Survival rate (%)
10^5	2/6/10/14/18	57/3/0/0/0
10^6	2/6/10/14/18	98/23/0/0/0
10^7	2/6/10/14/18	96/9/0/0/0
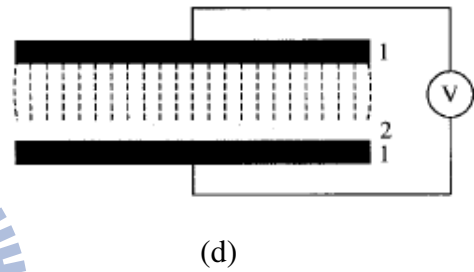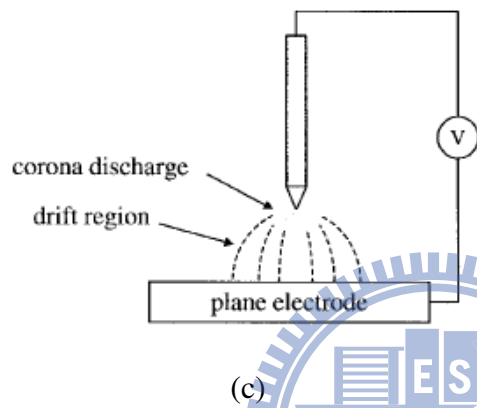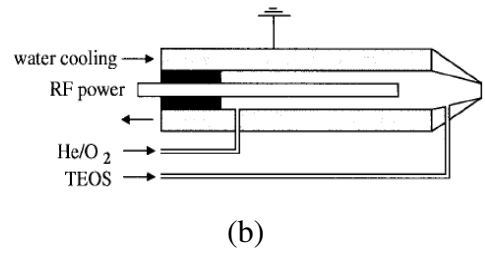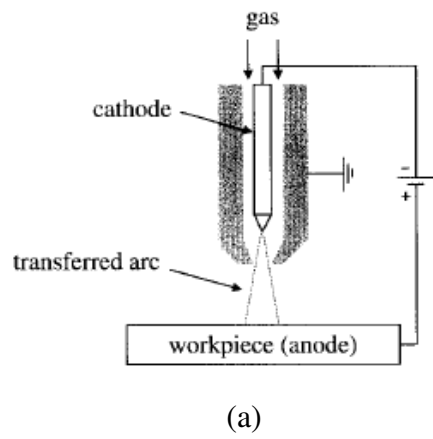
Fig. 1-1 Types of atmospheric-pressure plasma: (a) transferred arc; (b) plasma jet; (c) corona discharge; and (d) dielectric barrier discharge. [Schutze *et al*., 1998].
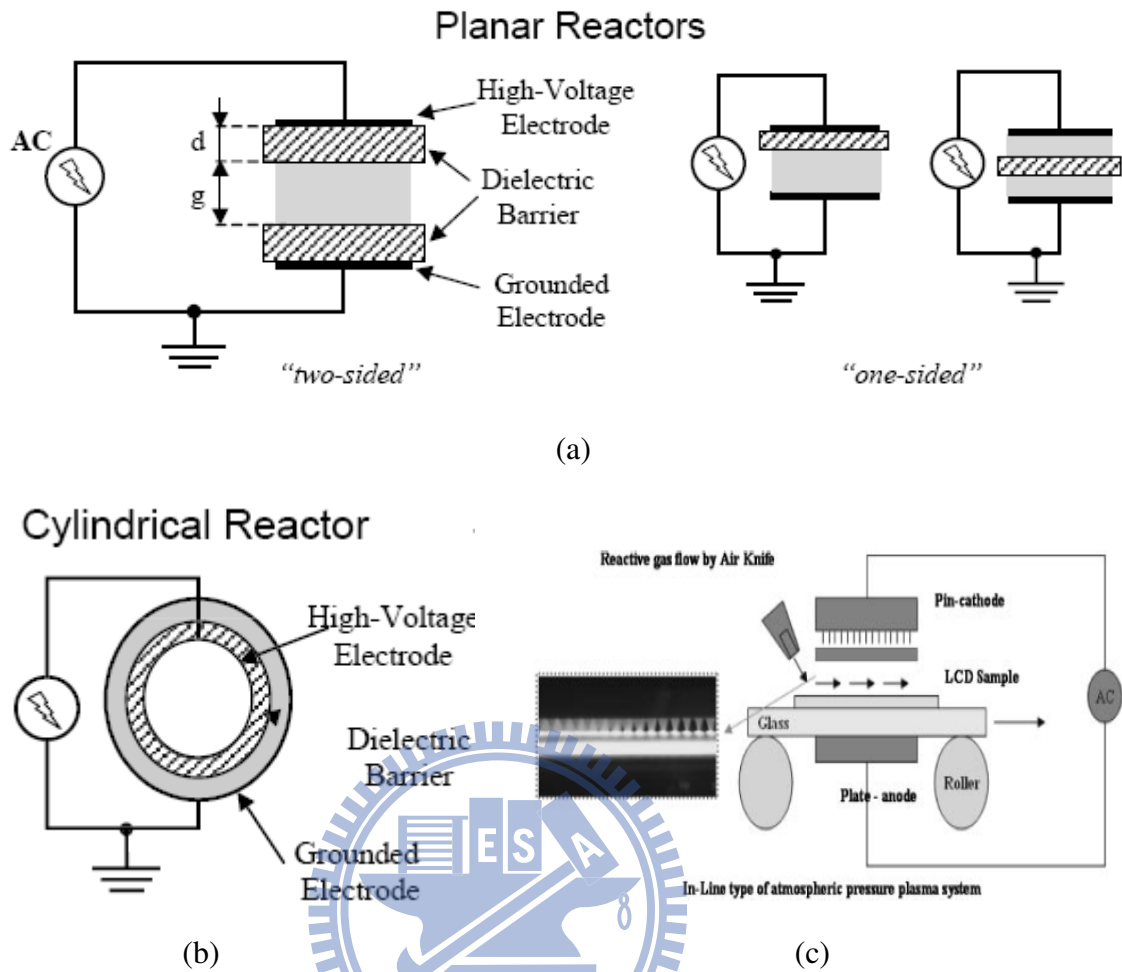
Fig. 1-2 Typical electrode arrangements of barrier discharges: (a) planar reactor; (b) cylindrical reactor; and (c) pin-to-plate discharge. [Wagner, *et al.*, 2003 and Lee, *et al.*, 2005]
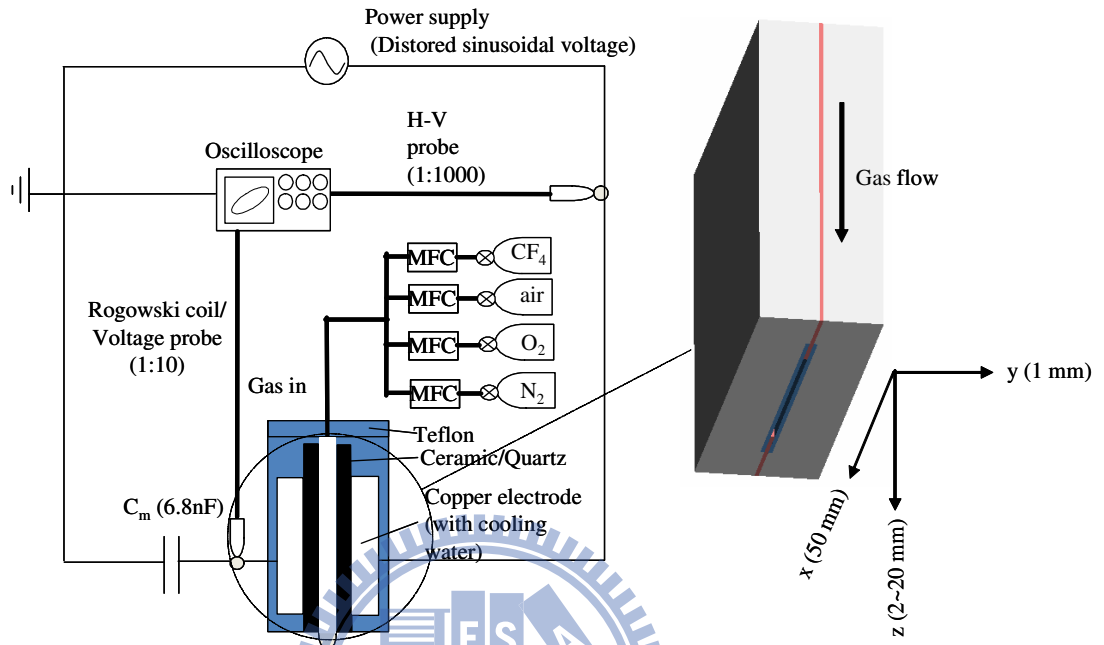
Fig. 2-1 Schematic sketch of a planar DBD APPJ
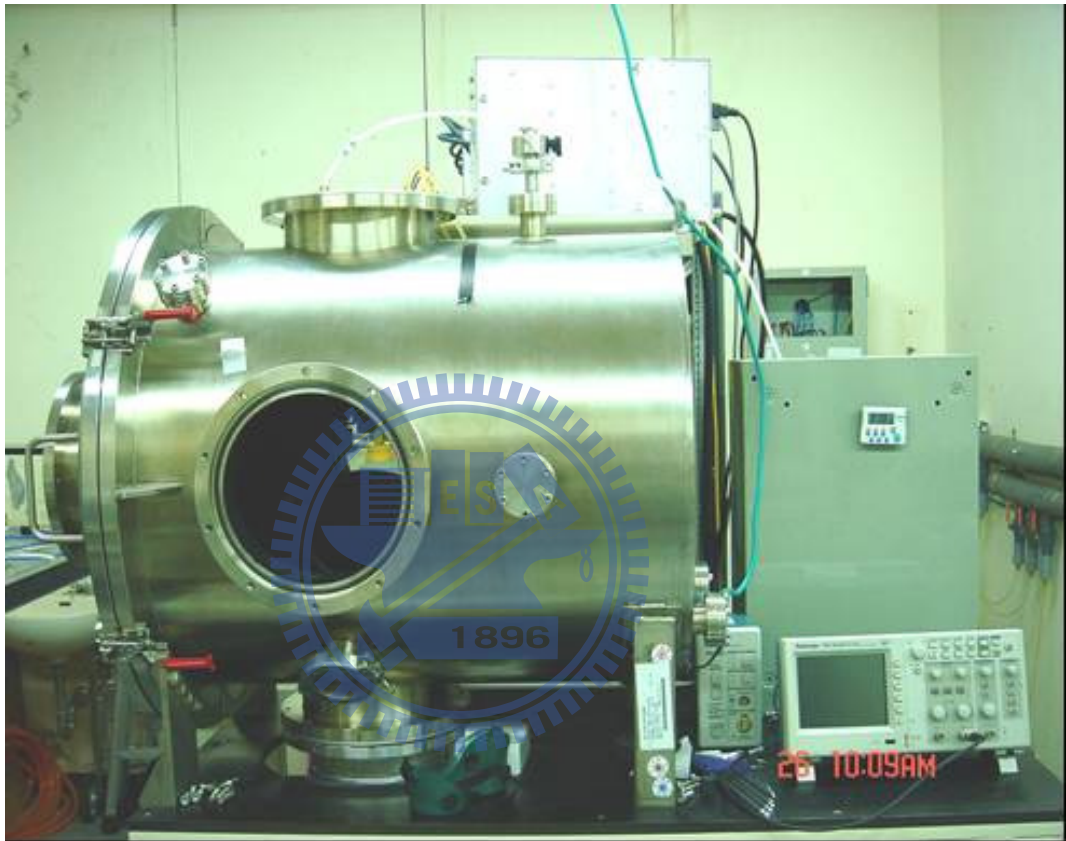
Fig. 2-2 Image of the venting chamber.
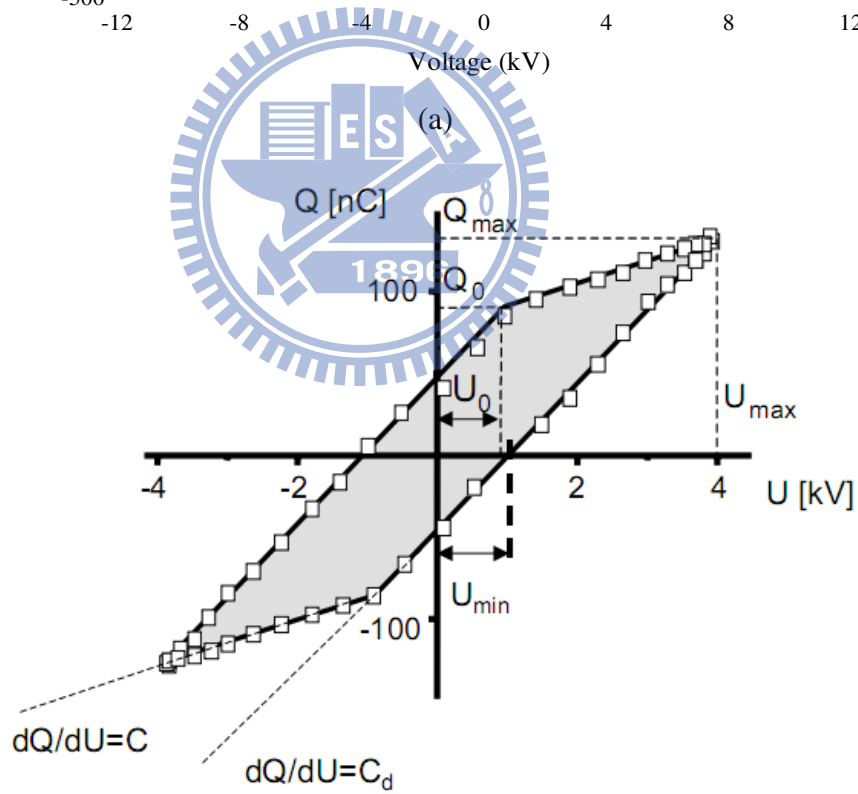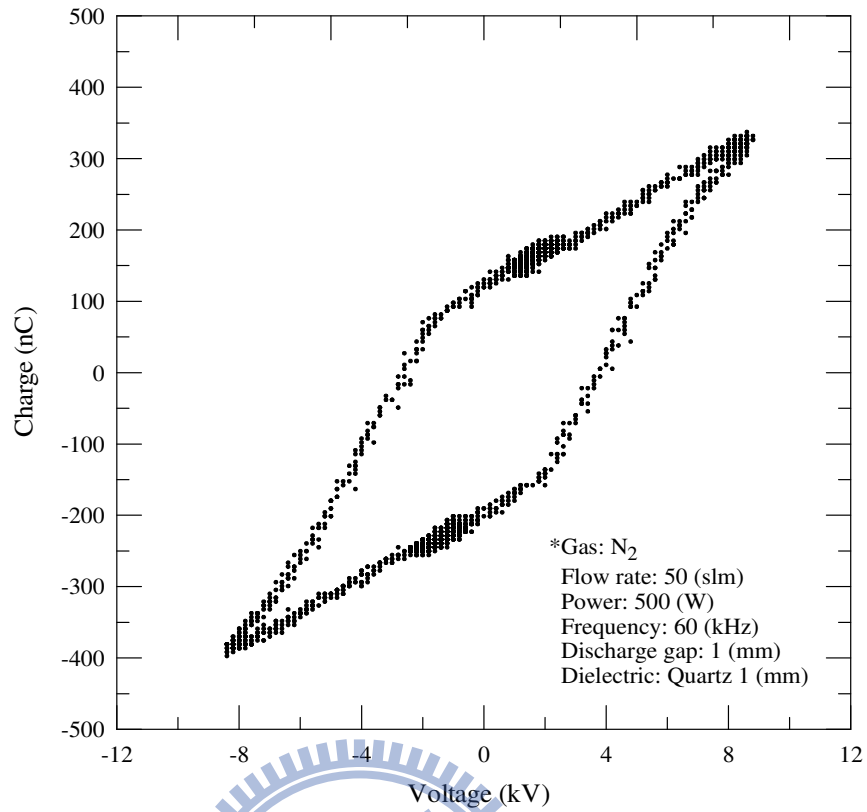
Fig. 2-3 Typical Lissajous figure for a parallel-plate DBD APPJ: (a) distorted-sinusoidal voltage power supply; and (b) AC power supply [Wagner et al. 2003].
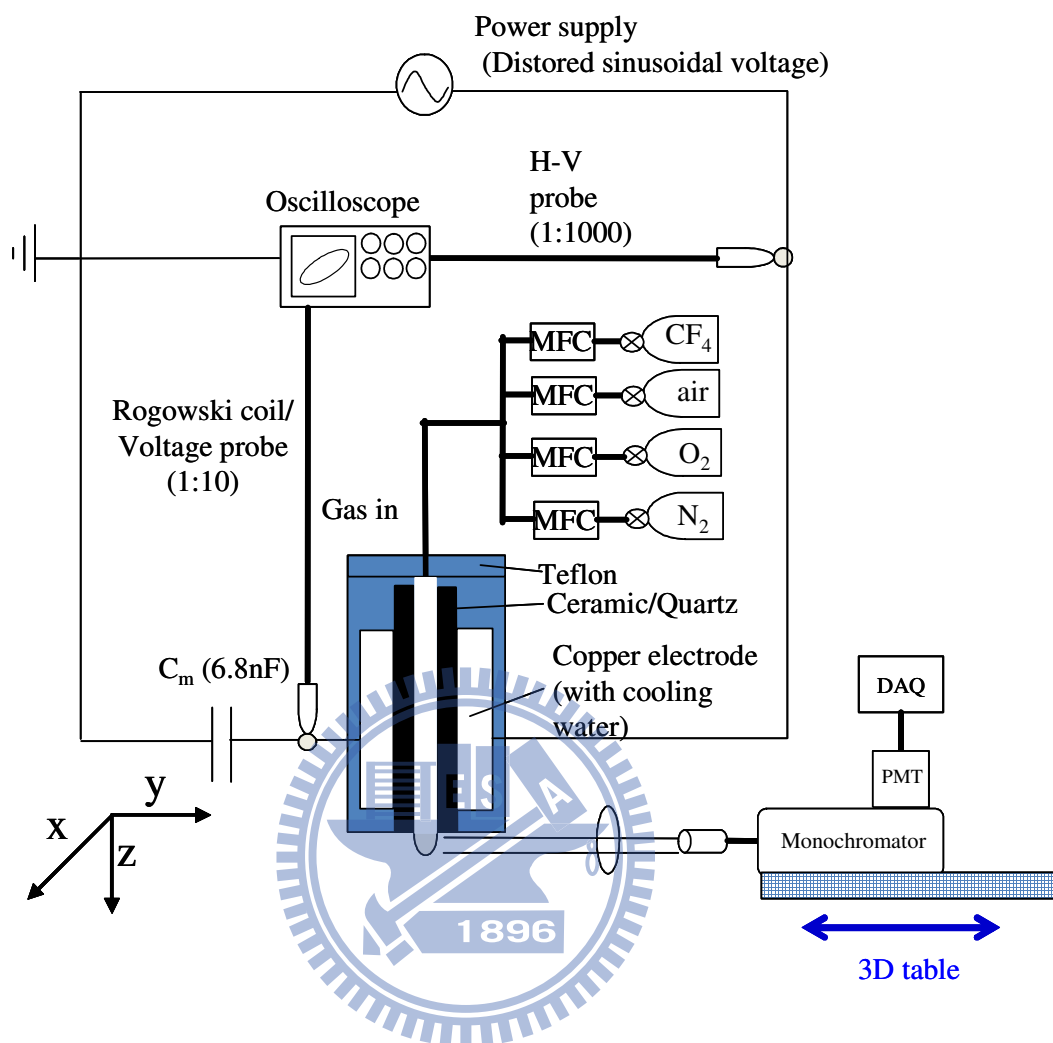
Fig. 2-4 Schematic sketch of a planar DBD APPJ with OES measurement.
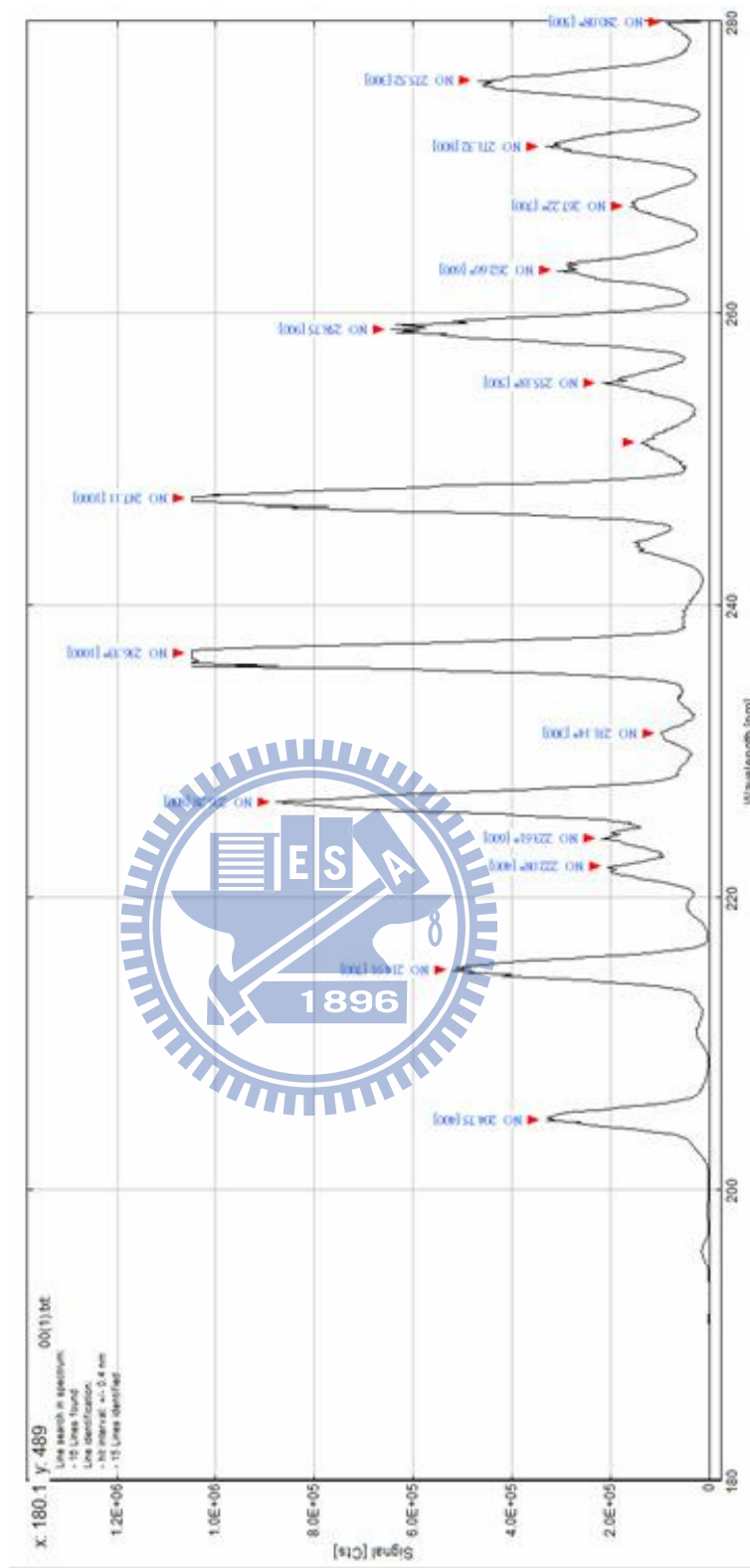
Fig. 2-5 Line identification of O$_2$/N$_2$ DBD plasma OES spectrum (180-280 nm).

The chart contains the following annotations:

exp
sim (360 K)

*Gas: N_2
 Flow rate: 50 (slm)
 Frequency: 60 (kHz)
 Dischage gap: 1 (mm)
 Dielectric: Quartz 1 (mm)
 Specrum: NO-r
 $\Delta\lambda$=0.01 nm
 Position: Discharge

Intensity (a.u.)

λ (μm)
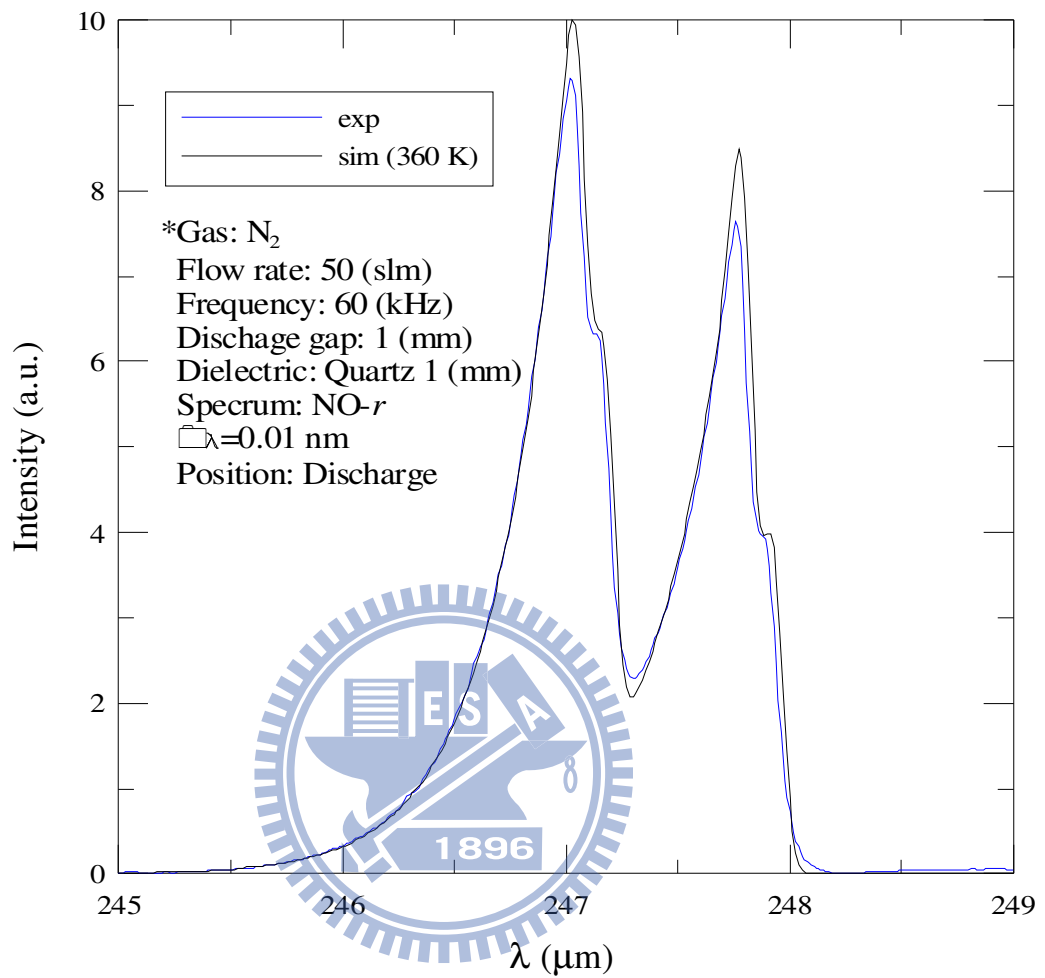
Fig. 2-6 Observed and simulation emission spectra of NO-γ. The gas temperature in the calculated spectrum was 360 K ($\Delta\lambda$=0.01 nm, output power from power supply= 500W).
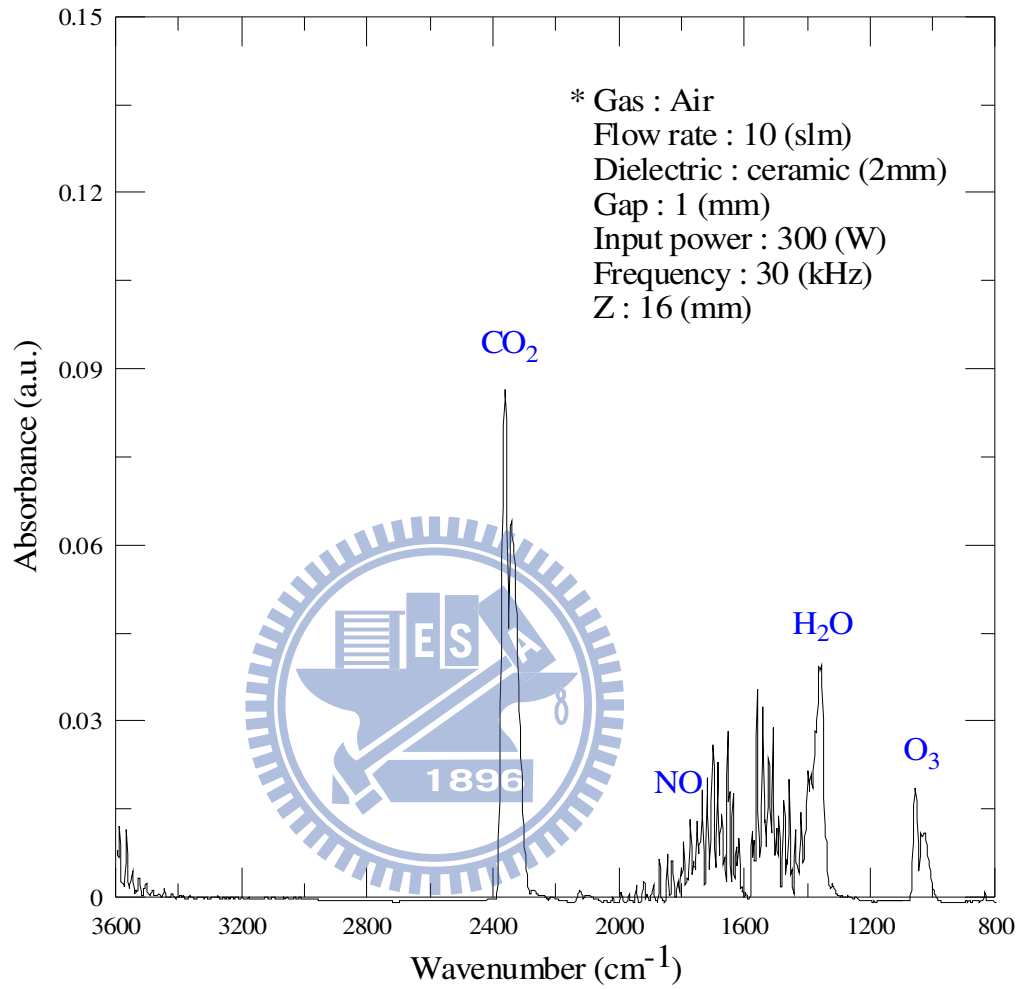
Fig. 2-7 Air DBD plasma infrared spectrum in 800-3600 cm^{-1} (air plasma) (output power

from power supply=300 W).
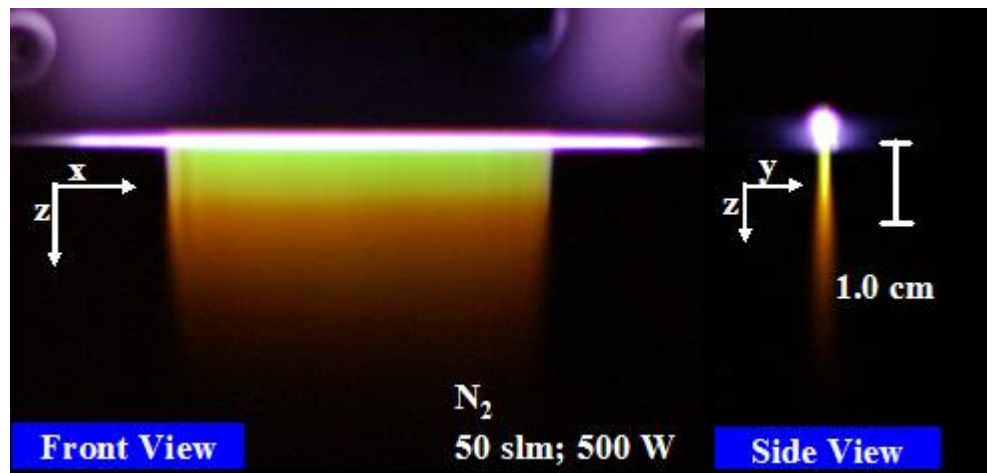
(a)
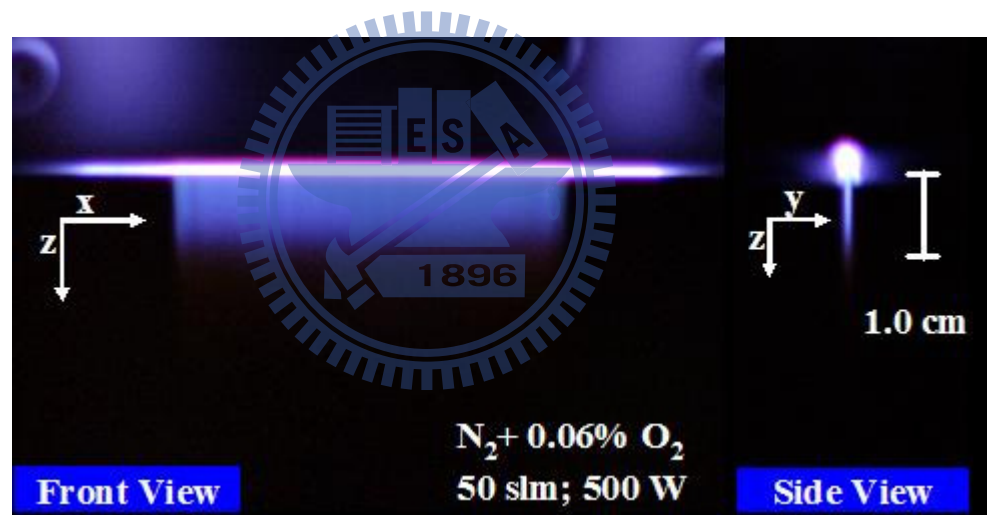
(b)

Fig. 3-1 Images of post-discharge region of APPJ with discharge gases consisting of (a) N_2, and (b) N_2+0.06% O_2 (output power from power supply=500 W).
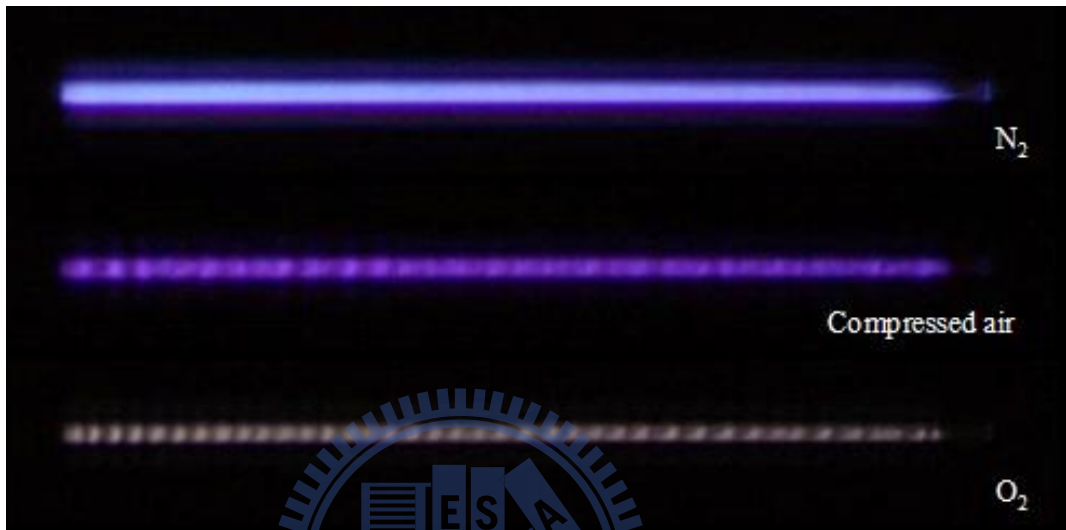
Fig. 3-2 Bottom view of discharge region for N_2, compressed air and O_2 discharges. Other discharge parameters: gas flow rate=10 slm; output power from power supply=300 W; and gap=1 mm.
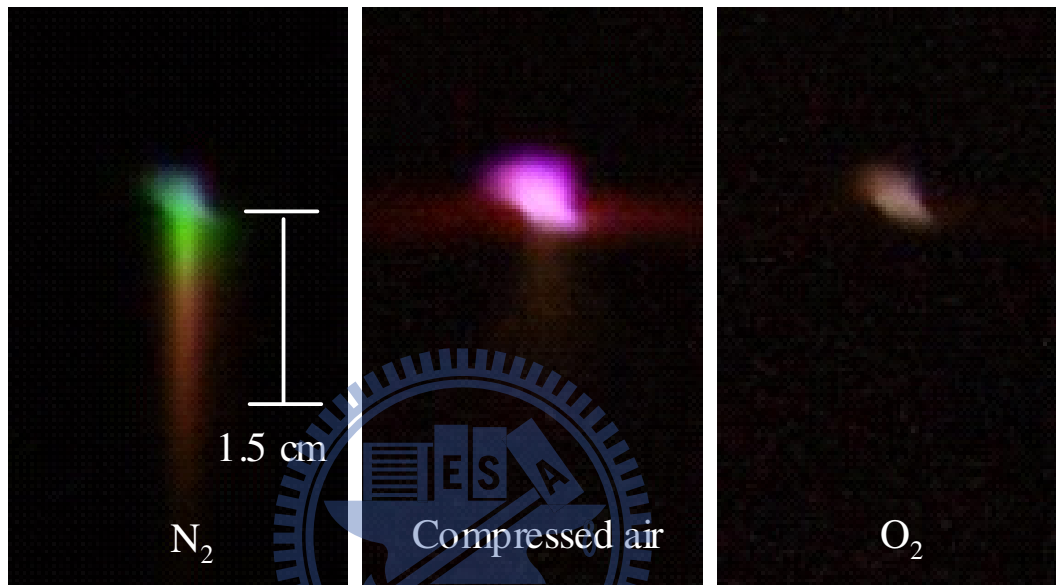
Fig. 3-3 Side view of post-discharge region for N_2, compressed air and O_2 discharges.

Other discharge parameters: gas flow rate=10 slm; output power from power supply=300

W; and gap=1 mm.
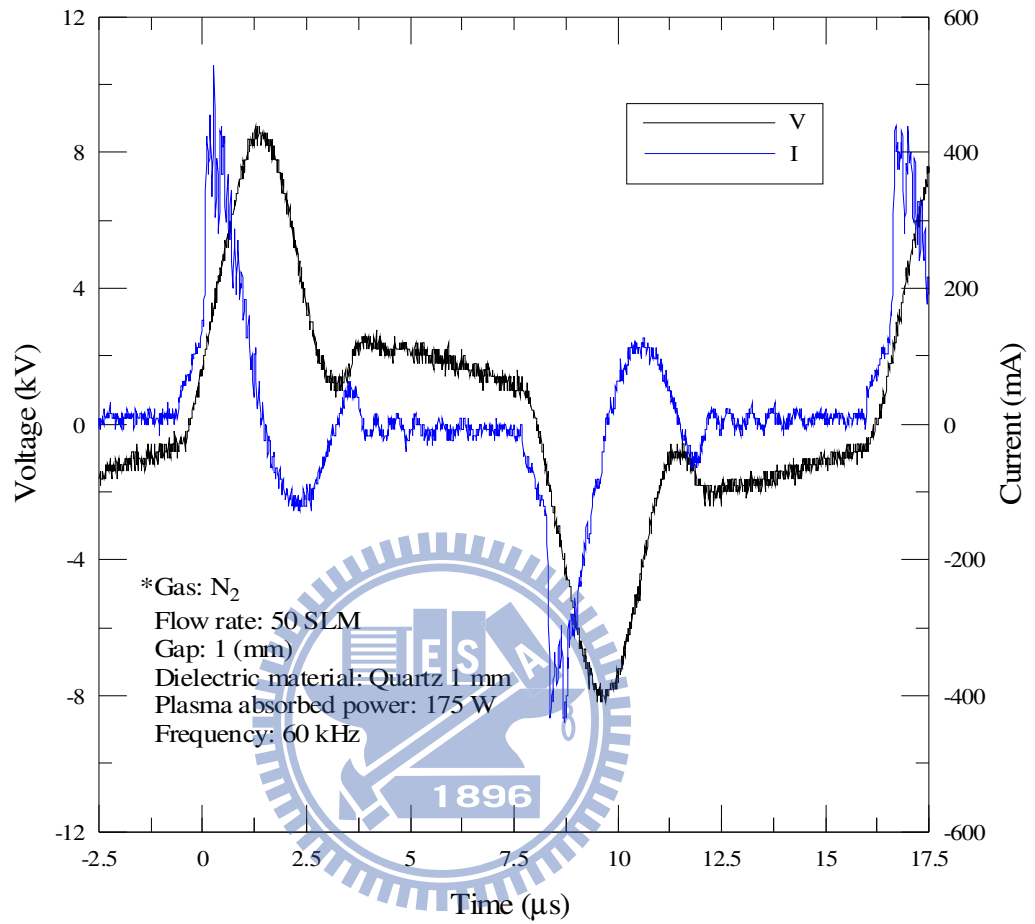
Fig. 3-4 Typical current and voltage waveforms for N_2 discharge (60 kHz).

(a)

(b)

104
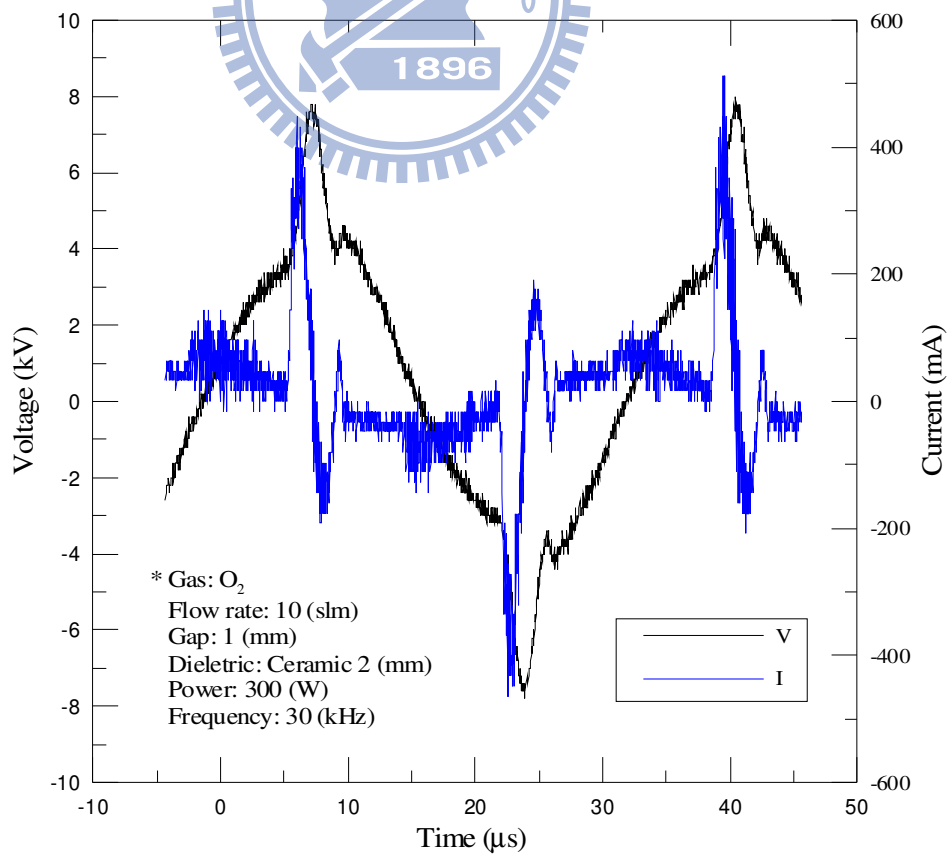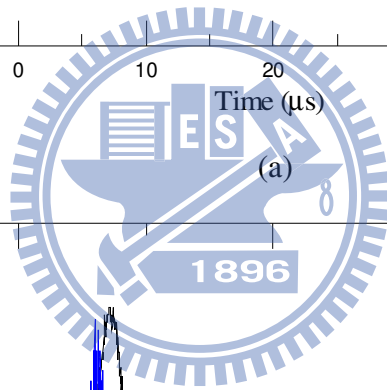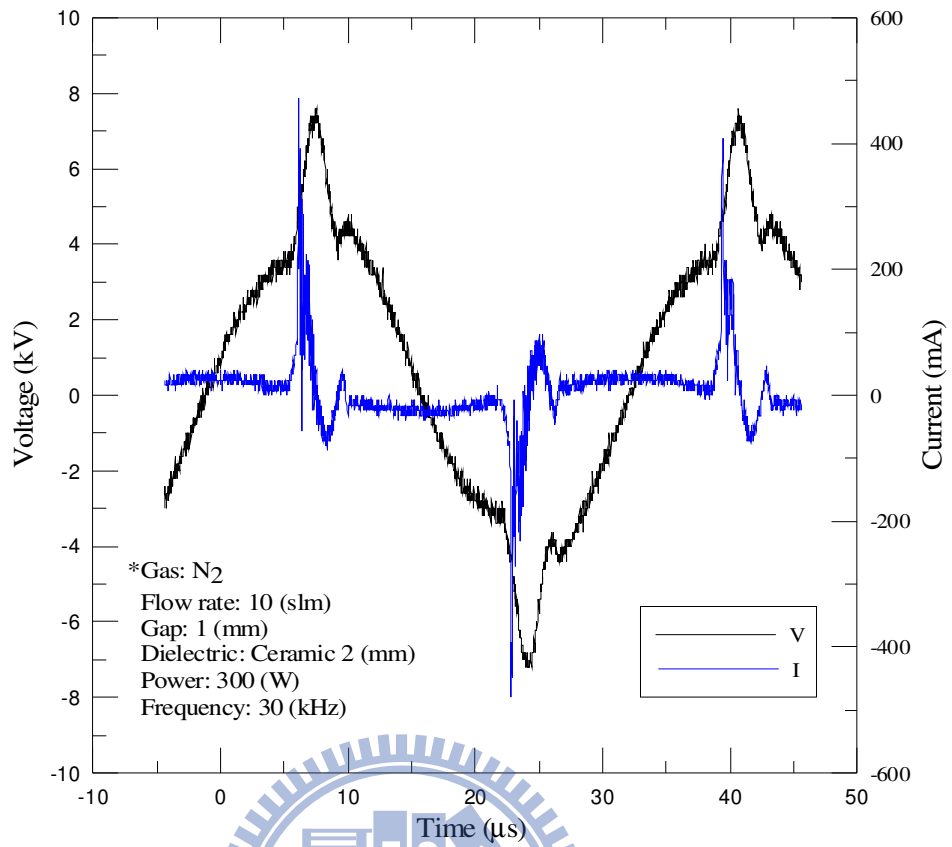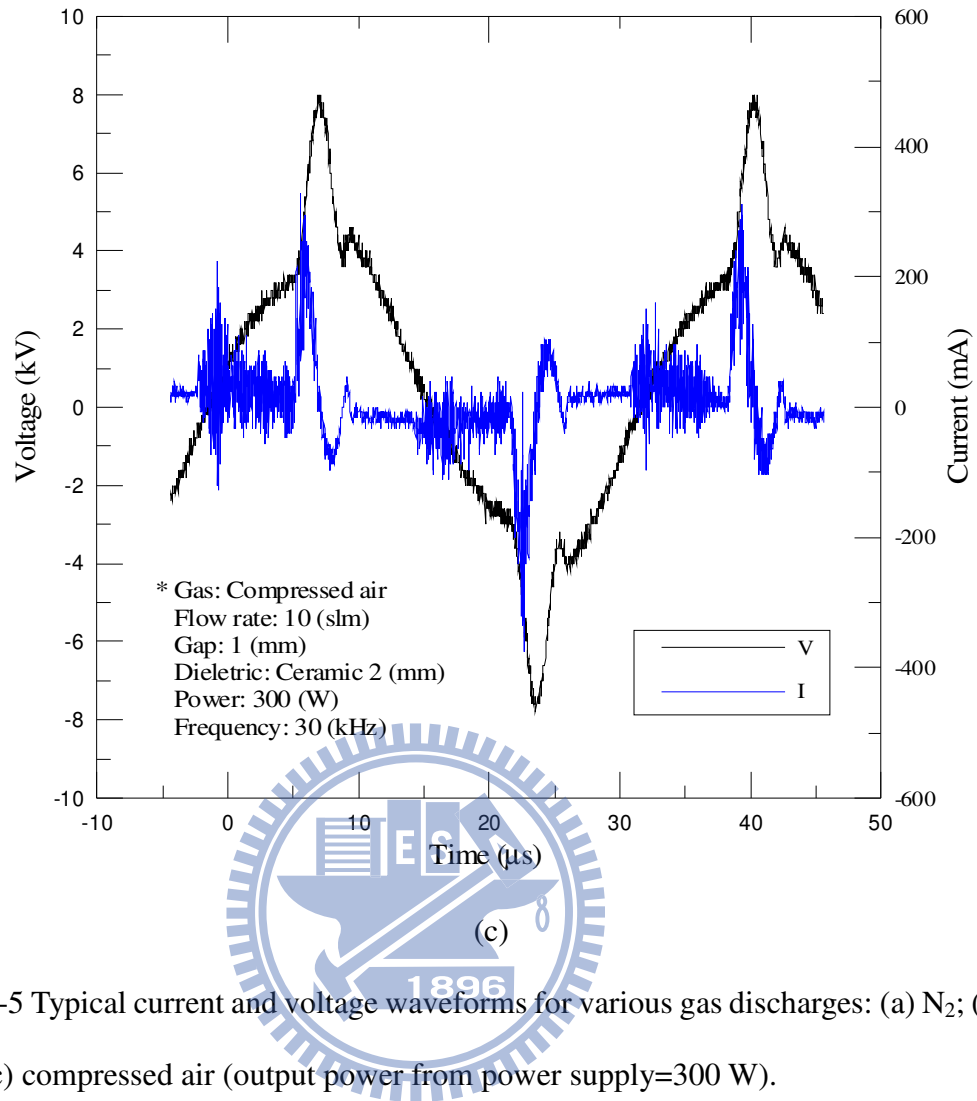
Fig. 3-5 Typical current and voltage waveforms for various gas discharges: (a) N_2; (b) O_2; and (c) compressed air (output power from power supply=300 W).
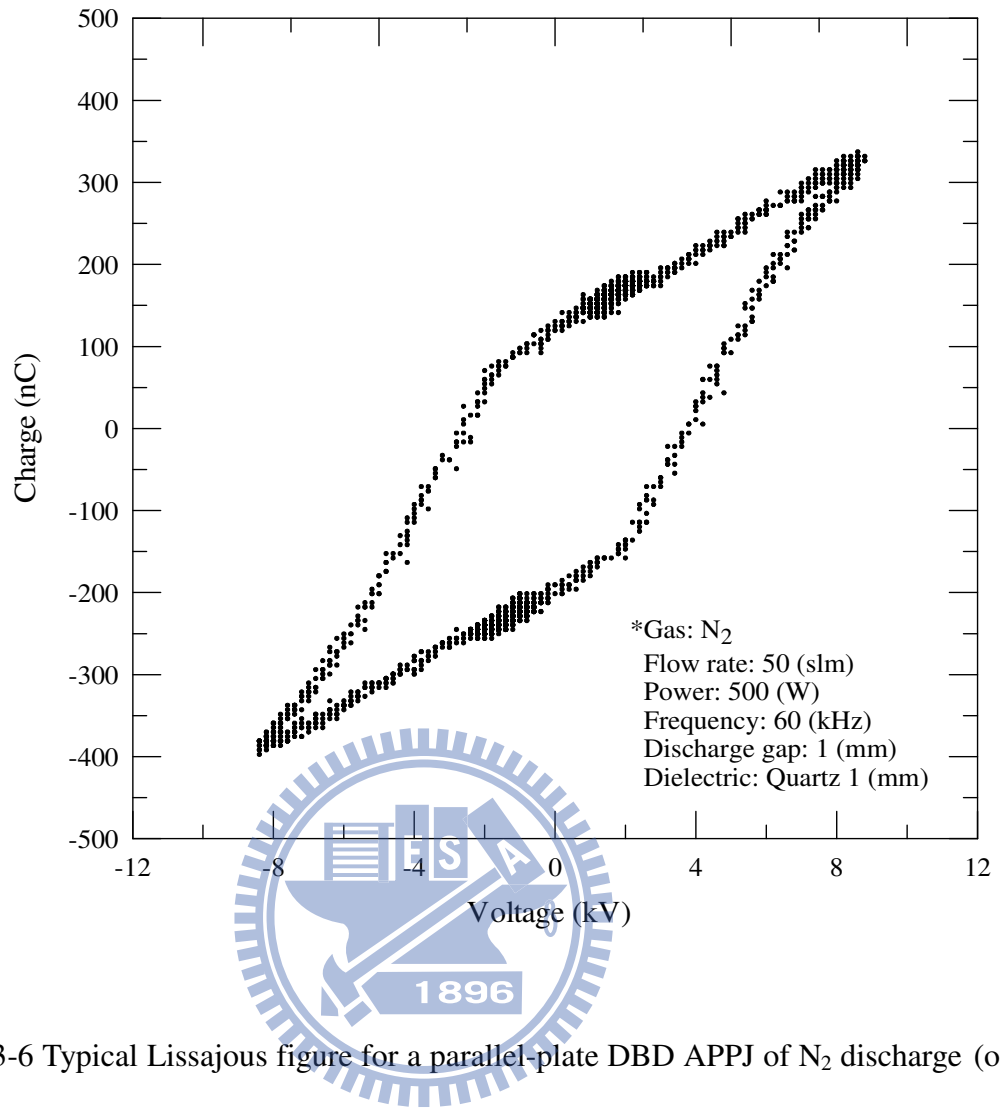
Fig. 3-6 Typical Lissajous figure for a parallel-plate DBD APPJ of N_2 discharge (output power from power supply=500 W).

*Gas: N$_2$
Flow rate: 10 (slm)
Gap: 1 (mm)
Dielectric: Ceramic 2 (mm)
Power: 300 (W)
Frequency: 30 (kHz)

(a)

* Gas: O$_2$
Flow rate: 10 (slm)
Gap: 1 (mm)
Dielectric: Ceramic 2 (mm)
Power: 300 (W)
Frequency: 30 (kHz)
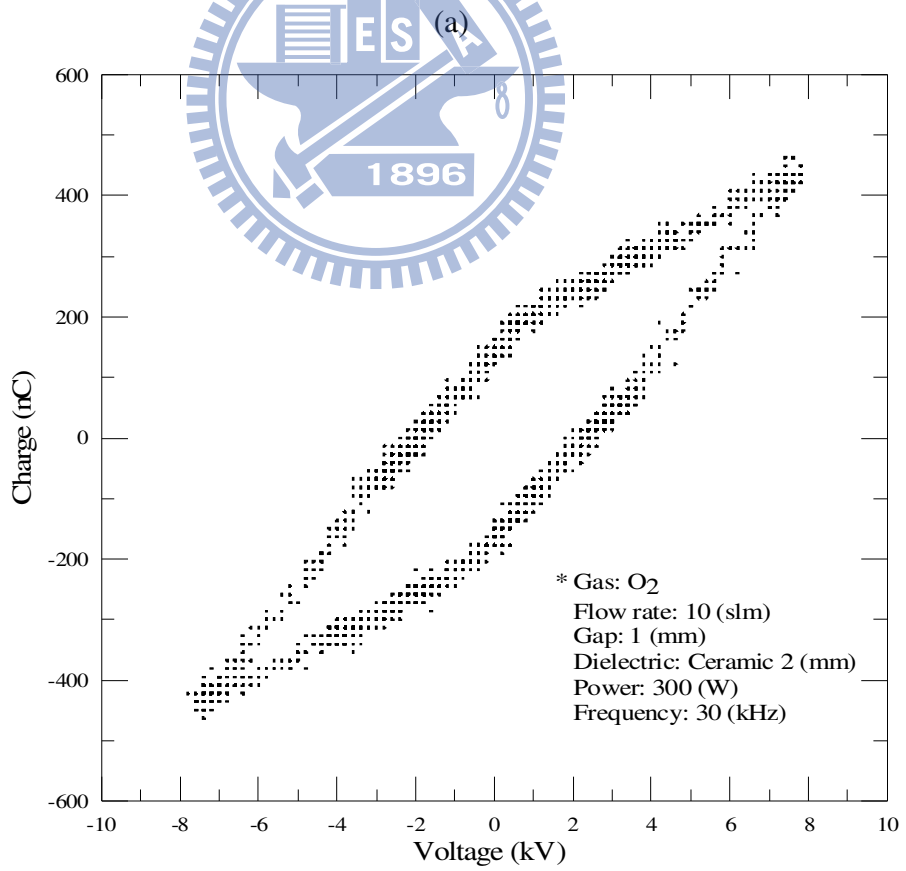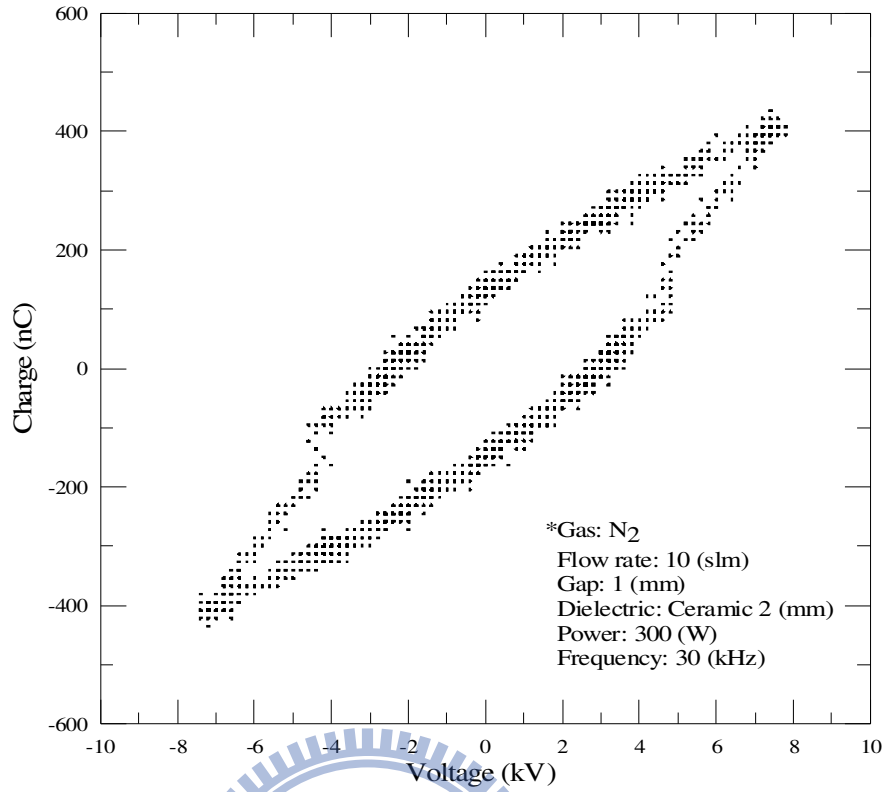
(b)
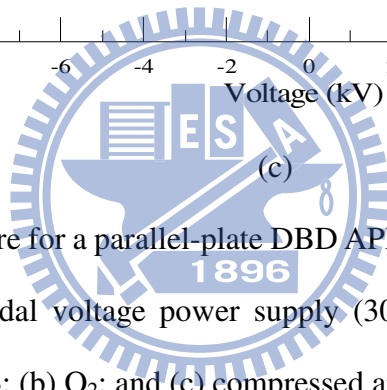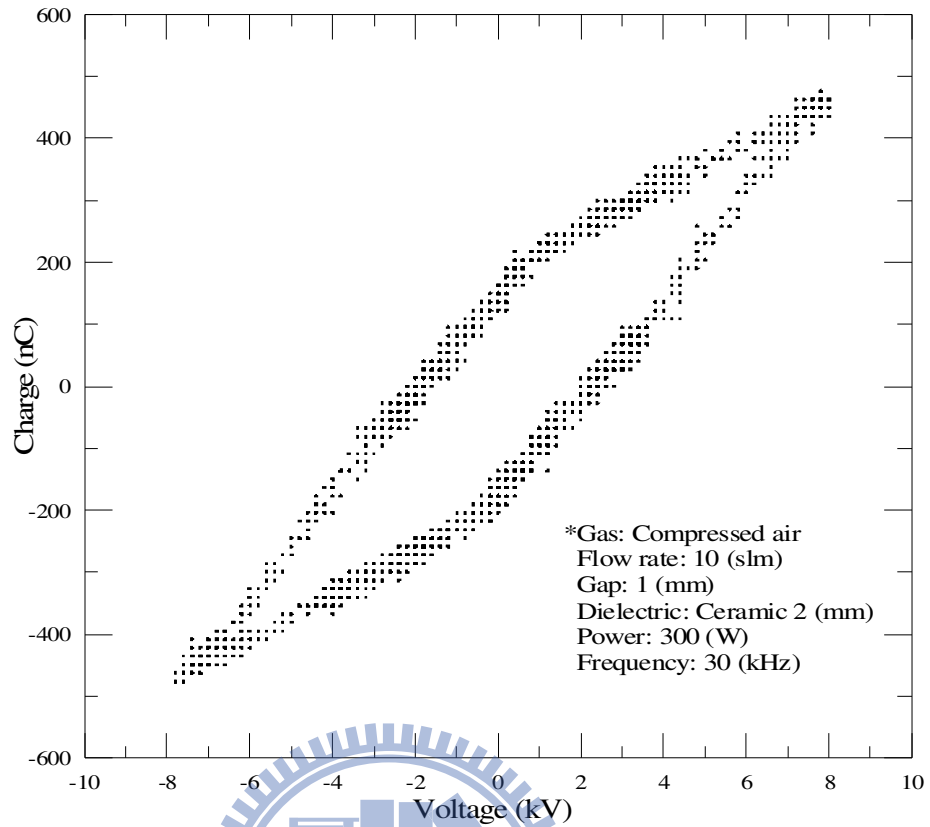
Fig. 3-7 Lissajous figure for a parallel-plate DBD APPJ for various gas discharges driven by a distorted sinusoidal voltage power supply (30 kHz, output power from power supply=300 W): (a) N$_2$; (b) O$_2$; and (c) compressed air.
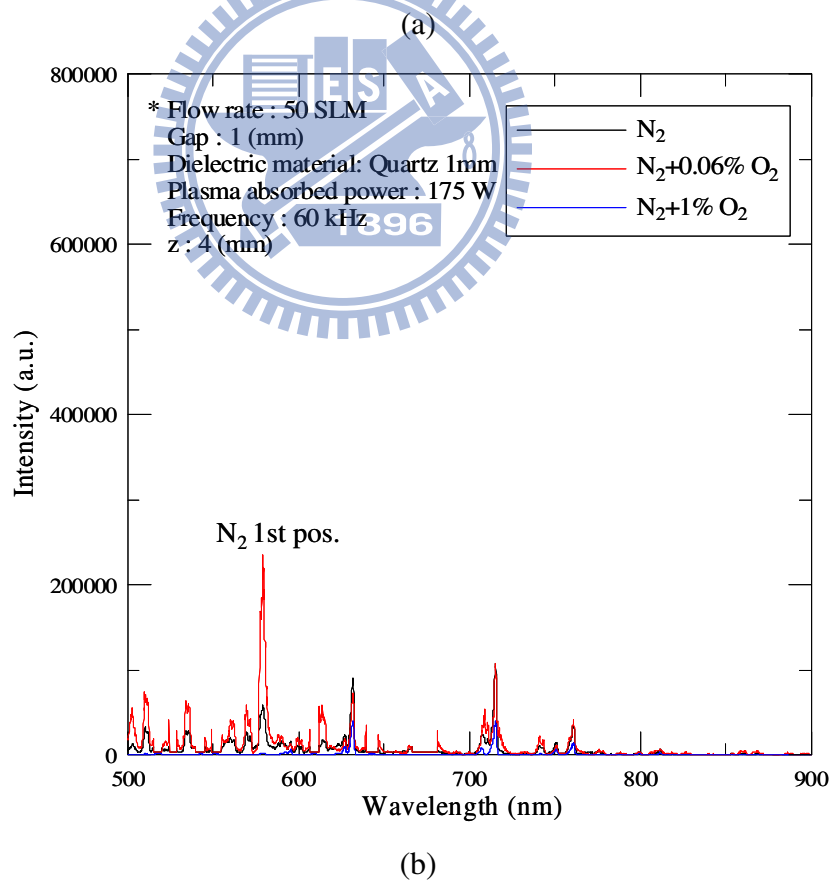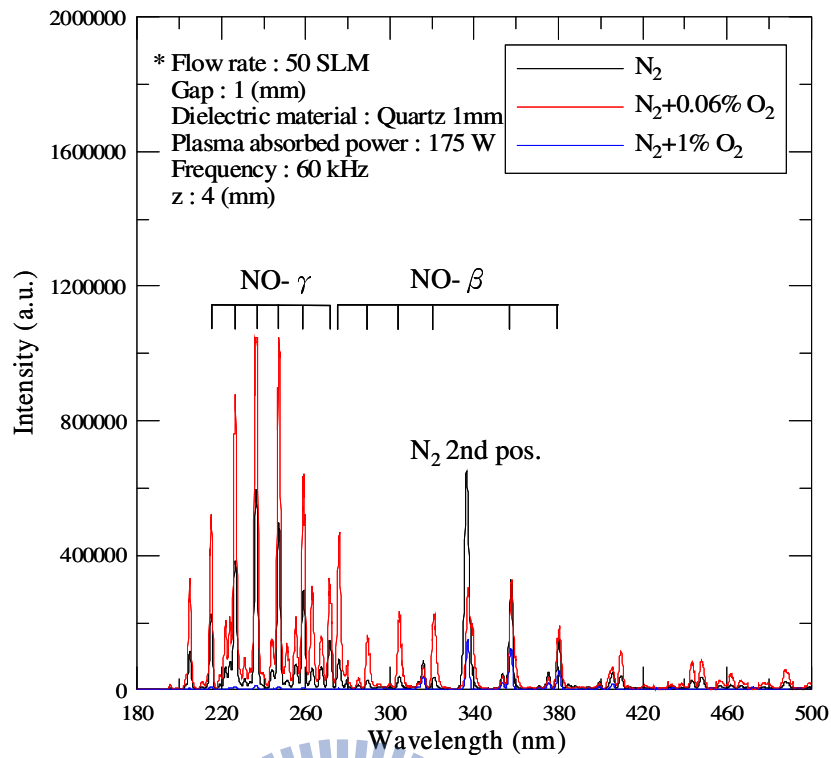
Fig. 3-8 Optical emission spectra in (a) 180-500 nm; and (b) 500-900 nm for post-discharge plasma (60 kHz, 50 SLM)
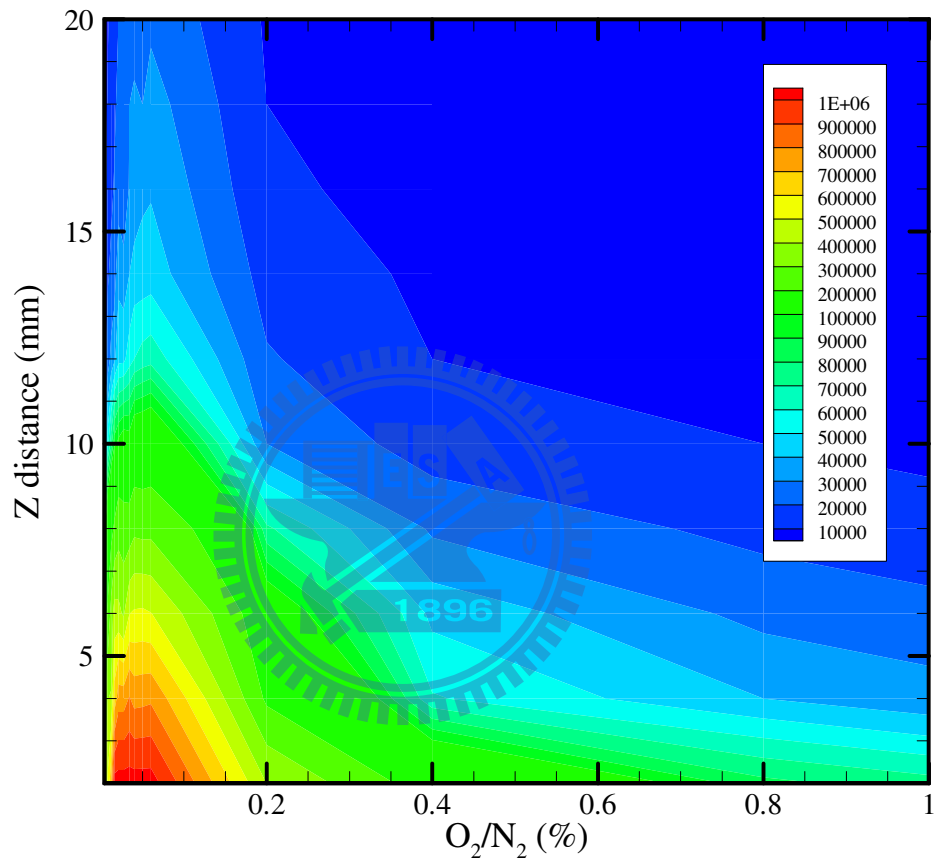
Fig. 3-9 Distributions of typical NO-γ UV emission intensity (236.6 nm, photon energy: 5.2 eV) as functions of downstream distance and O_2/N_2 (%) in post-discharge region (60 kHz, 50 SLM, output power from power supply=500 W)
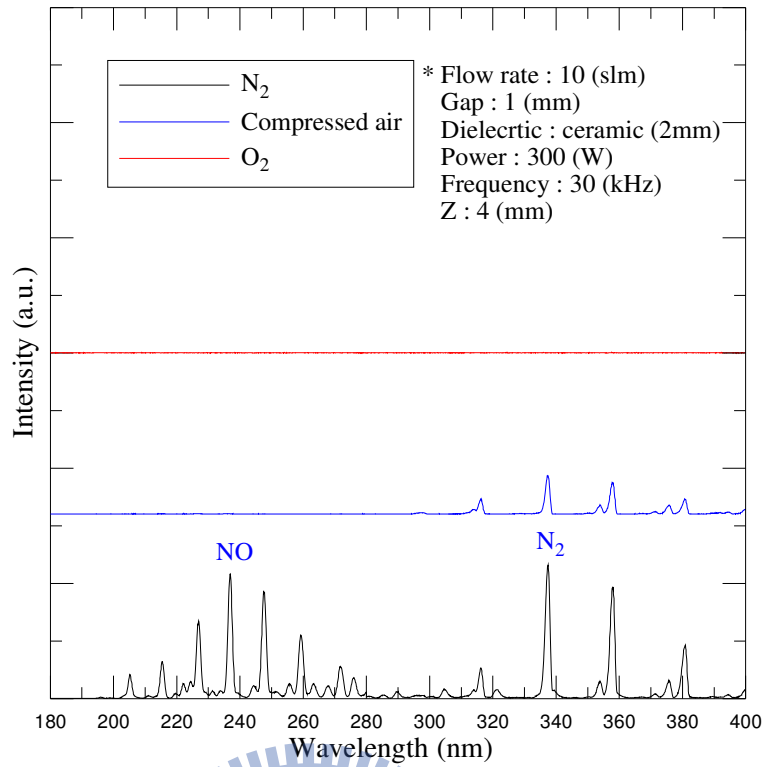
(a)
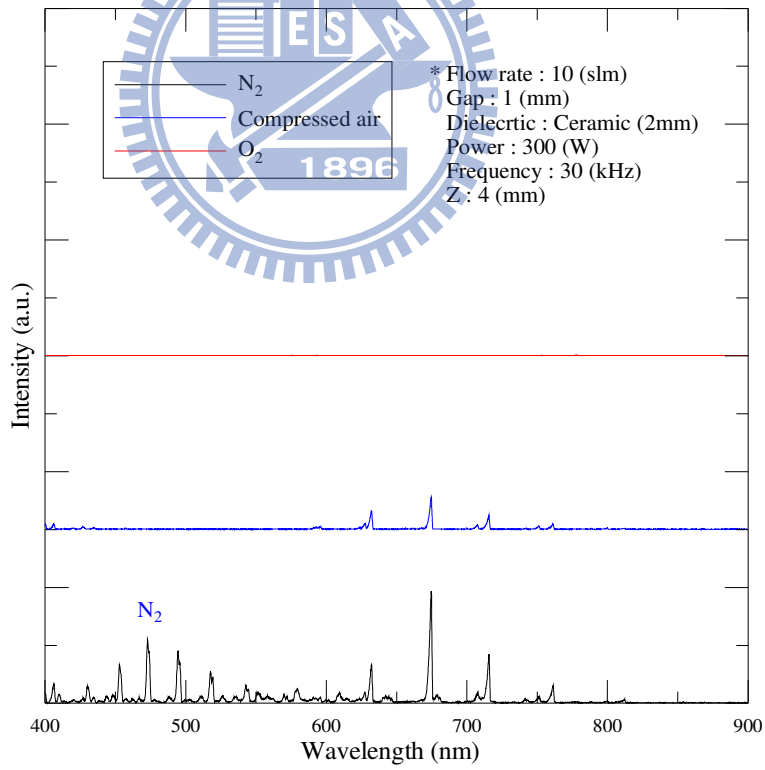
(b)

Fig. 3-10 Optical emission spectrum in the (a) UV and (b) VIS regions for the post-discharge plasma (output power from power supply=300 W).
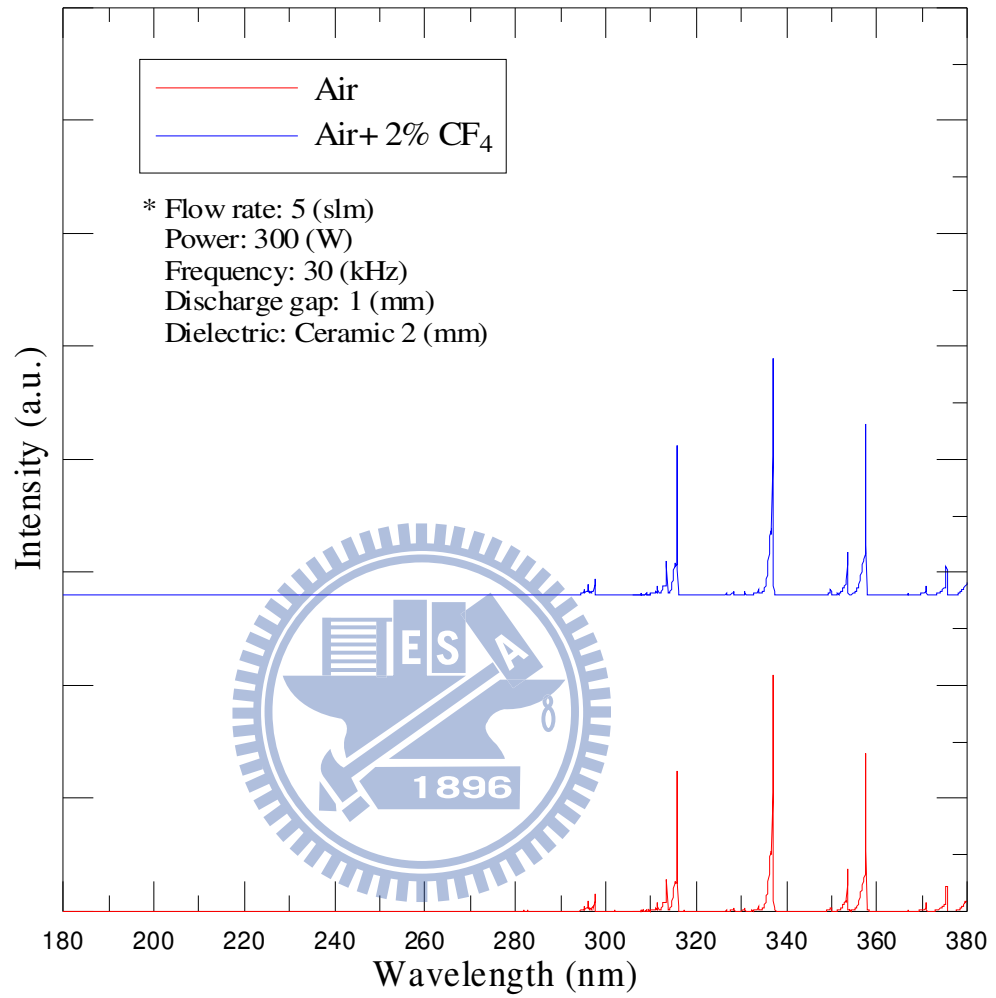
Fig. 3-11 Optical emission spectrum in 180-380 nm for the discharge plasma (output power from power supply=300 W).
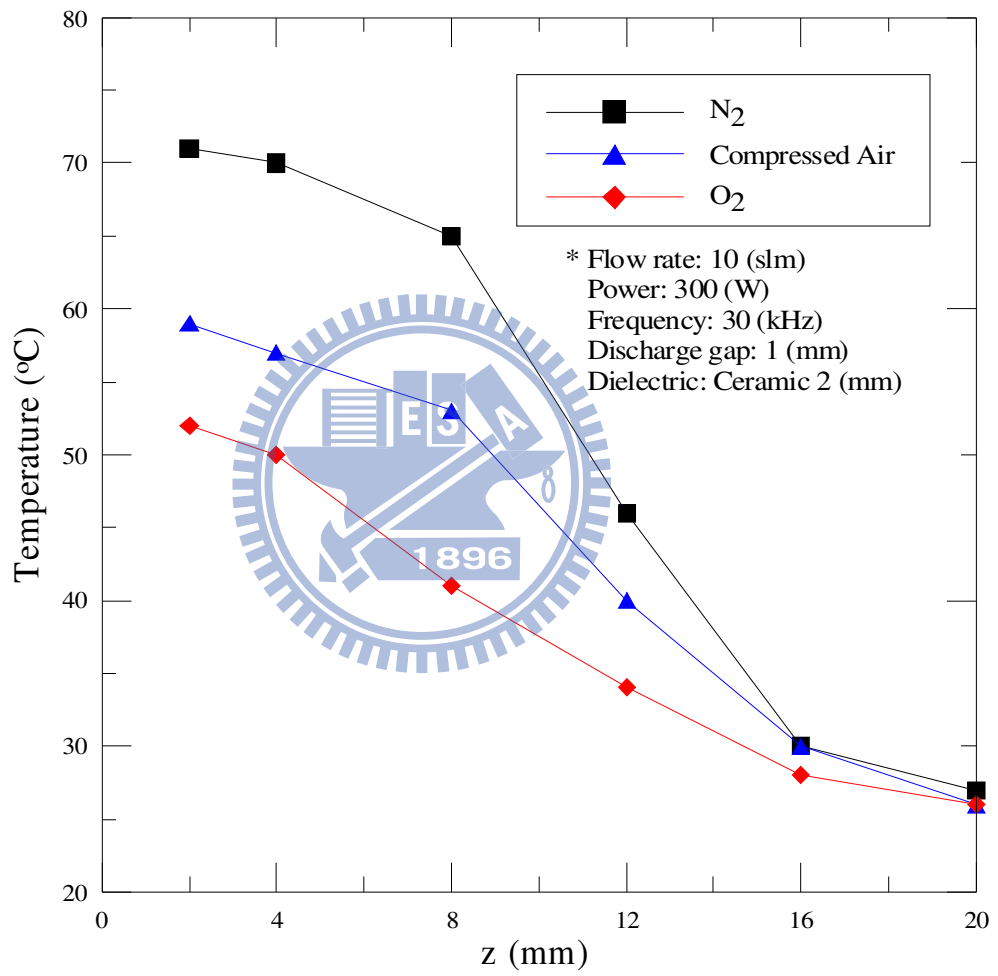
Fig. 3-12 Temperature distributions in the post-discharge jet region of N_2, compressed air and O_2 discharges (output power from power supply=300 W).
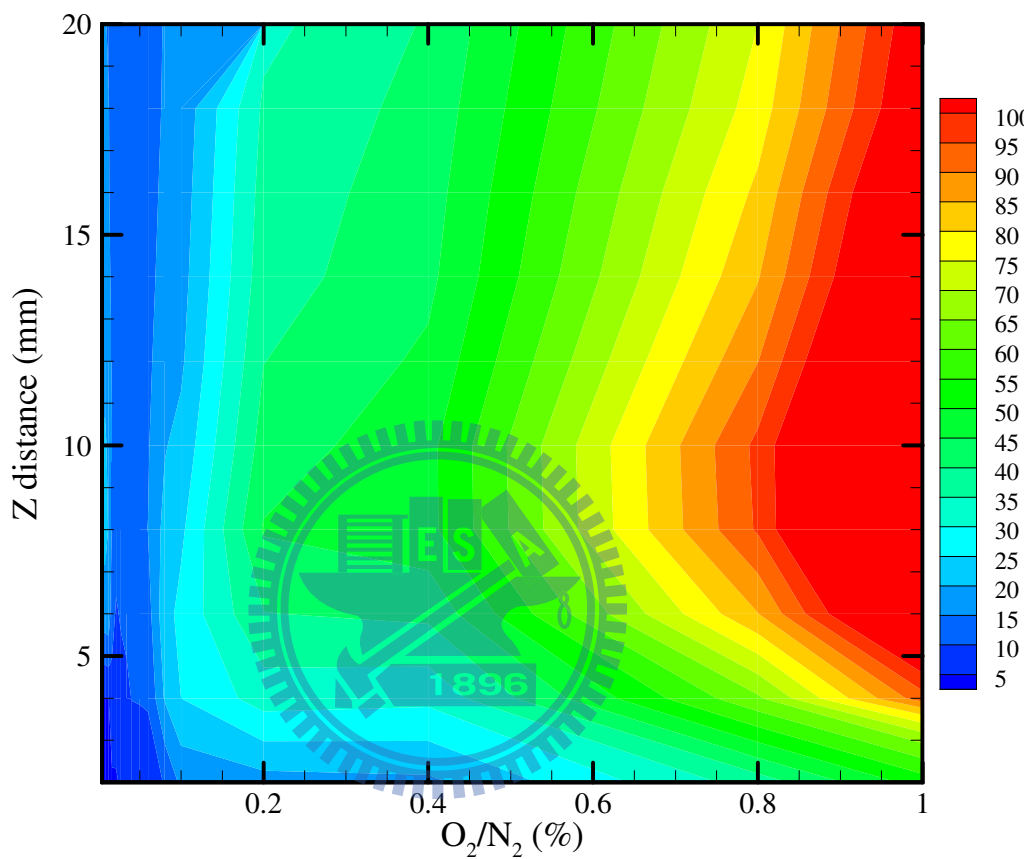
Fig. 3-13 Distributions of O_3 concentration (ppm) as functions of downstream distance and O_2/N_2 (%) in post-discharge region (60 kHz, 50 SLM, output power from power supply=500 W).
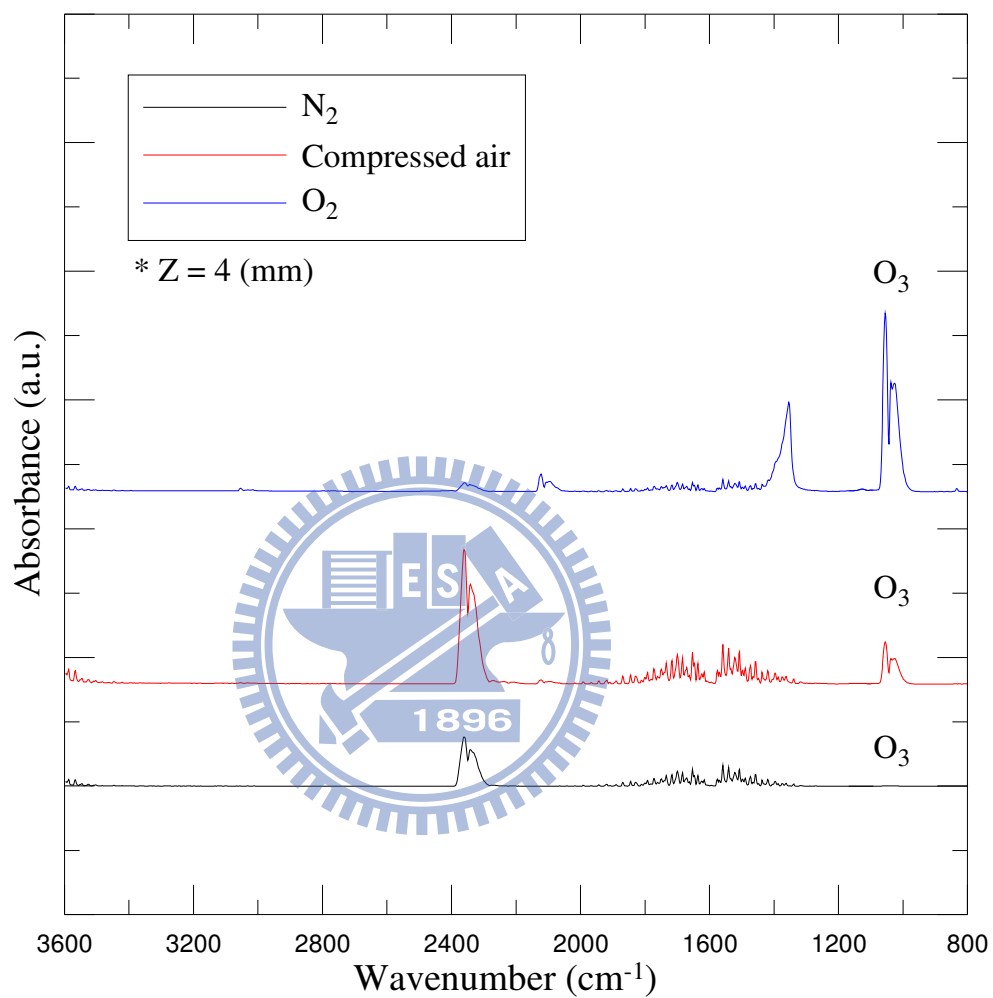
Fig. 3-14 Infrared spectra of post-discharge region for N_2, compressed air, and O_2 discharges in the 800-3600 cm^{-1} (30 kHz, 10 SLM, output power from power supply=300 W).
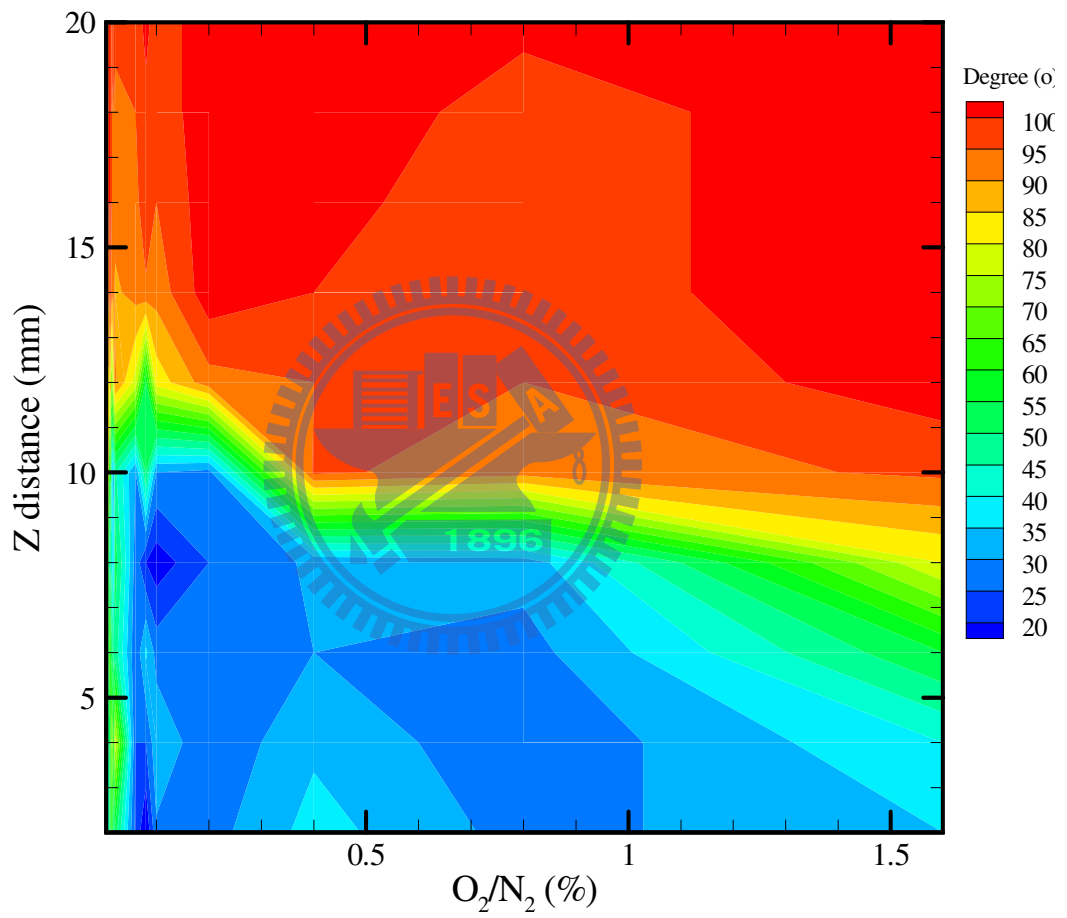
Fig. 4-1 Distribution of measured contact angles as a function of downstream distance
and ratio of O_2/N_2 (%) (60 kHz, 50 SLM, output power from power supply=500 W).
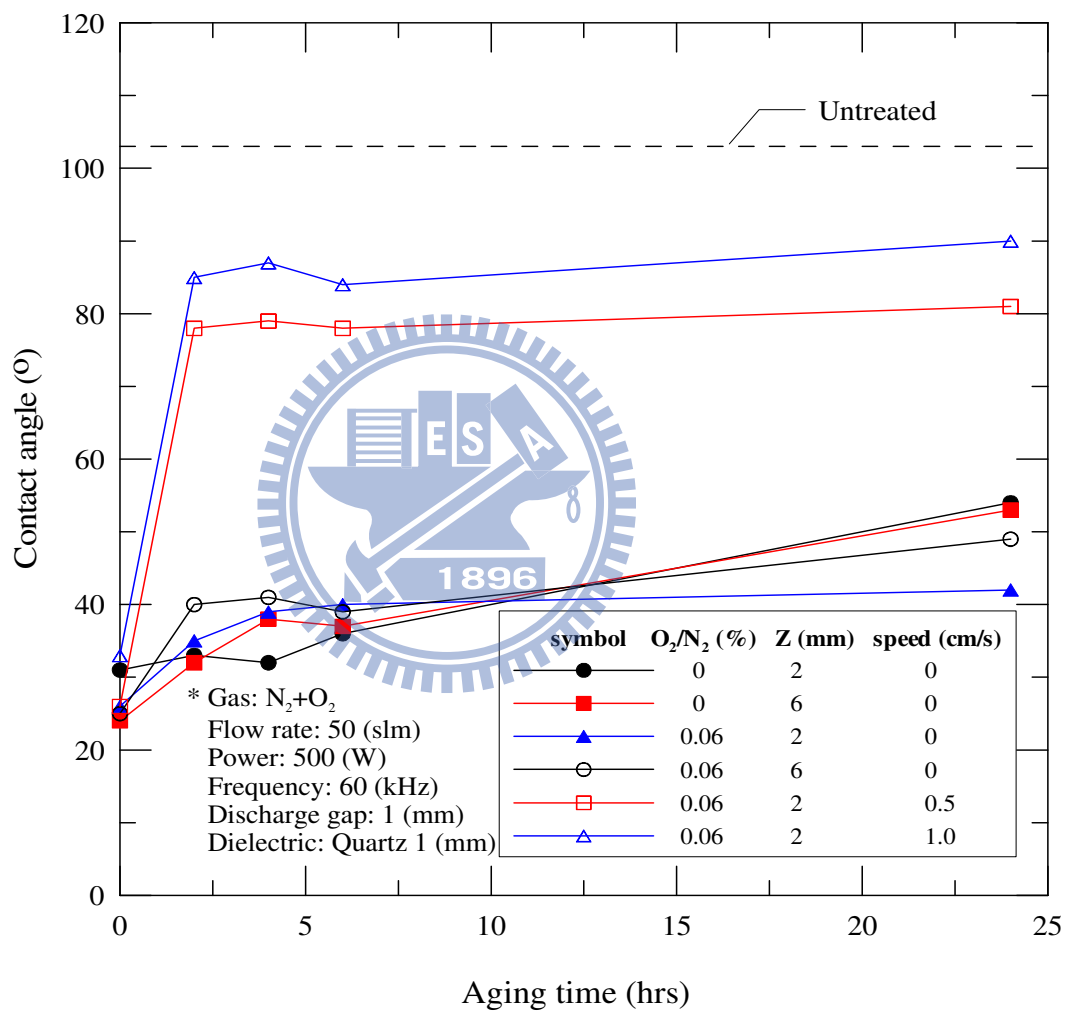
Fig. 4-2 Contact angle of water on PP film versus various gases, Z-directions and aging times treated in the N_2+O_2 DBD environment (output power from power supply=500 W).
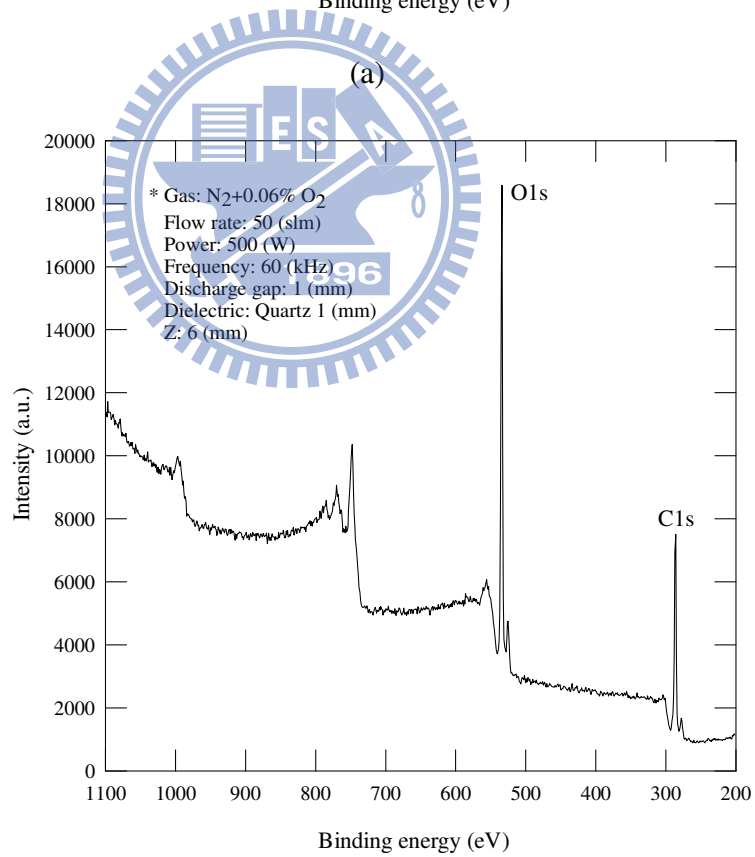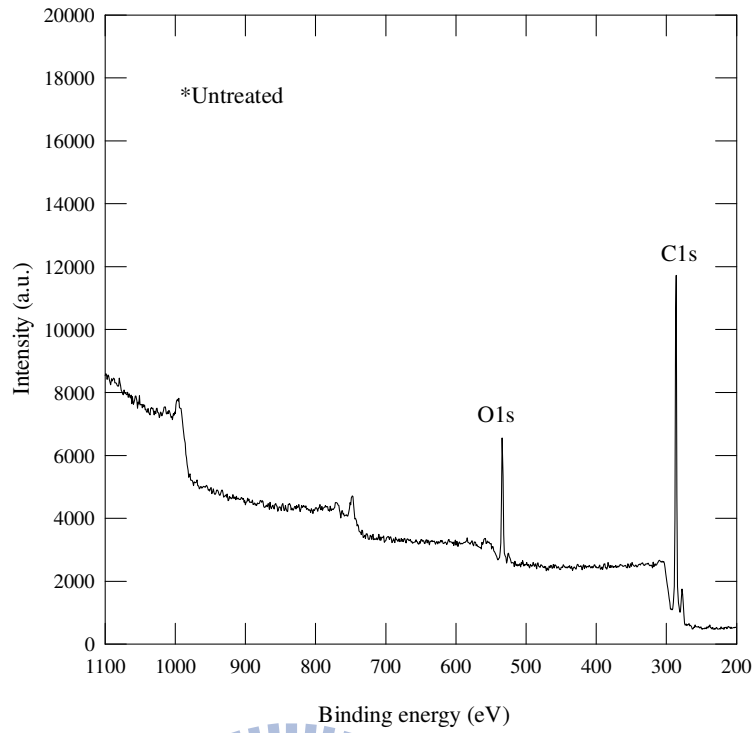
Fig. 4-3 XPS scan spectra of (a) untreated PP film and (b) $N_2+0.06\%$ O_2 treated PP at Z=

6 mm (output power from power supply=500 W).
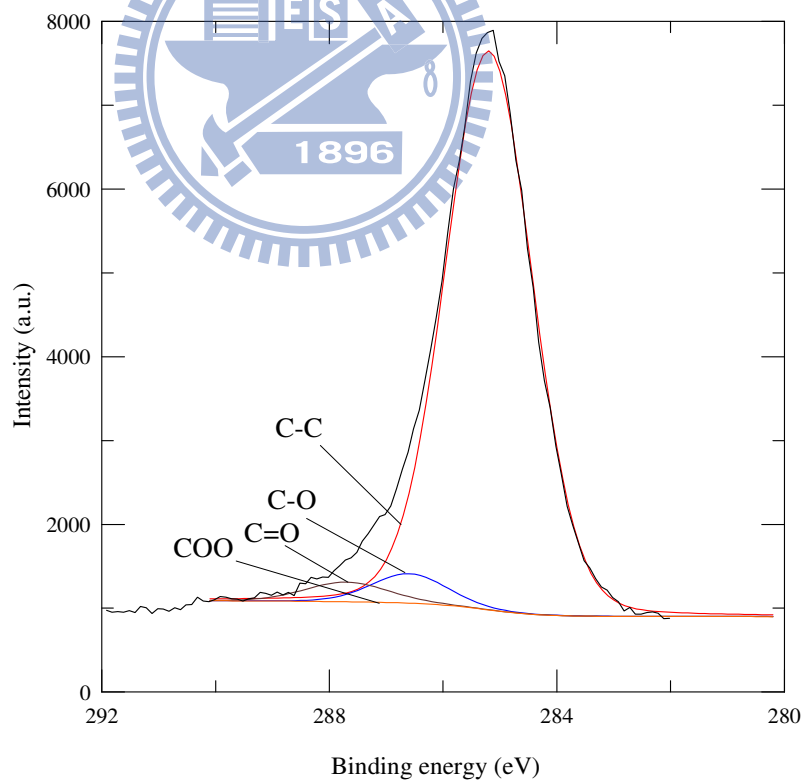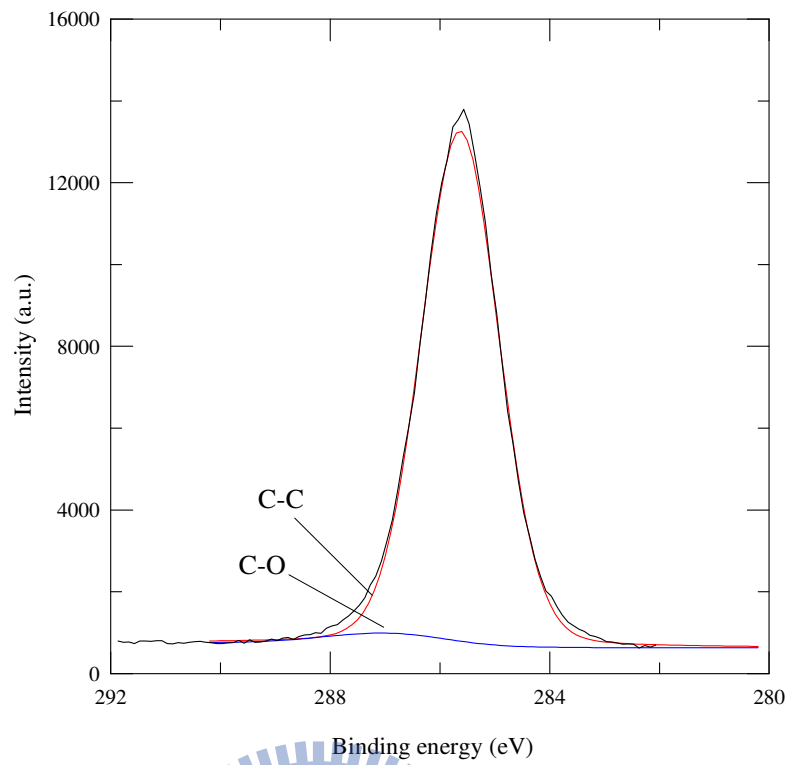
Fig. 4-4 C1s spectra of (a) untreated PP film and (b) N_2+0.06% O_2 treated PP at Z= 6 mm.
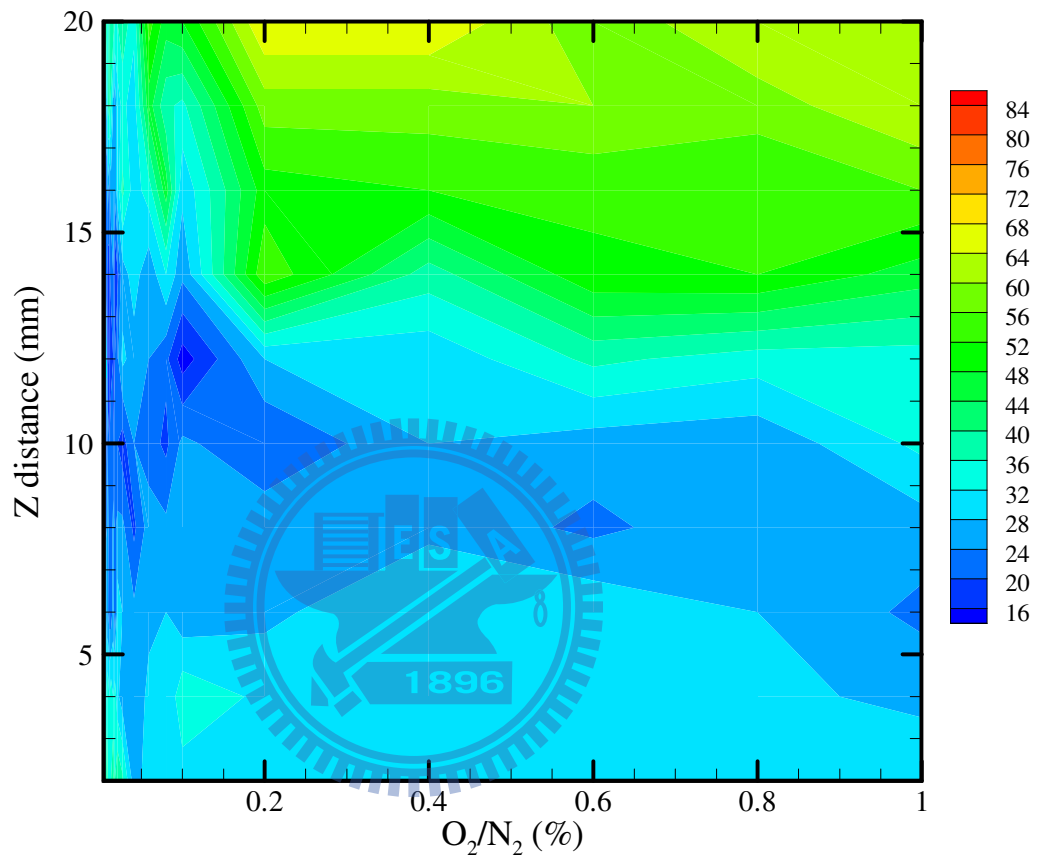
Fig. 5-1 Measured contact angle of ITO glass surface (stationary) as functions of z coordinate and O_2/N_2 (%) after 5 seconds of plasma jet treatment (60 kHz, 50 SLM, output power from power supply=500 W).

(a)
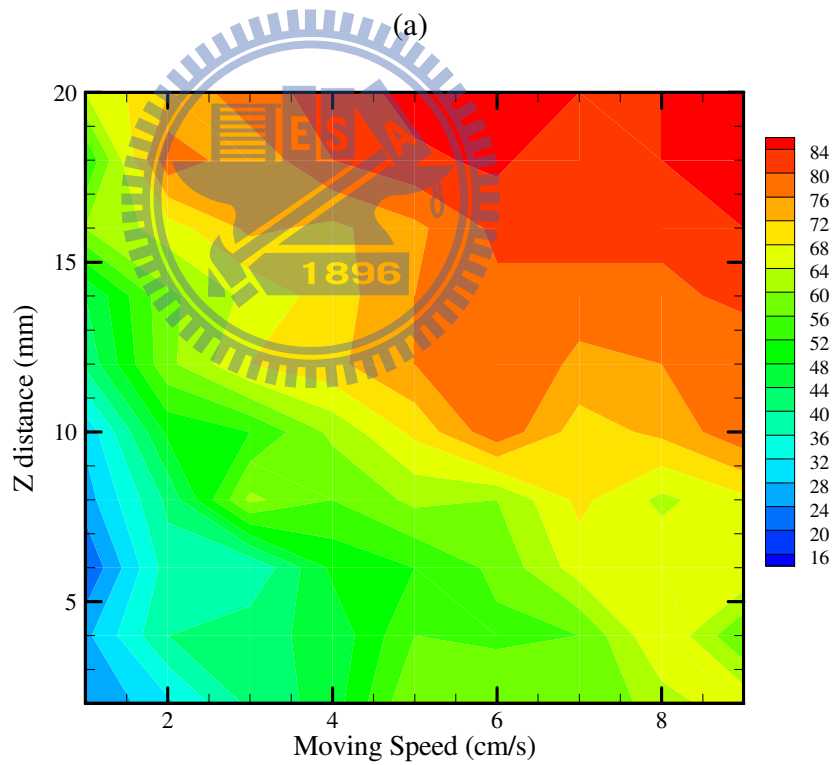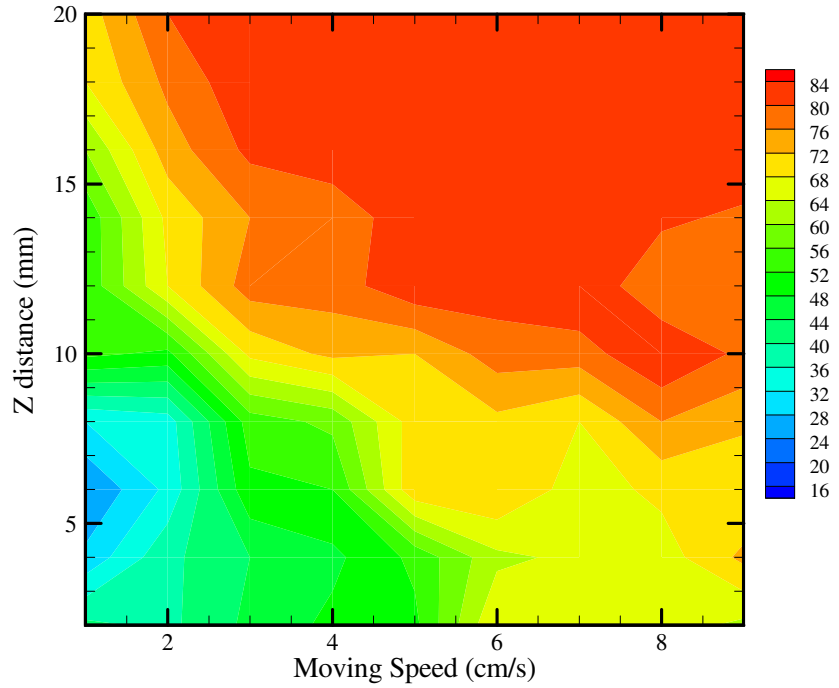
(b)

Fig. 5-2 Measured contact angle of ITO glass surface (non-stationary) as functions of z-coordinate and O_2/N_2 (%) after (a) pure N_2 and (b) 0.04 % O_2/N_2 plasma jet treatment (60 kHz, 50 SLM, absorbed power=175W).
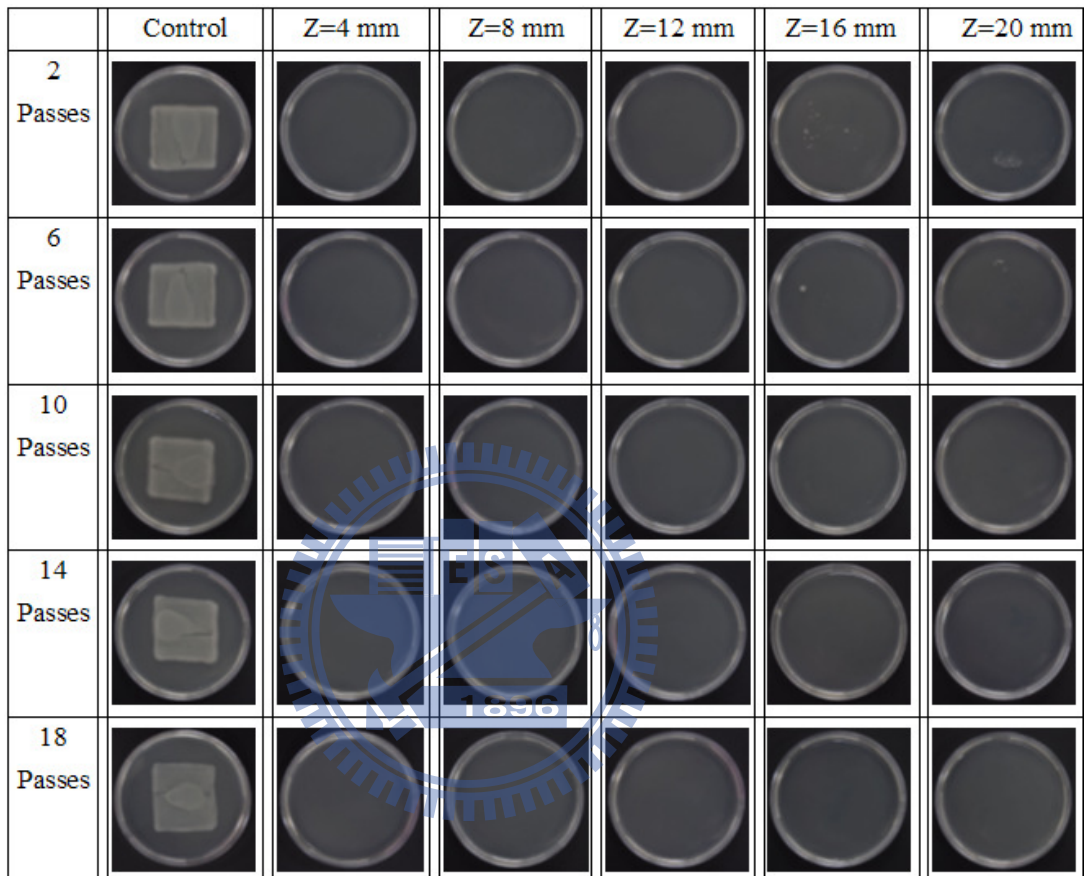
Fig. 6-1 Appearance of *E. coli* petri dishes after incubation with different exposure times with different exposure distances and times (number of passes) to compressed air plasma. Other discharge parameters: gas flow rate=10 slm, output power from power supply=300 W, and gap=1 mm.
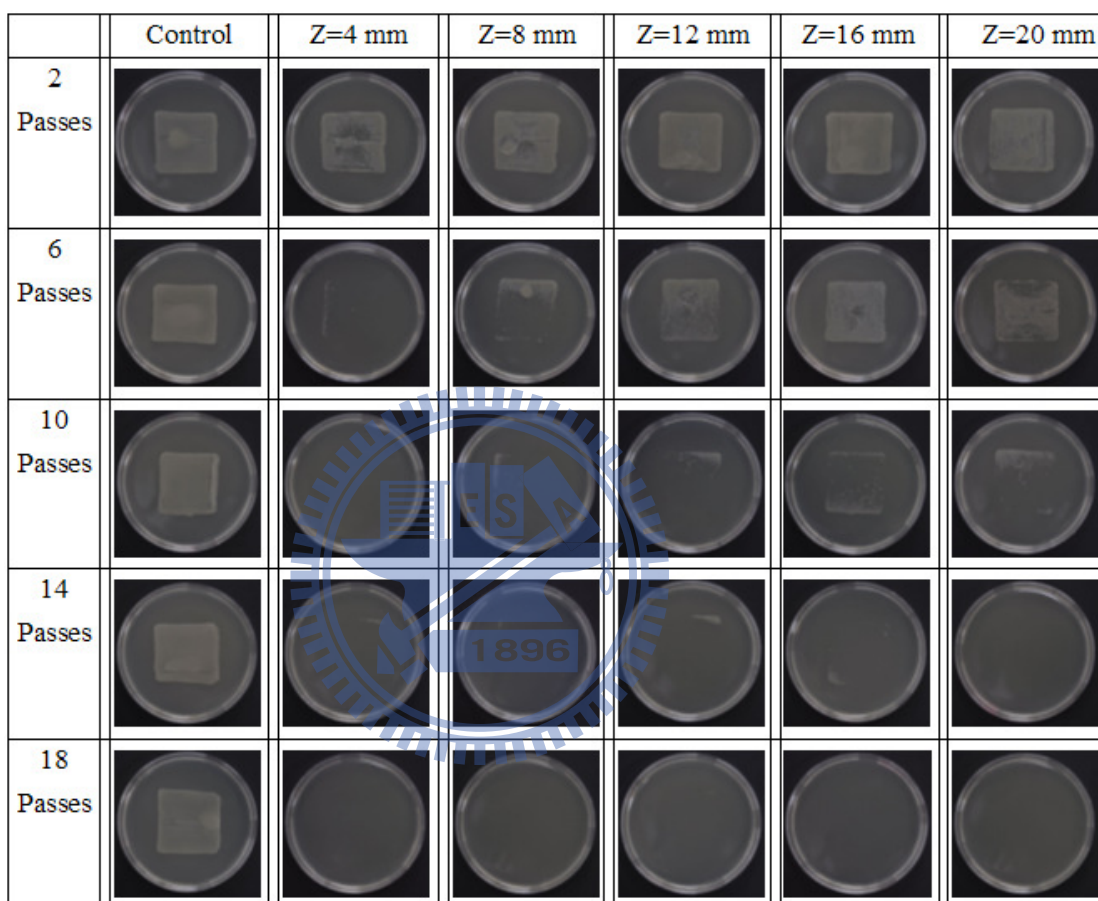
Fig. 6-2 Appearance of *B. subtilis* petri dishes after incubation with different exposure distances and times (number of passes) to compressed air plasma. Other discharge parameters: gas flow rate=10 slm, output power from power supply=300 W, and gap=1 mm.

(a)
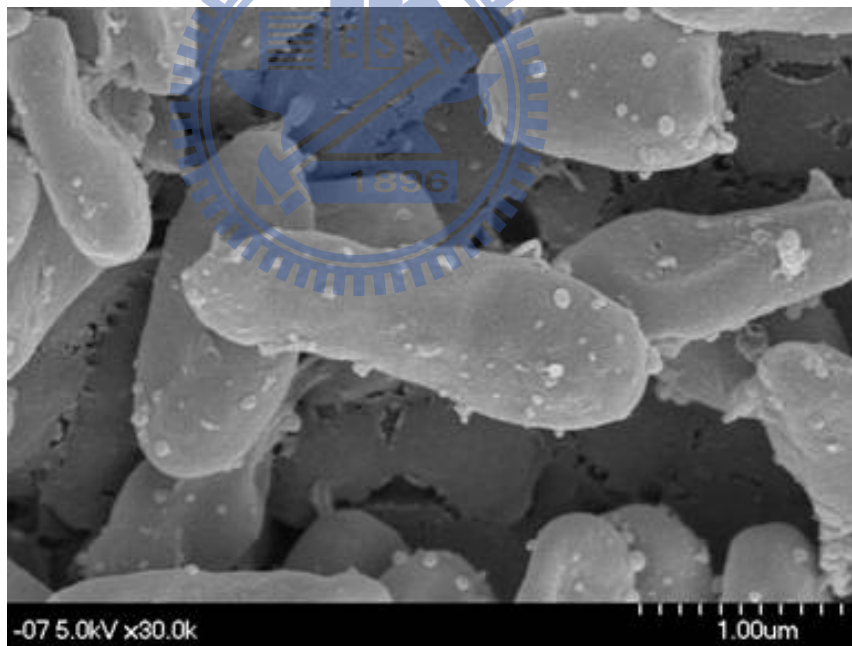
(b)

Fig. 6-3 SEM images of various microorganisms with a parallel-plate DBD APPJ using compressed air: (a) untreated *E. coli*; and (b) plasma-treated *E. coli*.
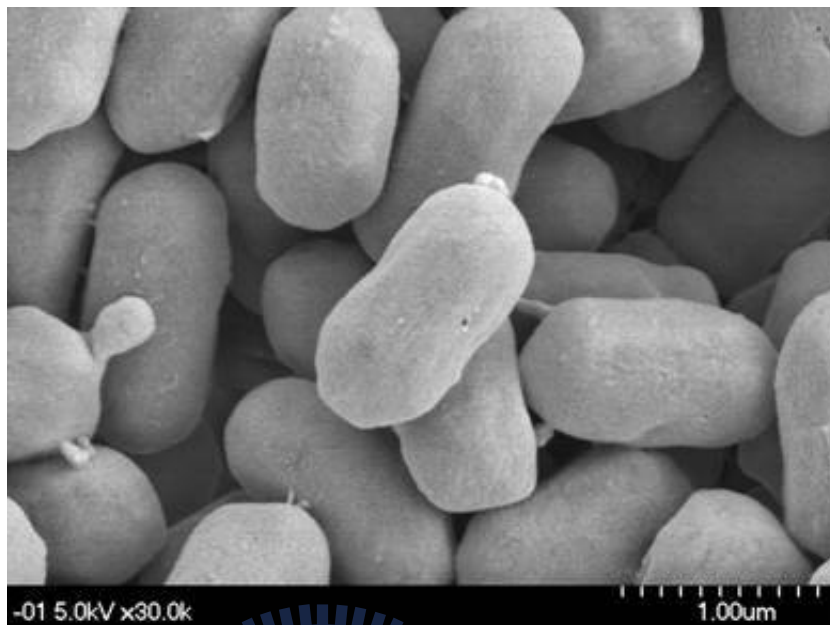
(a)

(b)

Fig. 6-4 SEM images of various microorganisms with a parallel-plate DBD APPJ using compressed air: (a) untreated *B. subtilis*; and (b) plasma-treated *B. subtilis*.

Fig. 7-1 Appearance of B. subtilis spore petri dishes after incubation with different exposure times to different bacterial numbers (spore/mL) and times (number of passes) to compressed air plasma. Other discharge parameters: gas flow rate=5 slm; output power from power power=300 W; and gap=1 mm.
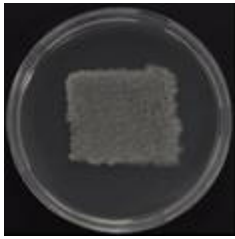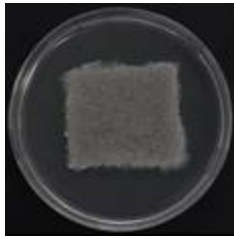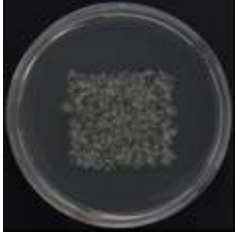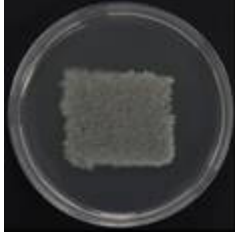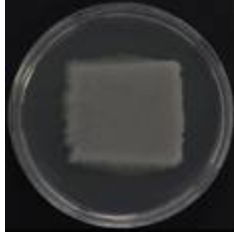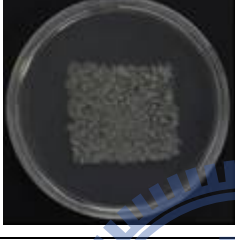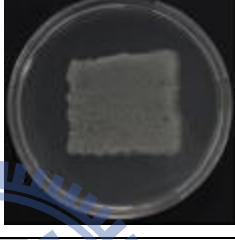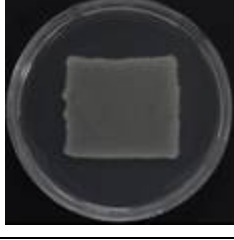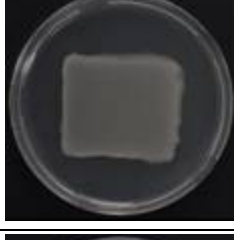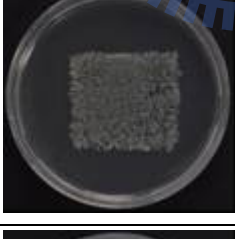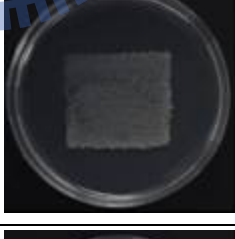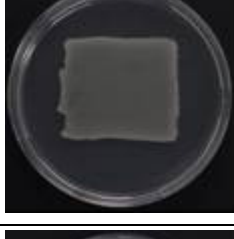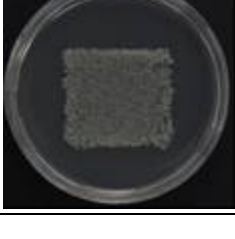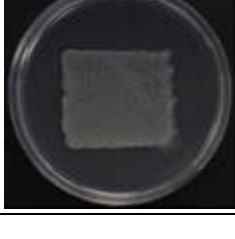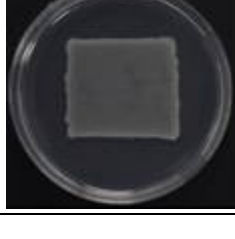
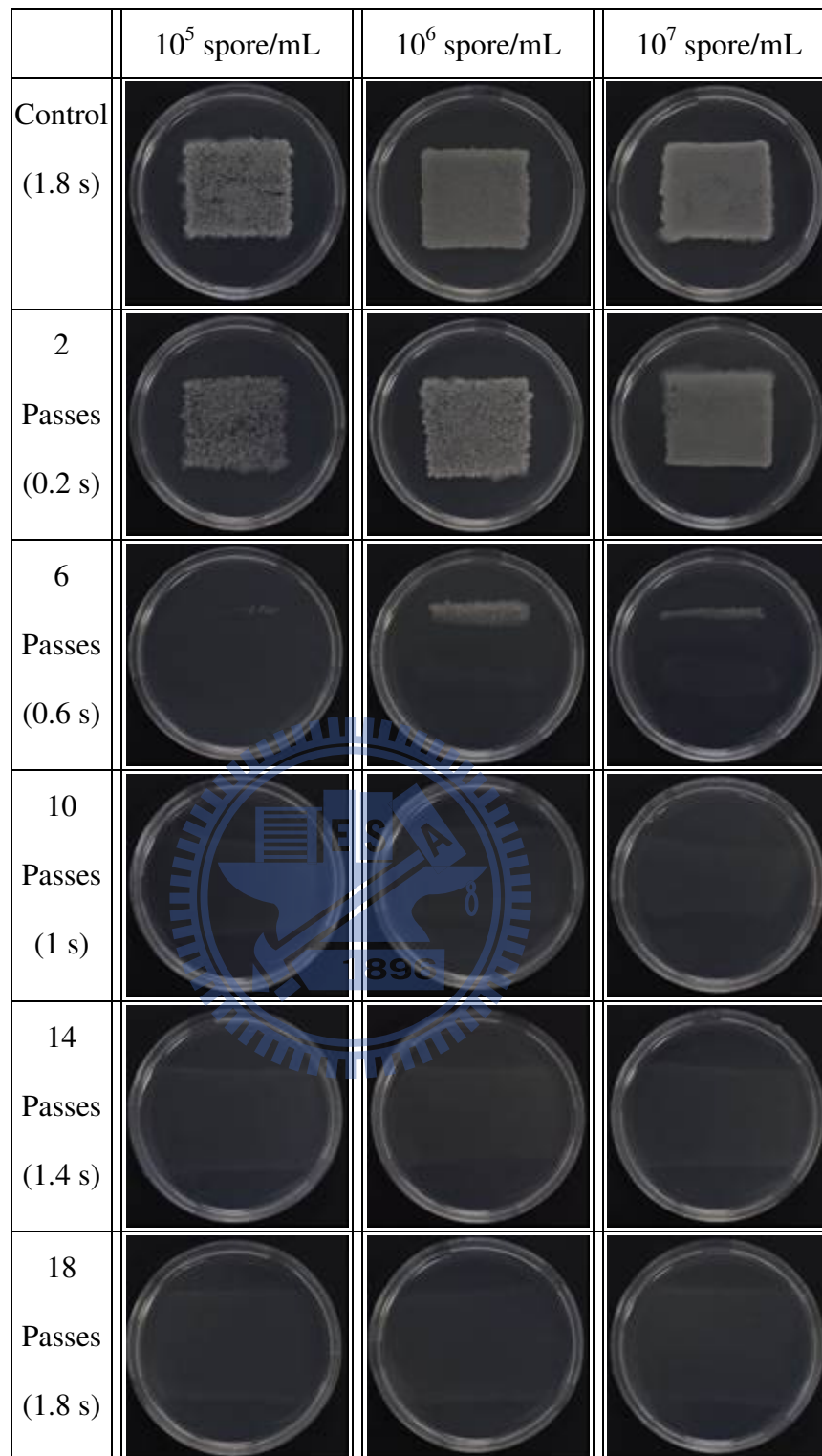|	10^5 spore/mL	10^6 spore/mL	10^7 spore/mL
Control (1.8 s)			
2 Passes (0.2 s)			
6 Passes (0.6 s)			
10 Passes (1 s)			
14 Passes (1.4 s)			
18 Passes (1.8 s)			

Fig. 7-2 Appearance of *B. subtilis* spore petri dishes after incubation with different exposure times to different bacterial numbers (spore/mL) and times (number of passes) to CF$_4$/air (2%) plasma. Other discharge parameters: gas flow rate=5 slm; output power from power supply=300 W; and gap=1 mm.

(a)
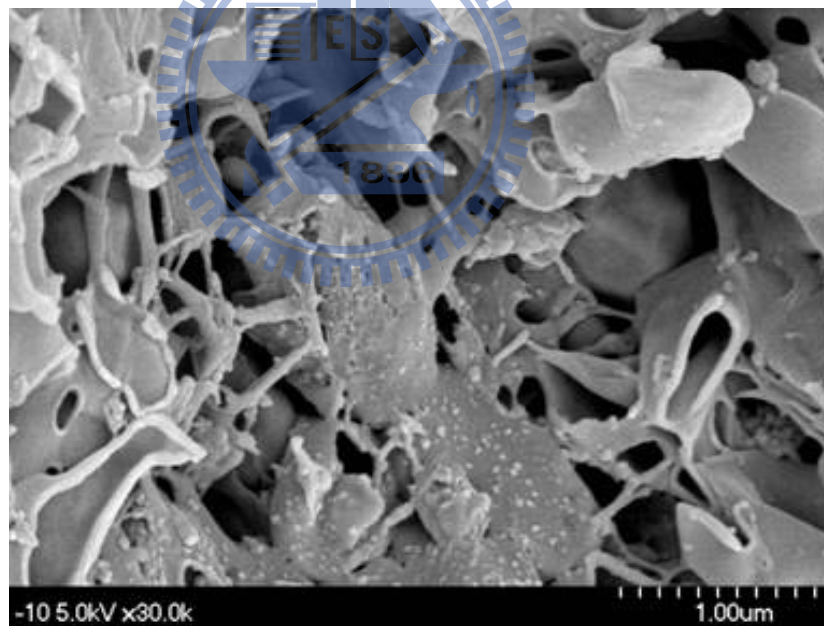
(b)

Fig. 7-3 SEM images of various microorganisms with a parallel-plate DBD APPJ using compressed CF$_4$/air (2%): (a) untreated *B. subtilis* spore; and (b) plasma-treated *B. subtilis* spore.

List of Publications

Journal Publications

1. **M.-H. Chiang**, K.-C. Liao, I.-M. Lin, C.-C. Lu, H.-Y. Huang, C.-L. Kuo and J.-S. Wu*, "Modification of Hydrophilic Property of Polypropylene Films by a Parallel-Plate Nitrogen-Based Dielectric Barrier Discharge Jet", *IEEE Transactions on Plasma Science*, Vol. 38, Issue 6, pp. 1489-1498, 2010.

2. **M.-H. Chiang**, J.-Y. Wu, Y.-H. Li, J.-S. Wu*, S.-H. Chen and C.-L. Chang, "Inactivation of *E. coli* and *B. subtilis* by a parallel-plate dielectric barrier discharge jet", *Surface & Coatings Technology*, Vol. 204, Issue 21-22, pp. 3729-3737, 2010.

3. **M.-H. Chiang**, K.-C. Liao, I.-M. Lin, C.-C. Lu, H.-Y. Huang, C.-L. Kuo, J.-S. Wu, C.-C. Hsu and S.-H. Chen, "Effects of Oxygen addition and treating distance on surface cleaning of ITO glass by a non-equilibrium nitrogen atmospheric-pressure plasma jet", *Plasma Chemistry and Plasma Processing*, accepted in June 2010, DOI 10.1007/s11090-010-9237-4.

4. Y.-M. Chiu, C.-T. Hung, F.-N. Hwang, **M.-H. Chiang**, J.-S. Wu* and S.-H. Chen, "Effect of Plasma Chemistry on the Simulation of Helium Atmospheric-Pressure Plasmas", *Computer Physics Communications*, accepted in June 2010.

5. K.-W. Cheng, C.-T. Hung, **M.-H. Chiang**, F.-N. Hwang and J.-S. Wu*, "One-dimensional Simulation of Nitrogen Dielectric Barrier Discharge Driven by a Quasi-Pulsed Power Source and Its Comparison with Experiments", *Computer Physics Communications*, accepted in June 2010.

6. J.-Y. Wu, **M.-H. Chiang**, C.-L. Kuo and J.-S. Wu*, "Effective Sterilization of *B. subtilis* Spore Using the Post-discharge Jet Region of a Dielectric Barrier Discharge with Air/CF$_4$ Mixture," *Applied Physics Letters*, in preparation.

7. C.-L. Kuo, J.-Y. Wu, **M.-H. Chiang**, H.-Y. Huang and J.-S. Wu*, "Ultra-fast Amino Functionalization of PLA Surface Using the Post-Discharge Jet Region of a Dielectric Barrier Discharge," _Biomaterials_, in preparation.

International Conference Papers

1. **M.-H. Chiang**, Y.-T. Liu, and J.-S. Wu*, "Measurements of Thermal-Fluid Fields of a RF-driven Atmospheric-Pressure Plasma Jet, "3rd International Symposium on Advanced Fluid/Solid Science and Technology in Experimental Mechanics,Tainan, Taiwan, December 7-10, 2008. (Oral presentation)

2. **M.-H. Chiang**, J.-Y. Wu, Y.-H. Li and J.-S. Wu*, "Inactivation of _E. coil_ and _B. subtilis_ Using a Quasi-Pulsed Power Driven Air Atmospheric Pressure Plasma Jet," 2008 Taiwan-Japan Bilateral Technology Interchange Project- The Workshop on the Applications of Plasma to Bio-Medical Engineering, Taoyuan, Taiwan, December 15-17, 2008.

3. **M.-H. Chiang**, I-M. Lin, C.-C. Lu, H.-Y. Huang, J.-S. Wu* and K.-C. Liao, "Characterization of a Nitrogen-Based Planar DBD APPJ and Its Application in ITO Glass Cleaning," CAPPSA 2009-4th International Congress on Cold Atmospheric Pressure Plasmas: Sources and Applications, Belgium, June 22-24, 2009. (Oral presentation)

4. **M.-H. Chiang**, K.-C. Liao, I-M. Lin, C.-C. Lu, H.-Y. Huang, J.-S. Wu*, "Modification of Polymer Surfaces Using the Post-Discharge Region of an Atmospheric-Pressure Dielectric Barrier Discharge," The Sixth Asia-Pacific International Symposium on the Basic and Application of Plasma Technology (APSPT-6), Hsinchu, Taiwan, December 14-16, 2009.